

# **DEVELOPING COUPLED CAVITY LIVING LASER FOR BIOLOGICAL CELL ANALYSIS**

Husni Hani Jameela SAPINGI

School of Physics and Astronomy

Cardiff University



A thesis submitted in fulfillment of the requirements for  
the degree of

Doctor of Philosophy

March 2016

# Abstract

The development of a prototype of a coupled cavity living laser that is aimed to be used for cell analysis is described. Quantum well and quantum dot material is characterized as the potential active medium. Quantum dot material has the beneficial qualities of a low internal optical loss  $\alpha_i$  of  $2\pm1\text{ cm}^{-1}$ , broader gain spectrum with reduced peak gain magnitude as well as larger spectral peak gain shift with increasing current density. However, the maximum gain available with quantum dot at 300 K is smaller ( $15\text{ cm}^{-1}$  compared to  $37\text{ cm}^{-1}$ ), which might limit the device performance where the etched mirror loss was large. The quantum well active medium material is therefore used for the fabrication of the prototype.

The recipe for the fabrication of etched facets has been investigated since the monolithic design of the coupled cavity living laser doesn't allow cleaving of the inner facets. A nickel mask is found to be a suitable mask for inductively coupled plasma etching of semiconductor crystal here as unlike silicon oxide the metal doesn't have any significant interaction with the etchant during the etching process. Oxide stripe lasers with cleaved – etched facets show decreasing threshold current density and increasing external and internal quantum efficiency as an increasing exposure dose factor and short development time is applied. The electron beam lithography process for mask patterning requires a high exposure dose factor which is 1.5 and short development time, which is 40 seconds to produce etched facet with minimum striations and the best reflectivity achieved is 0.24. This level of total losses, where a mirror reflectivity of 0.24 is achieved, coupled with the measured  $\alpha_i$  means that quantum dot material could be used for future iterations.

The prototype of a coupled cavity living laser is fabricated with the developed processing procedure. The laser devices function as individual laser cavities with threshold current of 538 mA for laser 1 and 588 mA for laser 2. The vertical far field divergence  $\theta$  of  $25^\circ$  along with the channel width of  $125\text{ }\mu\text{m}$  means that only 0.004 of the emitted electric field profile overlaps with the second cavity. The fabricated prototype of a coupled cavity living laser also operates in a source – detector mode. Laser 1 and 2 appear to give

threshold current of 421 mA and 446 mA respectively when they are operating as a source and signal is measured using the other device operating as a detector. The apparent reduction compared to the externally measured threshold is likely to be due to the changing fraction of light coupled from one section to the other as the near field and consequently the far field changes around threshold and the influence this has on the determination of the threshold from the slope characteristic. When both sections are operated as lasers a negligible effect is seen on the threshold current of one due to contributions from the other and this may be due to the very small fraction of light coupled from one to the other.

# Acknowledgements

I am grateful to ALLAH, the Creator and the Guardian of the universe, and to whom I owe my very existence.

It has been a really tough journey but I am truly blessed to have so many people that have accompanied me throughout this journey. Firstly, I would like to express my sincere gratitude to my supervisor Prof. Peter Snowton for his encouragement, patience, guidance and continuous support throughout my PhD study.

Besides my supervisor, I also would like to thank Dr. Rob Thomas, who helps me a lot since the first day I registered as a PhD student. Thank you for all the interesting discussions and helps in the clean room as well as in the Opto lab.

I would also like to give a special thanks to the members of staff who have helped me during my studies. In particular Dr. Phil Buckle, Mrs. Karen Barnett, Dr. Angela Sobiesierski and Mr. Chris Dunscombe for all the help in the clean room. Not forgetting Dr. Awg Makarimi, Dr. Stella Elliot, Dr. Sam Shutts and Dr. Mohamed Al-Ghamdi for helping out in the Opto lab and lots of useful motivation, discussion throughout my studies.

My sincere thanks also go to the administrative staff, Louise Winter as well as the Director of PG study Dr. Dan Read for assisting me in all the administrative issues.

Thank you to the Ministry of Higher Education Malaysia and Universiti Teknologi Malaysia for the sponsorship and study leave granted to me.

To the Malaysian Community in Cardiff, thank you for the great memories. A special thanks dedicated to the family of Abang Yusri and Kak Shima, who is always supporting me and lending me a helping hand in difficult times.

Most importantly, I would like to thank my husband, Muhammad Hazim Anuar for his endless love, continuous emotional support and great patience throughout this journey. Thank you to my beautiful children, Amir Rafiq and Amira Azzahra, for cheering me up every single day. Thank you to both of my parents, my parents in law, family and friends for supporting and praying for me.

Last but not least, to my late nephew Abu Khaer Ridzuan. You light up our life with your presence. Even when you are gone, the memories linger on. We just can't stop talking about you Dikboo. Have fun in heaven sweetheart. When the time comes, take Umi and Baba hands, shed their tears and walk in heaven with them. Until we meet again Dikboo. Alfatihah.

# Contents

<b>Chapter 1 : Introduction .....</b>	<b>1</b>
1.1 Introduction.....	1
1.2 Objectives .....	2
1.3 Thesis Structure .....	4
1.4 Bibliography .....	5
<b>Chapter 2 : Literature Review .....</b>	<b>6</b>
2.1 Introduction.....	6
2.2 Fundamental Of Laser Physics .....	6
2.2.1 What Is A Laser? .....	6
2.2.2 How To Achieve Laser Action? .....	6
2.3 Semiconductor Laser .....	10
2.3.1 Brief History Of Semiconductor Laser .....	10
2.3.2 Light Emission In Semiconductor Laser .....	12
2.3.3 Semiconductor Laser Structure .....	17
2.3.4 Quantum Confinement.....	20
2.4 Coupled Cavity Laser System.....	23
2.4.1 Far Field Diffraction In The Coupled Cavity Laser Systems .....	25
2.5 Bibliography .....	28
<b>Chapter 3 : Active Medium.....</b>	<b>30</b>
3.1 Introduction.....	30
3.2 Multisection Technique.....	32
3.1.1 Multisection Device.....	33
3.1.2 Multisection Technique Measurement Principle .....	33
3.1.3 Device Checks.....	36

3.1.4	Experimental Procedure .....	40
3.3	Characterization Of Quantum Well And Quantum Dot Active Media.....	42
3.3.1	Absorption.....	42
3.3.2	Modal gain .....	44
3.4	Conclusion .....	52
3.5	Bibliography .....	54
<b>Chapter 4</b>	<b>: Etched Facet.....</b>	<b>56</b>
4.1	Introduction.....	56
4.2	Electron Beam Lithography.....	57
4.3	Inductively Coupled Plasma Etching.....	62
4.4	Fabrication Of Etched Facet .....	64
4.4.1	Selection Of Material For The Mask .....	64
4.4.2	Selection Of Exposure Dose And Development Time For Mask Patterning	72
4.5	Characterization of Cleaved Facet and Etched Facet.....	80
4.5.1	Reflectivity.....	80
4.5.2	Threshold Current Density .....	81
4.5.3	Efficiency.....	85
4.5.4	Mirror Loss.....	88
4.6	Conclusion .....	88
4.7	Bibliography .....	90
<b>Chapter 5</b>	<b>: The Prototype Of A Coupled Cavity Living Laser.....</b>	<b>93</b>
5.1	Introduction.....	93
5.2	Design And Fabrication Of The Prototype Of A Coupled Cavity Living Laser ....	94
5.3	Far Field Measurement .....	99
5.4	Light – Current –Voltage (LIV) Measurement .....	101
5.4.1	Laser 1 And Laser 2 As An Individual Laser.....	101
5.4.2	Laser 1 And Laser 2 As A Source – Detector .....	104

5.4.3	Laser 1 And Laser 2 As Laser – Laser.....	106
5.5	Conclusion .....	109
5.6	Bibliography .....	111
<b>Chapter 6</b>	<b>: Conclusions And Future Work.....</b>	<b>113</b>
6.1	Conclusions .....	113
6.2	Future Works .....	115
6.3	Bibliography .....	117



# List of Figures

Figure 1.1 : A simplified schematic top view of a flow cytometer system [4].-----	2
Figure 2.1 : Essential elements to achieve laser action. -----	7
Figure 2.2 : Schematic diagram of laser cavity indicating the exponential growth of light intensity along the cavity, the loss and reflection of light at each mirror.-----	9
Figure 2.3 : E-k diagram of a typical (a) direct and (b) indirect band gap semiconductor. -----	11
Figure 2.4 : Conduction band and three sub-bands of valence band i.e. light hole, heavy hole and split-off bands in a semiconductor material. -----	12
Figure 2.5 : Absorption. -----	13
Figure 2.6 : Spontaneous emission.-----	14
Figure 2.7 : Stimulated emission. -----	15
Figure 2.8 : Three level energy state.-----	17
Figure 2.9 : Heterostructure laser diode [4]. -----	18
Figure 2.10 : Schematic diagram of double heterostructure band diagram that provide optical confinement. $n(x)$ represents the refractive index profile and $E(x)$ represents the electric field profile of the propagating mode. -----	18
Figure 2.11 : Energy band diagram corresponding to the three-region of double heterostructure laser (a) when they are not in contact, (b) when they are in contact with no bias and (c) under forward bias. -----	19
Figure 2.12 : Laser beam divergence in near field and far field.-----	20
Figure 2.13 : Density of state as a function of structure size. -----	22
Figure 2.14 : Coupled cavity laser geometry.-----	24
Figure 2.15: Schematic diagram of the far field beam divergence as the lasing transverse mode leaves the laser source waveguide. -----	26
Figure 2.16 : Schema of the far field light distribution.-----	26
Figure 3.1 : Schematic diagram of a 50 $\mu\text{m}$ stripe multisection device (not to scale).---	33
Figure 3.2 : The exemplary ASE spectra of a quantum well multisection device. -----	35
Figure 3.3 : Exemplary modal gain and absorption curves obtained from amplified spontaneous emission spectra of a quantum well material. -----	36

Figure 3.4 : Schematic diagram of experimental set up for light - current - voltage (LIV) measurement. The red line shows the light path and the black lines show electrical connections. -----	37
Figure 3.5 : I-V characteristic for section 1 (blue) and section 2 (red) of a multisection device. -----	38
Figure 3.6 : Schematic block diagram of near field experimental setup. -----	39
Figure 3.7 : Exemplary (a) uniform and (b) non uniform near field distribution of a multisection device.-----	40
Figure 3.8 : A multisection device is mounted onto the transistor header. -----	41
Figure 3.9 : Schematic diagram of experimental setup for multisection technique measurement.-----	41
Figure 3.10 : Absorption spectra of (a) quantum well and (b) quantum dot multisection devices. -----	43
Figure 3.11 : The gain and absorption of the multisection device.-----	45
Figure 3.12 : Net modal gain spectra of (a) quantum well and (b) quantum dot multisections at room temperature. -----	46
Figure 3.13 : Plot of peak gain against applied current density as a function of temperature for (a) quantum well and (b) quantum dot samples. -----	49
Figure 3.14 : Plot of the applied current density against inversion level as a function of temperature for (a) quantum well and (b) quantum dot sample. -----	50
Figure 3.15 : Plot of applied current density as a function of temperature at a constant value of the inversion level of quantum well and quantum dot samples. -----	51
Figure 3.16 : Plot of peak gain against applied current density at $T = 300$ K. -----	52
Figure 4.1 : Screen shot of the design page of Klayout software.-----	59
Figure 4.2 : Image of sample holder used in e-line Raith system.-----	60
Figure 4.3 : Image of e-line Raith Electron beam lithography system available in the clean room of Cardiff University. -----	60
Figure 4.4 : Illustration of the electron beam gun and stage movement during exposure. -----	61
Figure 4.5 : Plasmalab System 100 by Oxford Instruments available in the clean room of Cardiff University.-----	62
Figure 4.6 : Schematic diagram of gas chamber for Plasmalab System 100 [3]. -----	63

Figure 4.7 : Sample with a nickel mask that undergone air plasma etch to stripping resist before evaporation of metal.-----	67
Figure 4.8 : Processing procedure of fabrication of etched facet using SiO <sub>2</sub> and nickel mask.-----	68
Figure 4.9 : SEM images of facets formed by a dry etching technique using SiO <sub>2</sub> as a mask.-----	69
Figure 4.10 : Facet formed using SiO <sub>2</sub> mask on (a) single quantum well wafer sample and (b) bare GaAs wafer sample.-----	70
Figure 4.11 : SEM image of facets formed by a dry etching technique using nickel as a mask.-----	71
Figure 4.12 : High verticality pattern was observed on both facets fabricated using (a) SiO <sub>2</sub> and (b) nickel mask.-----	71
Figure 4.13 : Plot of the peak height of the striated etched facet as a function of exposure dose and development time.-----	73
Figure 4.14 : The Gaussian roughness distributions for the samples fabricated at different dose factor with a development time of (a) 40 seconds and (b) 60 seconds. -----	74
Figure 4.15 : Mechanism of radiation-induced chain scission in PMMA [14].-----	75
Figure 4.16 : Polymer-solvent interactions can result in gel formation & swelling [6]. -	77
Figure 4.17 : Width of the etched facet pattern for the sample fabricated with different dose factor and were developed at 40 seconds and 60 seconds.-----	79
Figure 4.18 : Schematic diagram of cleaved-cleaved facets laser and cleaved-etched facets laser. -----	82
Figure 4.19 : Light-current (L-I) curves for a cleaved – cleaved facets laser and cleaved-etched facets lasers for various dose factors applied during the mask patterning process.-----	83
Figure 4.20 : Plot of threshold current density, $J_{th}$ for cleaved-etched devices that were fabricated with various dose factors applied during mask patterning.-----	85
Figure 4.21 : Plot of power against current for cleaved-etched devices that were fabricated with various dose factors applied during mask patterning.-----	86
Figure 5.1 : Proposed design of the prototype of coupled cavity living laser. -----	94
Figure 5.2 : Schematic diagram of far field measurement apparatus.-----	99
Figure 5.3 : The normalized angular far field profile of etched facet operating above threshold current.-----	101

Figure 5.4 : Current - voltage (IV) curves of laser 1 (blue) and laser 2 (red) on a prototype of a coupled cavity living laser. ....	102
Figure 5.5 : Light - current (LI) curves of laser 1 (blue) and laser 2 (red) on a prototype of a coupled cavity living laser. ....	103
Figure 5.6 : Current - voltage (IV) curves of a coupled cavity living laser operating as a source and a detector. ....	104
Figure 5.7 : Light - current (LI) curves of a coupled cavity living laser operating as a source and a detector. ....	105
Figure 5.8 : Current - voltage (IV) curves of laser 1 when a constant current is applied to laser 2. ....	107
Figure 5.9 : Light - current (LI) curves of laser 1 when a constant current is applied to laser 2. ....	107
Figure 5.10 : Current - voltage (IV) curves of laser 2 when a constant current is applied to laser 1. ....	108
Figure 5.11 : Light - current (LI) curves of laser 2 when a constant current is applied to laser 1. ....	108

# List of Tables

Table 3.1 : Layer structure of MR2459 Main quantum dot wafer. -----	31
Table 4.1 : Parameter affecting EBL process. Ref [3].-----	58
Table 4.2 : Summary of parameters used in fabrication of a prototype of a coupled cavity living laser. -----	62
Table 4.3 : Summary of parameters used in fabrication of etched facet for the prototype of a coupled cavity living laser.-----	64
Table 4.4 : Summary of the measured value of surface roughness and calculated efficiency. -----	81
Table 4.5 : Summary of the measured values used to calculate device threshold current density. -----	84
Table 4.6 : Summary of the measured slope and calculated external quantum efficiency of laser devices fabricated with different value of dose factor during mask patterning.---	87
Table 5.1 : Processing procedure of the prototype of coupled cavity living laser. -----	95

# Chapter 1 : Introduction

## 1.1 Introduction

This thesis describes the development of a fabrication process for a coupled cavity laser intended for blood analysis. A full blood count is one of the most common blood tests. A full blood count involves counting, measuring and analysing red cells, white cells and platelets as well as measuring the amount of haemoglobin in the red blood cell [1] [2]. It frequently represents the first step of haematological analysis. Usually the data of full blood count is used to make decisions whether or not additional medical attention is required. Unusually high or low counts indicate the presence of disease such as anaemia, leukaemia, bone marrow problems, and many more [2] [3].

In the past, full blood counting was performed manually, by inspecting a slide prepared with a sample of the patient's blood under a microscope. Though this method is capable of providing detailed data regarding any abnormalities appearing in the blood cells, analysing a large number of cells in this way is ineffective as it is time-consuming as well as a labour intensive operation.

At the present time, full blood count is generally performed using the automated analyser such as a flow cytometer. A flow cytometer is a system for sensing cells as they travel in a fluid stream through a laser beam, as shown in Figure 1.1. The laser beam that hits the cells is either scattered or absorbed and then re-emitted (fluorescence). This scattered or re-emitted light is then collected by the detector such as an array of photomultiplier tube and photo detector. Nowadays, flow cytometers are commonly used in the diagnosis of health conditions, particularly full blood count procedure. Nevertheless, flow cytometers are bulky and expensive machines. The reliability of the results depends on consistent system calibration and good sample preparation. These limitations initiated the idea of producing lab-on-chip system for cell analysis. Other than to overcome those limitations, the lab-on-chip system may also lessen the time taken to synthesize and analyse a sample due to its small volume. Moreover, it permits sample to be processed and analysed at the point of need rather than a centralized laboratory.

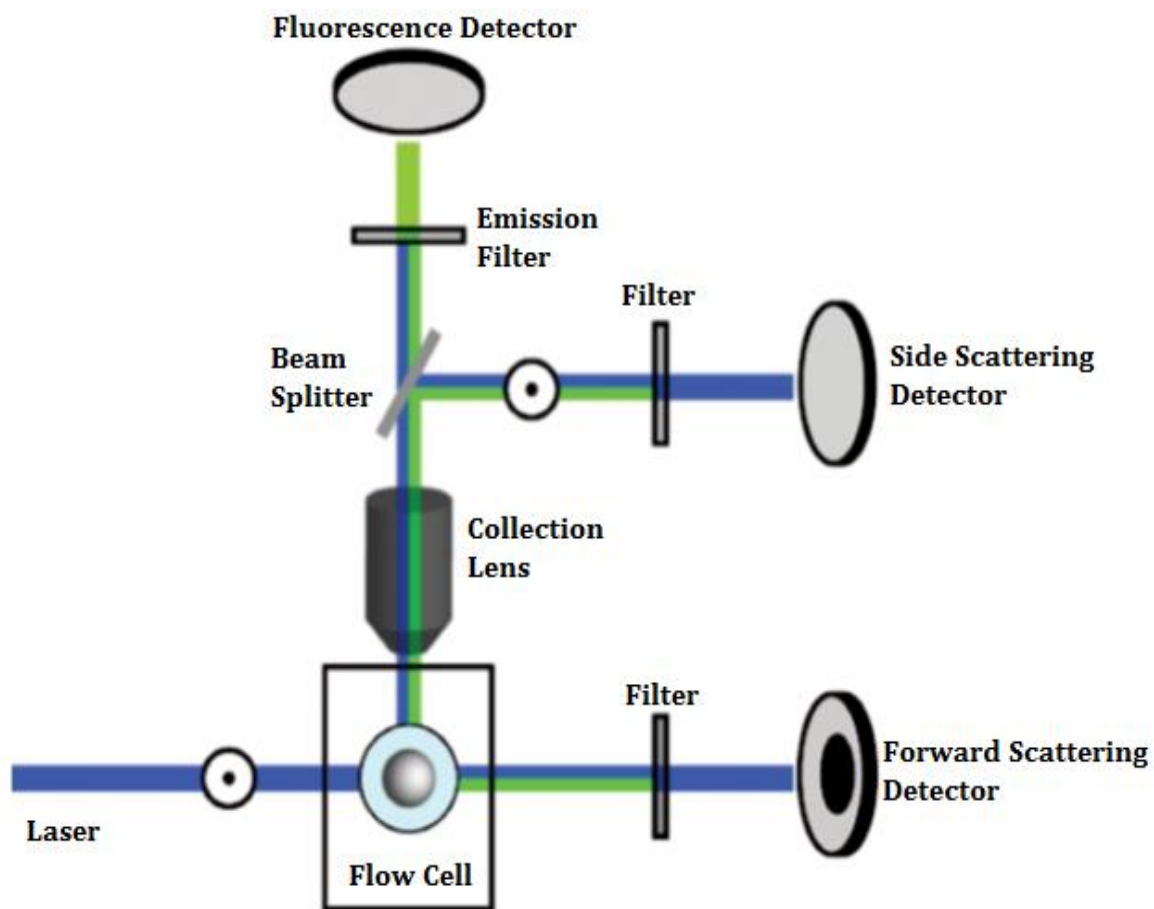


Figure 1.1 : A simplified schematic top view of a flow cytometer system [4].

## 1.2 Objectives

This project aims to fabricate a prototype of a coupled cavity ‘living laser’ that can be used for live biological cell analysis. This can be achieved by having a coupled cavity laser system with an integrated fluidic channel. A pair of laser diodes will be fabricated that lies along a common, linear optical axis with a fluidic channel running between them. Two cavities coupled together across a small gap restrict the radiation to the extremely low bandwidth that can be sustained in both resonant chambers [5]. Laser diodes are suitable for this purpose as they can operate with relatively low power input. This factor is very important to ensure that the biological cells remain alive after they have undergone lasing

action. The simplest realization of such a structure is represented schematically in Figure 1.2.

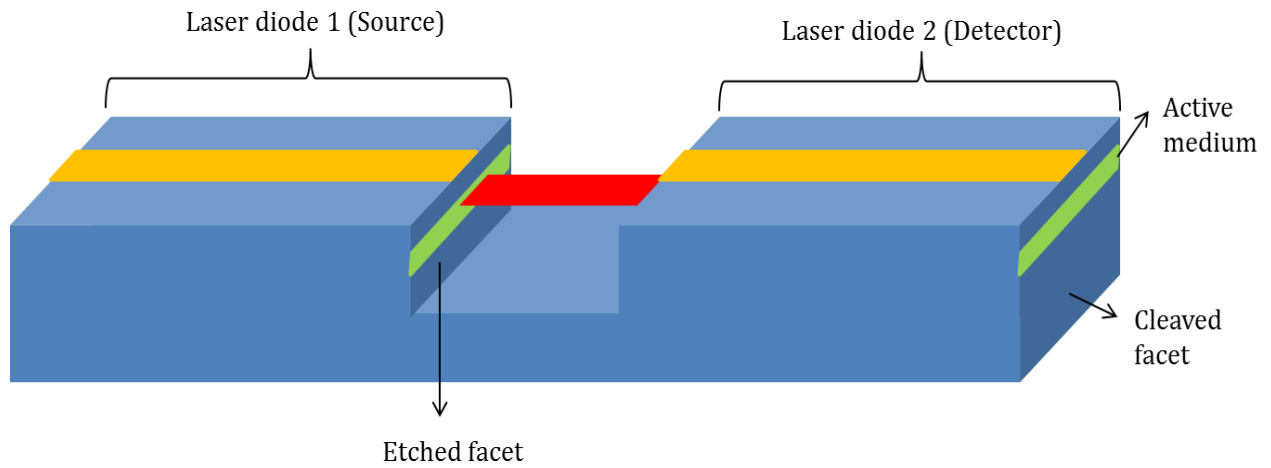


Figure 1.2 : Simplest realization of a coupled cavity 'living laser'.

While it is possible to fabricate such a structure from discrete devices, a more attractive approach is to etch the channel in a semiconductor laser structure. This latter approach should facilitate large scale integration. However, the concept is dependent on the quality of etched facet. The technique and a recipe for fabrication of the etched facet is investigated in this study.

A comparison study of the performance of quantum well and quantum dot active media at different temperature is conducted to investigate which active media is best suited for fabrication of the prototype of a coupled cavity 'living laser'.

Finally, the processing procedure for the fabrication of the prototype of a coupled cavity 'living-laser' is developed with etching technique and active medium that has been investigated. The fabricated prototype will then undergo operational trial measurement to test its performance.



## 1.3 Thesis Structure

The following chapter in this thesis, Chapter 2 provides some necessary background theory relating to laser physics, semiconductor laser, quantum wells and quantum dots as well as the basic principle of the coupled cavity laser system. Chapter 3 describes the experimental techniques used in this work for characterization of active media, i.e. quantum well and quantum dot at various temperature. In Chapter 4, fabrication of the inner etched facet is discussed in detail. The performance of devices with fabricated etched facet is then characterized. Chapter 5 presents the developed processing procedure of the fabrication of a prototype of a coupled cavity 'living laser'. The latter part of this chapter presents the operational trial test that has been done on the fabricated prototype of a coupled cavity 'living laser'. Finally, Chapter 6 presents the conclusion of this study and provide some suggestions for future work.

## 1.4 Bibliography

- [1] "Wikipedia," [Online]. Available: [http://en.wikipedia.org/wiki/Complete\\_blood\\_count](http://en.wikipedia.org/wiki/Complete_blood_count). [Accessed 7 January 2015].
- [2] "Patient.co.uk," [Online]. Available: <http://www.patient.co.uk/health/full-blood-count-and-blood-smear>. [Accessed 7 January 2015].
- [3] "Boots," [Online]. Available: <http://www.webmd.boots.com/a-to-z-guides/full-blood-count>. [Accessed 7 January 2015].
- [4] J. Fattaccioli, J. Baudry, J.-D. Emerard, E. Bertrand, C. Goubault, N. Henry and J. Bibette, "Size and Fluorescence Measurements of Individuals Droplets by Flow Cytometry," *Soft Matter*, vol. 5, pp. 2232 - 2238, 2009.
- [5] E. Hetch, Optics, Adison Wesley, 2002.

## **Chapter 2 : Literature Review**

### **2.1 Introduction**

This chapter is dedicated to explaining the fundamentals of laser physics and how to reach lasing action followed by the background of semiconductor laser diodes. A brief theoretical background about quantum wells and quantum dots follows in the latter section of this chapter. The principle of the coupled cavity laser system is also discussed in the final part of this chapter.

### **2.2 Fundamental Of Laser Physics**

#### **2.2.1 What Is A Laser?**

The term LASER is an acronym formed from Light Amplification by Stimulated Emission of Radiation. Among the ideal laser characteristics that make it a high demand device is its directionality where the laser beam travels straight with almost no divergence. Unlike light from an ordinary lamp that diverges in every direction. The laser beam is also highly monochromatic. It emits a light beam with a single wavelength and frequency while an ordinary lamp emits a light beam with many wavelengths mixed. The laser provides excellent coherency which means the uniform phase of light relative to time. On the other hand ordinary light produces an inconsistent phase of light with respect to time.

#### **2.2.2 How To Achieve Laser Action?**

The laser makes use of processes that increase or amplify light signals after those signals have been generated by other means. These processes include stimulated emission and optical feedback.

There are three essential elements, as shown in Figure 2.1, needed in order to achieve laser action:

- i. An active or gain medium for amplification that emits at required wavelength,
- ii. A pumping mechanism to obtain population inversion,
- iii. An optical laser cavity to provide positive feedback to achieve coherent emission.

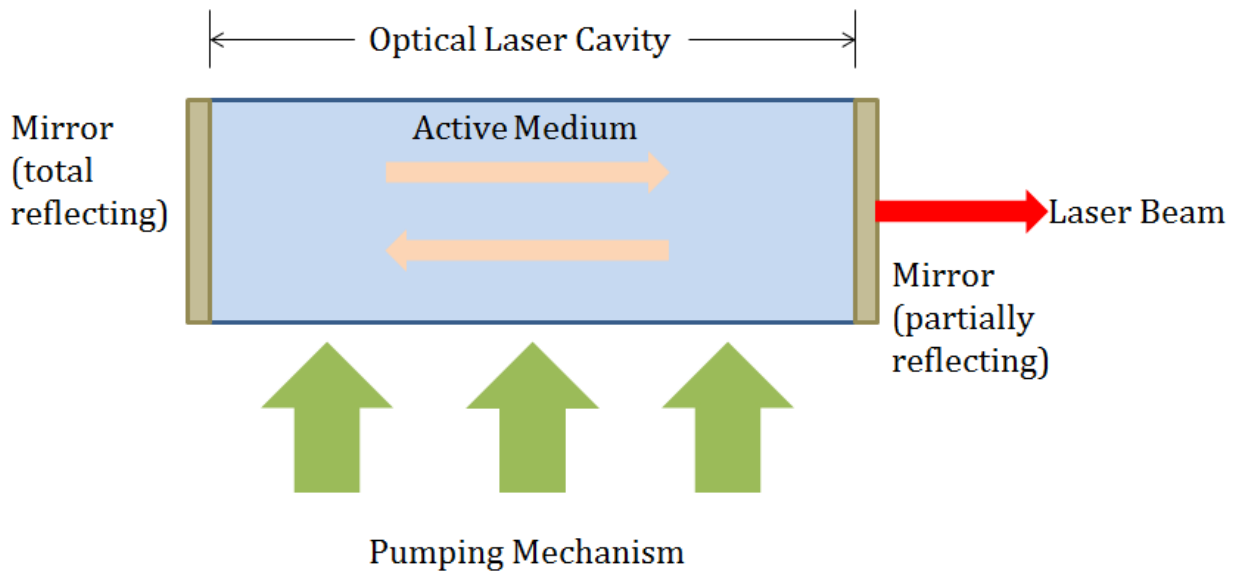


Figure 2.1 : Essential elements to achieve laser action.

### 2.2.2.1 The Active Medium

The laser active medium also known as gain medium is a material with properties that allow it to amplify light by stimulated emission. The gain medium determines the range of wavelengths for which laser radiation is possible. There are varieties of very different gain medium. For example, helium and neon (HeNe) gases that are used in gas laser, ruby or doped glass for solid state laser, gallium arsenide (GaAs), indium gallium arsenide (InGaAs), or gallium nitride (GaN) for semiconductor laser.

### **2.2.2.2 Pumping Mechanism**

The active medium can be pumped optically, electrically or chemically to obtain population inversion which is the necessary condition for laser action. For example, semiconductor lasers are normally electrically pumped using a p-n junction to inject the electron and holes. This is contained within a more complex multilayer structure known as a heterostructure which confines the light and carriers.

### **2.2.2.3 Optical Laser Cavity**

An optical laser cavity consists of two mirrors, one at each end of the cavity, usually one of them is highly reflective while the other one is partially reflective. These mirrors feedback a proportion of light incident on them, increasing the photon density within the cavity and hence increasing the stimulated emission. In semiconductor lasers, these mirrors are created by cleaving or polishing or etching the crystal planes normal to the optical axis and in this case the mirrors usually have the same reflectivity. This structure is called a Fabry-Perot resonator. The optical cavity determines the precise lasing wavelength within the range allowed by the active medium.

### **2.2.2.4 Threshold Condition**

Spontaneous emission provides the initial stimulus to start the lasing process. Spontaneously emitted photons with certain energy emitted in a direction along the cavity are amplified by the stimulated emission process. These photons are then reflected by the mirrors and further amplified on the return path.

The laser threshold condition is reached when the roundtrip gain matched the roundtrip loss. The loss comes from several sources:

- i. Mirror transmission, and
- ii. Internal optical mode loss.

The required threshold gain can be calculated using Figure 2.2 for reference.

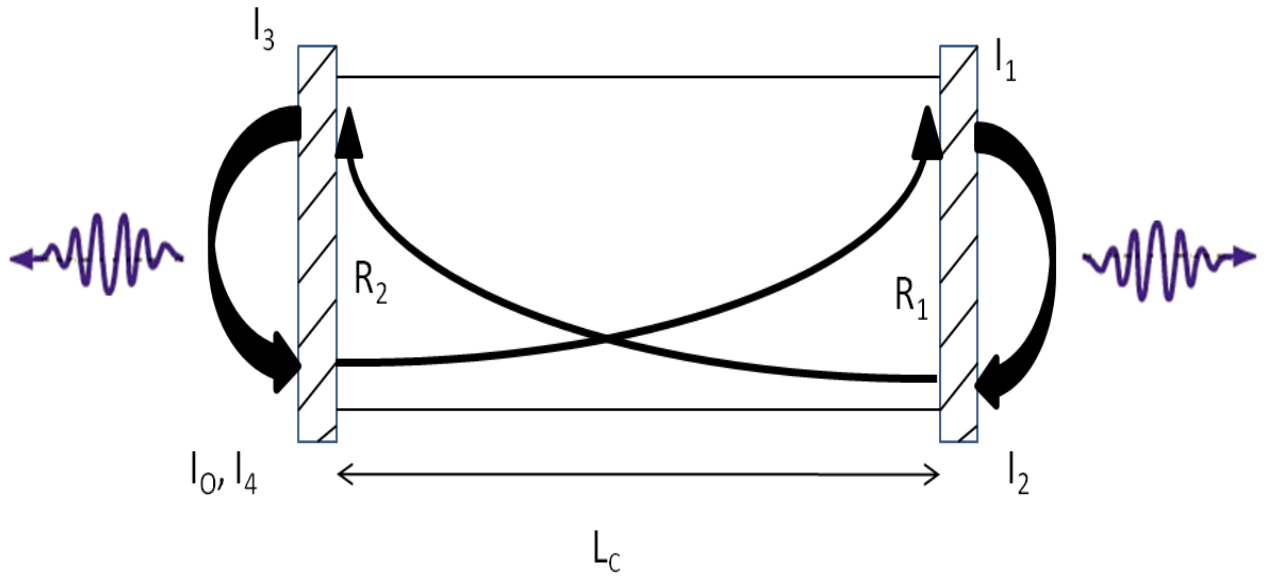


Figure 2.2 : Schematic diagram of laser cavity indicating the exponential growth of light intensity along the cavity, the loss and reflection of light at each mirror.

The initial light grows in intensity as it passes through the gain medium. If the length of the cavity is  $L_c$ , the value of the intensity at the first mirror is shown in Equation 2.1:

$$I_1 = I_0 \exp[(G - \alpha_i)L_c]$$

Equation 2.1

where  $I_0$  is the initial light intensity,  $G$  is the gain and  $\alpha_i$  is the internal optical mode loss that may cause by the absorption within the laser medium, absorption and scattering at the mirrors and scattering losses due to optical inhomogeneity in the active medium.

Due to reflection at the first mirror, which has the reflectivity  $R_1$ , the reflected intensity, is now reduced to a value:

$$I_2 = R_1 I_0 \exp[(G - \alpha_i)L_c]$$

Equation 2.2

This then grows exponentially again on the return trip:

$$I_3 = R_1 I_0 \exp[(G - \alpha_i)2L_c]$$

Equation 2.3

The intensity is then reduced again due to transmission losses at the second mirror:

$$I_4 = R_1 R_2 I_0 \exp[(G - \alpha_i)2L_C]$$

Equation 2.4

For a steady state to be achieved the final intensity  $I_4$  must be equal to the initial intensity,  $I_0$ . Therefore, by setting  $I_4 = I_0$  and rearranging Equation 2.5 gives the threshold condition as below:

$$\frac{I_4}{I_0} = R_1 R_2 \exp[(G_{th} - \alpha_i)2L_C] = 1$$

Equation 2.5

This can be rearranged in term of gain threshold  $G_{th}$  as shown in Equation 2.6:

$$G_{th} = \alpha_i + \frac{1}{2L_C} \ln \frac{1}{R_1 R_2}$$

Equation 2.6

In the Fabry - Perot laser, this condition is normally first met at the peak of the gain spectrum, which will be explained in Chapter 3.

## 2.3 Semiconductor Laser

### 2.3.1 Brief History Of Semiconductor Laser

The original concept of semiconductor laser or alternatively known as laser diode was introduced by Basov et al. in 1961 [1]. He suggested that stimulated emission of radiation could occur in a semiconductor by the recombination of carriers injected across a p-n junction. The material for laser diodes needs to have a direct band gap in order to allow photons to be produced from recombination events. Direct band gap means the material has the minimum of the conduction band  $E_c$  at the same value of wave vector  $k$  as the maximum in the valence band  $E_v$ . This is because only electron-hole pairs with the same momentum (vertical transition on E-k diagram) have a high probability of recombining via spontaneous or stimulated emission. An example energy,  $E$  against  $k$  graph is plotted

in Figure 2.3 and shows the configuration of the bands of material with a (a) direct and (b) indirect band gap property.

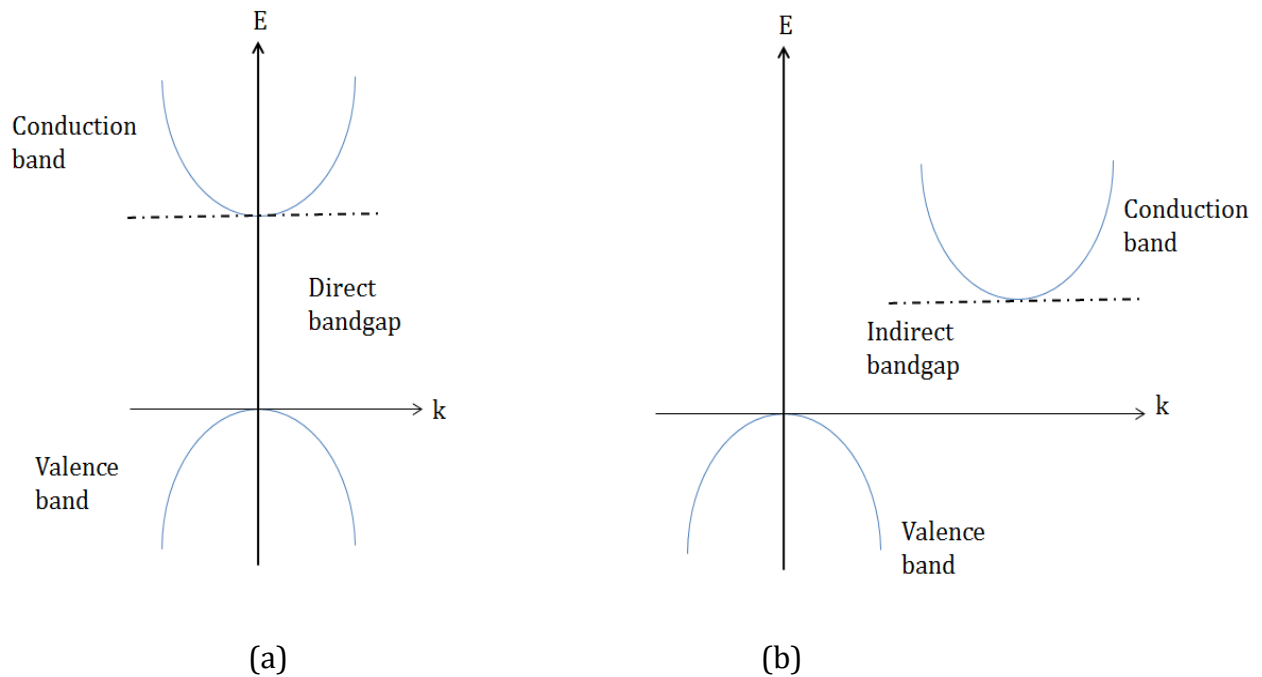


Figure 2.3 : E-k diagram of a typical (a) direct and (b) indirect band gap semiconductor.

In semiconductor material, the conduction band is essentially derived from the s-orbitals. Meanwhile, the valence bands often arise from three p-orbitals and are called the light hole band, the heavy hole band and the split-off band as seen in Figure 2.4. The terms “light and heavy hole” reflects the effective masses of the electron in the conduction band. Only light hole and heavy hole bands tend to be important under normal operating condition since the split-off band is further away in energy than the other two bands due to the spin orbit splitting interaction [2].



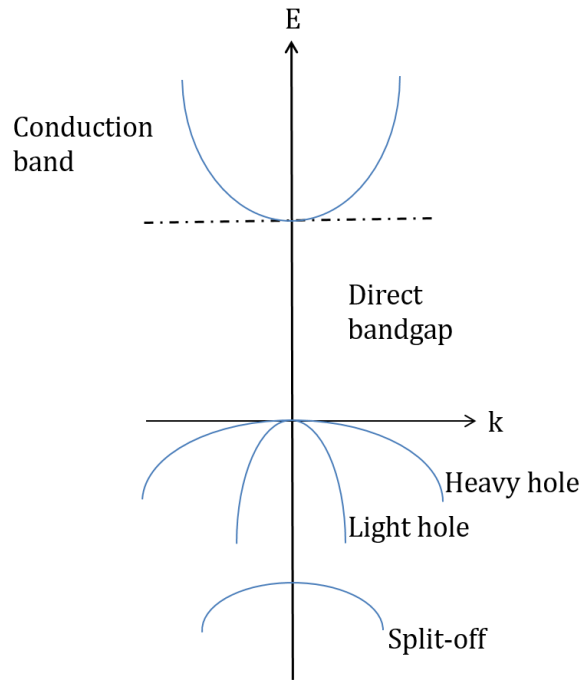


Figure 2.4 : Conduction band and three sub-bands of valence band i.e. light hole, heavy hole and split-off bands in a semiconductor material.

The first working semiconductor laser device appeared in 1962 when pulse oscillation at low temperature was observed in the first gallium arsenide (GaAs) laser [1] [3]. In 1969, the heterostructure laser was introduced [1] replacing the simple p-n junction. Continuous wave operation at room temperature was then observed in 1970 [3]. The continuous wave operation became possible because of better optical confinement in the heterostructure laser. Since then, semiconductor laser performance has continued to improve as more advanced heterostructures, containing quantum wells, and most recently quantum dots, are used as a gain medium. Nowadays, a semiconductor laser is one of the most important and widely used classes of laser such as for data storage, cable TV transmission, barcode scanner, and medical applications.

### 2.3.2 Light Emission In Semiconductor Laser

There are three kinds of transitions that are important in semiconductor laser, which occur between the conduction and valence band of the material. Those transitions are

absorption, spontaneous emission and stimulated emission. Of these three, only stimulated emission contributes to coherent optical gain.

### 2.3.2.1 Absorption

In absorption, an atom in a lower state absorbs a photon of frequency  $h\nu$  and moves to an upper state. This transition is represented by Equation 2.7 with  $h$  is the Planck's constant and  $\nu$  is the frequency of the light:

$$E_2 - E_1 = h\nu$$

Equation 2.7

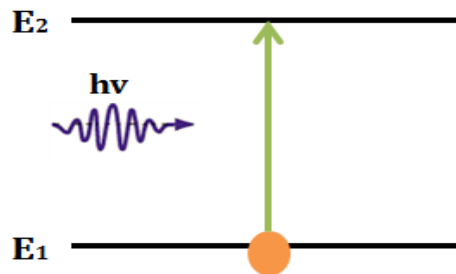


Figure 2.5 : Absorption.

The rate at which photons are absorbed is dependent on the number of occupied states in the valence band, the number of unoccupied states in the conduction band and the density of photons with the transition energy. In the Equation 2.8,  $p_1$  and  $p_2$  are the occupation probabilities of the lower and upper states respectively,  $B_{12}$  is the Einstein coefficient that represents the transition probability of an electron in the lower state being excited into a vacant upper state, and  $\rho(\nu)$  is the photon density:

$$R_{abs} = B_{12}p_1(1 - p_2)\rho(\nu)$$

Equation 2.8

### 2.3.2.2 Spontaneous Emission

In spontaneous emission an electron drops from an upper state to lower state and a photon is emitted. The energy of this photon is equal to the difference between the energy

of the involved states. The emitted photon has a random phase and direction. Therefore, it doesn't contribute to coherent optical gain.

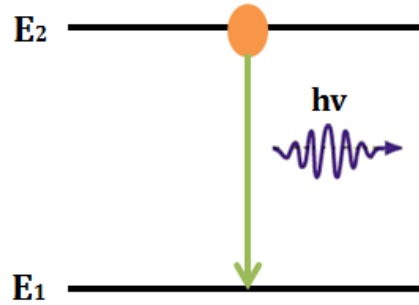


Figure 2.6 : Spontaneous emission.

The rate at which excited electrons will spontaneously emit photons is given by Equation 2.9 where  $A_{21}$  is the transition probability of an excited particle falling into a vacant lower state:

$$R_{spon} = A_{21}p_2(1 - p_1)$$

Equation 2.9

### 2.3.2.3 Stimulated Emission

In stimulated emission, an incident photon is strongly coupled with the electron. The photon causes the electron to decay to a lower energy state accompanied by the release of the second photon. The emitted photon has the same energy, direction and phase as the incident photon. Hence, it contributes to the coherent optical gain of the laser.

The stimulated emission rate depends on the occupation of both the levels and on the photon density at the transition energy as shown in Equation 2.10:

$$R_{stim} = B_{21}p_2(1 - p_1)\rho(\nu)$$

Equation 2.10

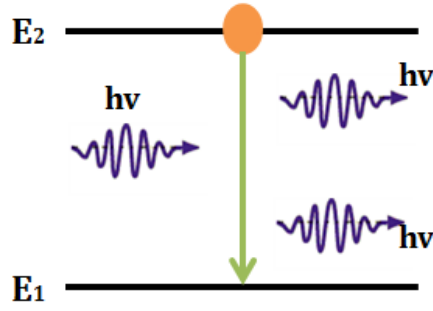


Figure 2.7 : Stimulated emission.

### 2.3.2.4 Einstein Relations

In equilibrium, the upward transition rate must equal the downward transition rate as shown in Equation 2.11:

$$R_{abs} = R_{spon} + R_{stim}$$

Equation 2.11

Substituting Equation 2.8, Equation 2.9, and Equation 2.10 in the Equation 2.11 gives:

$$B_{12}p_1(1 - p_2)\rho(v) = A_{21}p_2(1 - p_1)\rho(v) + B_{21}p_2(1 - p_1)\rho(v)$$

Equation 2.12

This can then be solved for  $\rho(v)$  to give:

$$\rho(v) = \frac{A_{21}p_2(1 - p_1)}{B_{12}p_1(1 - p_2) - B_{21}p_2(1 - p_1)}$$

Equation 2.13

Or,

$$\rho(v) = \frac{A_{21}}{B_{12} \frac{p_1(1 - p_2)}{p_2(1 - p_1)} - B_{21}}$$

Equation 2.14

As  $\frac{p_1(1 - p_2)}{p_2(1 - p_1)}$  consists of relative occupation probability of the states. It can be replaced with an expression derived by assuming that all the probabilities are governed by Fermi-Dirac statistic or, for the case of the simple two level atomic systems containing one electron,

the Boltzmann approximation to give Equation 2.15 below, which implies that the system is in thermal equilibrium.

$$\rho(v) = \frac{A_{21}/B_{21}}{(B_{12}/B_{21}) e^{hv/kT} - 1}$$

Equation 2.15

Comparing this with the Planck function for the distribution of radiation for a body in thermal equilibrium,

$$\rho(v) = \frac{\rho_o(v)hv}{e^{hv/kT} - 1}$$

Equation 2.16

Gives the results that in thermal equilibrium, the stimulated emission and stimulated absorption are complementary process associated with the same recombination rate,

$$B_{12} = B_{21}$$

Equation 2.17

and

$$A_{21} = \rho_o(v)hv \cdot B_{21}$$

Equation 2.18

These results were derived by Einstein for the case of two level single electron atoms, this is why the constant A and B are known as the Einstein coefficients.

### 2.3.2.5 Population Inversion

The achievement of a significant population inversion in the active medium is a precondition for laser action. Electrons will normally reside in the lowest available energy state. They can be elevated to upper or excited states by absorption. However, no significant collection of electrons can be accumulated by absorption alone since both spontaneous emission and stimulated emission will bring them back down.

A population inversion cannot be achieved with just two levels because the rate of absorption and spontaneous and stimulated emission is exactly the same, as shown by

Equation 2.11. Therefore, the electrons drop back down by photon emission about as fast as it can be pumped to the upper level.

For population inversion to be achieved, the minimum that is required is a three-level energy system. Electrons are pumped from the ground state of the system to a higher, unstable state. From here, they rapidly decay to a more stable state between the two. Laser transitions occur between this metastable state and the ground state.

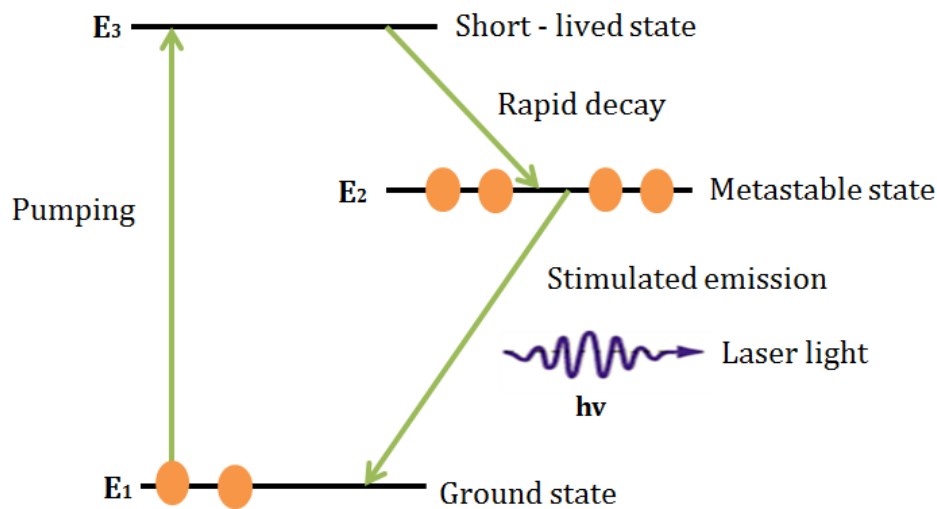


Figure 2.8 : Three level energy state.

### 2.3.3 Semiconductor Laser Structure

#### 2.3.3.1 Double Heterostructure

In a double heterostructure device, a layer of low bandgap active material is sandwiched between two high bandgap cladding layers. The active layer thickness is typically in the range of 0.1 – 0.3  $\mu\text{m}$ . This structure exploits the differences in bandgaps and refractive indexes between mixed semiconductors of different compositions. One commonly-used pair of materials is gallium arsenide (GaAs) with aluminium gallium arsenide ( $\text{Al}_x\text{Ga}_{1-x}\text{As}$ ). In this device the active region of p-GaAs is bounded by p-type AlGaAs on one side and n-type AlGaAs on the other as shown in Figure 2.9.

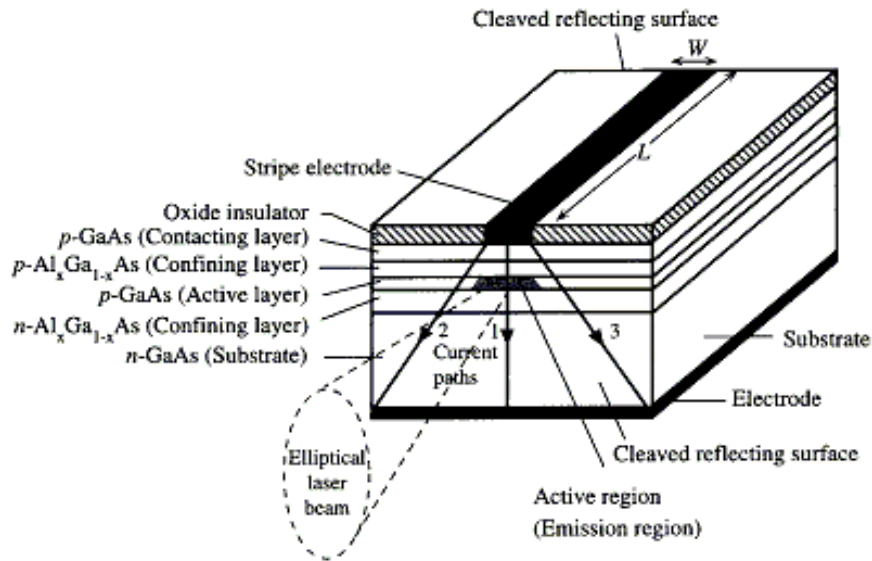


Figure 2.9 : Heterostructure laser diode [4].

The AlGaAs has a larger energy gap than GaAs and also a smaller refractive index. This causes the light to be confined to the active layer due to the total internal reflection phenomenon, see Figure 2.10.

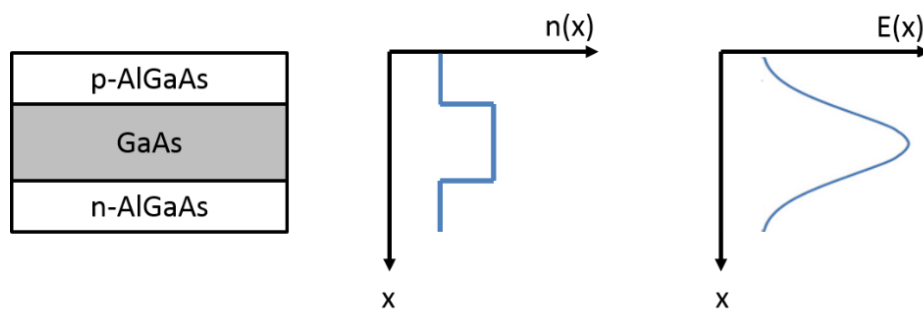


Figure 2.10 : Schematic diagram of double heterostructure band diagram that provide optical confinement.  $n(x)$  represents the refractive index profile and  $E(x)$  represents the electric field profile of the propagating mode.

In addition to optical confinement, this structure also has another beneficial effect which is carrier confinement to the active layer [5]. In a heterostructure laser, the carriers are physically prevented from diffusing away from the junction by the presence of a potential barrier created by the differing energy gaps of various layers. Figure 2.11 shows the energy band diagram corresponding to the three regions, i.e. active medium and barrier layers, (a) when they are not in contact, (b) before and (c) after forward biasing. As seen

in Figure 2.11 the potential barriers at the two junctions restrict the flow of electrons from the n-AlGaAs to the p-AlGaAs and holes from the p-AlGaAs to the n-AlGaAs layers. Consequently, there is a large concentration of accumulated charge carriers in the thin GaAs layer. Under forward bias a quasi-equilibrium exists and when quasi-Fermi level separation exceeds the transition energy, the conditions for gain is fulfilled thus leading to the amplification of light.

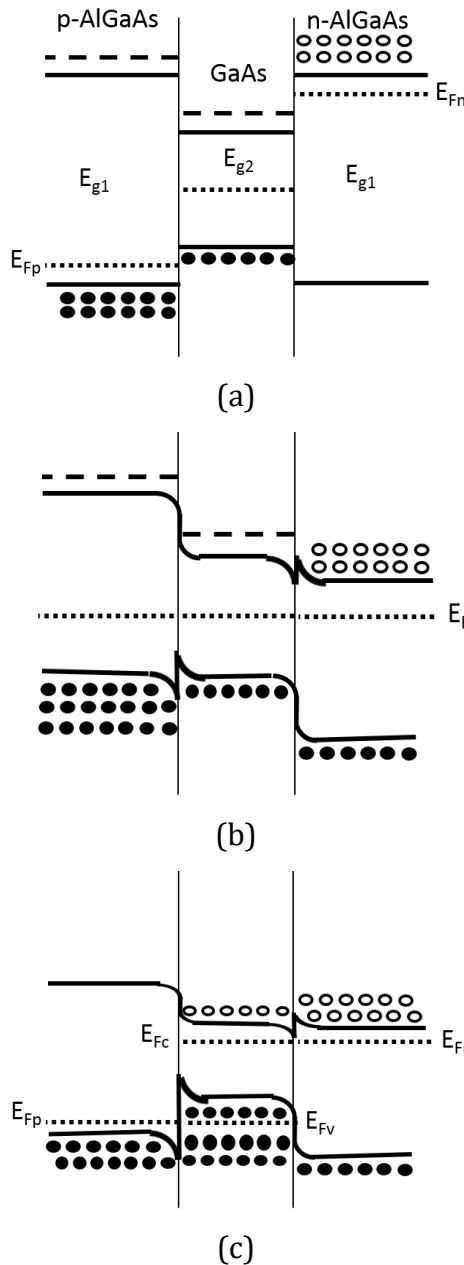


Figure 2.11 : Energy band diagram corresponding to the three-region of double heterostructure laser (a) when they are not in contact, (b) when they are in contact with no bias and (c) under forward bias.



When a laser diode is operated, the gain occurs in a localised spatial region as the device is pumped near threshold. The distribution of light from across a wide spatial region tends to narrow due to the enhanced amplification, where the population inversion is highest. The narrowing of the near field (see section 2.4.1) leads to an increase in the far field divergence as the device is pumped from below to above threshold. The emitted laser beam has an approximately planar wave front and a Gaussian intensity profile. The laser beam diameter is defined as the value at which the intensity has dropped to  $1/e$  of its peak value. The far field begins at a distance,  $z$ , defined by

$$z = \frac{\theta}{\lambda}$$

Equation 2.19

where  $\theta$  is the beam diameter at the exit aperture and  $\lambda$  is the wavelength of the emitted light. Figure 2.12 shows the laser beam divergence in near field and far field.

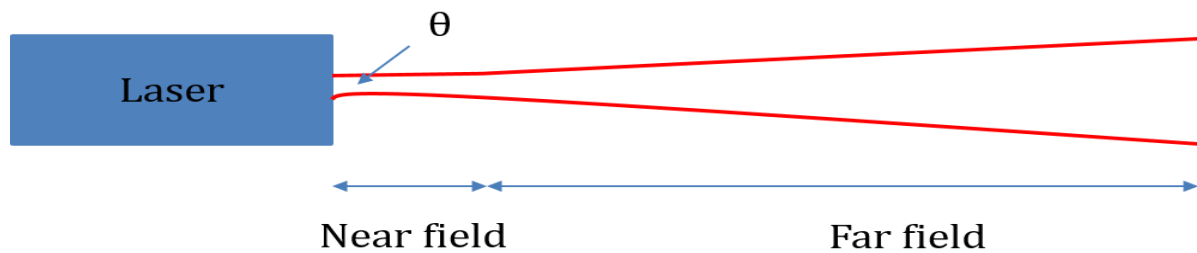


Figure 2.12 : Laser beam divergence in near field and far field.

### 2.3.4 Quantum Confinement

Many semiconductor lasers now use either single or multiple quantum wells or quantum dot in double heterostructure design. Quantum well and quantum dot are simply heterostructure where the thickness of the layer is decreased such that quantum confinement effects become apparent.

### 2.3.4.1 Quantum Well

The low bandgap semiconductor surrounded by higher bandgap semiconductor leads to the formation of a potential well that can trap electrons and holes. When the active layer thickness in the heterostructure laser is reduced to the order of the de Broglie wavelength ( $\lambda = h/p$ ), carriers motion normal to the active layer in these structures is restricted. This results in the kinetic energy of the carriers moving in that direction being quantized into discrete energy levels. These types of lasers are called quantum well lasers. The thickness of active medium in quantum well laser is typically about 100 Å, or about 40 atomic layers.

The resulting quantisation of the energy levels within the well increases the transition energy as compared to that of the bulk material. As the energy levels depend on the thickness of the well, by adjusting this thickness, the transition energy and hence the lasing wavelength can be altered [6] [7]. This provides considerable flexibility in manufacturing laser diodes for particular applications.

Another advantage of the quantum well laser is that it delivers more gain per injected carrier than that of a bulk laser. This is due to the confinement restricting the number of states available for transition within the gain spectrum. The more well-defined energies of the quantum well levels results in lower threshold currents [7] [8] and reduced its temperature dependence [8].

In a quantum well, the energy of the carrier across the well is quantized with the associated carriers' energies having discrete values. However, in the plane of the well the carriers are free to move. This leads to a step-like density of state functions as shown in Figure 2.13.

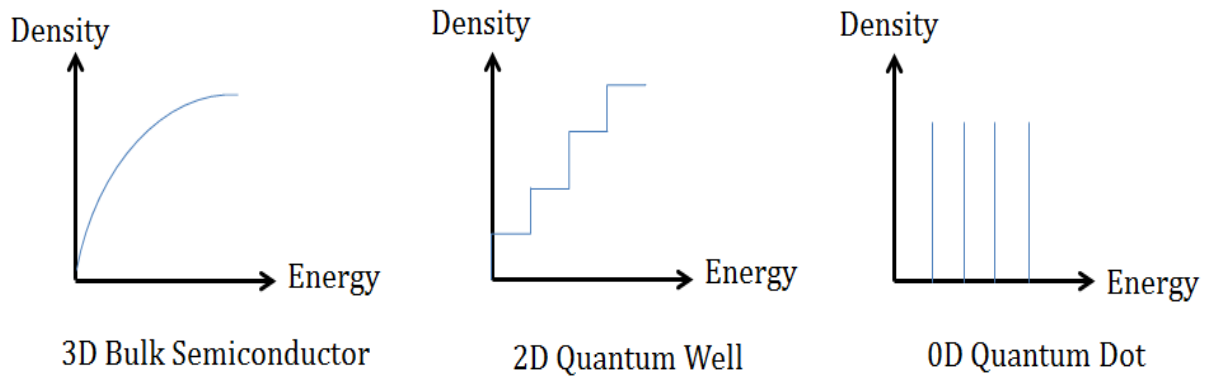


Figure 2.13 : Density of state as a function of structure size.

### 2.3.4.2 Quantum Dot

After the success of one dimensional quantization, the next step was to reduce the dimensionality to three dimensional quantum dot. The carriers are now confined in all three dimensions of space by surrounding material with a larger bandgap. The energy levels are now obviously discrete as in atoms with a delta function density of states. The typical dimension of the quantum dot is around 1 - 10 nm so that the quantization effect will be apparent. Although it has atomic like energy levels and the resulting properties, it can still contain  $10^4$  or more atoms.

The main advantages of quantum dots as the active region of semiconductor lasers that were originally proposed are:

- i. An improved temperature stability as the energy level separation is greater than that the thermal energy [8].
- ii. Lower threshold current as with fewer possible states less charge carriers are needed for population inversion [8] [9].
- iii. A narrow spectral linewidth as the discrete energy spectrum allows highly efficient laser action at a distinct energy.
- iv. Increased in differential gain [10].

The gain required to reach threshold (overcome the losses) is given by Equation 2.6. This gain must be achieved in a material as the difference between stimulated emission and absorption by increasing the population inversion. I evaluate the gain that can be achieved in the next chapter.

## 2.4 Coupled Cavity Laser System

In this work, the coupled cavity laser system will be developed. Generally, there are two categories of such system. They can be referred to as active-passive and active-active arrangements. It depends on whether the second cavity can be externally pumped or not. The active-active arrangements have an advantage of having additional degree of freedom that can be used to control the behavior of the device.

The threshold gain requirement of a single cavity laser, as described by Equation 2.6, to the first order, is independent of wavelength. Hence, each of the allowed cavity mode will have the same value of threshold gain. On the other hand, for the coupled cavity laser system, the threshold gain requirement of a given mode will depend on the gain or loss that it experiences in each of the laser section as well as the optical feedback that take place within the gap coupler. The light entering the gap coupler from each of active section will be reflected backward and forward multiple times. A fraction of a resonant light will leak back into the active section of the device for every internal reflection. Consequently, the strength and phase of coupling between the two laser sections is wavelength dependent.

To analyze the coupling between the two cavities, we consider general case that is applicable for both active-passive and active-active arrangement device. Figure 2.14 shows the geometry of coupled cavity laser system. The coupling of light between the cavities with length  $L_1$  and  $L_2$  is affected by the loss and phase shift experienced by the optical field while traversing the gap coupler with length  $L_G$ .  $r$  and  $r'$  are the amplitude of reflectivity coefficients for the respective facets.  $E'_1$  and  $E'_2$  are the amplitudes of the

electric fields that enter each of the laser cavities from the gap coupler. The gap coupler is characterized by a scattering matrix ( $S$ ). The transmission and reflection of electric fields  $E_1$  and  $E_2$  in the two cavities can be described by the following relation:

$$\begin{pmatrix} E'_1 \\ E'_2 \end{pmatrix} = \begin{pmatrix} S_{11} & S_{12} \\ S_{21} & S_{22} \end{pmatrix} \begin{pmatrix} E_1 \\ E_2 \end{pmatrix}$$

Equation 2.20

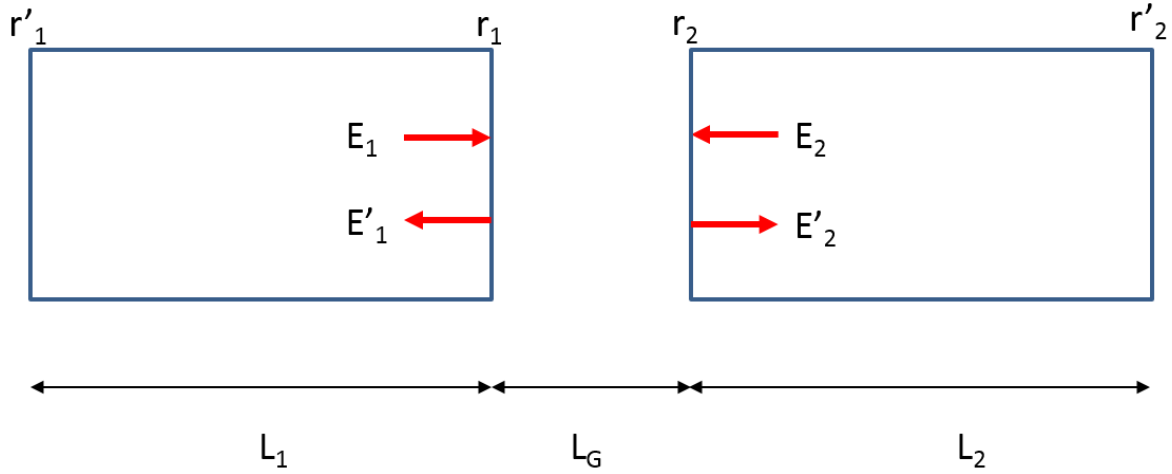


Figure 2.14 : Coupled cavity laser geometry.

The scattering matrix elements can be obtained by considering the light reflected back from the gap into the cavity of origin, combined with light transmitted through the gap from the opposite cavity. Each of these contributions itself comes from multiple round trips inside the gap coupler. For a symmetric device, i.e.  $L_1 = L_2$ , with an air gap coupler of width  $L_G$ , the scattering matrix elements are as follows:

$$S_{11} = r_1 - \frac{r_2(1 - r_1^2)t_G}{1 - r_1r_2t_G}$$

Equation 2.21

$$S_{22} = r_2 - \frac{r_1(1 - r_2^2)t_G}{1 - r_1r_2t_G}$$

Equation 2.22

$$S_{12} = S_{21} = \frac{[t_G(1 - r_1^2)(1 - r_2^2)]^{1/2}}{1 - r_1 r_2 t_G}$$

Equation 2.23

where  $t_G$  is a propagation coefficient that describes the phase dependence of the amplitude after a single pass of the gap coupler.  $t_G$  is given by the following equation:

$$t_G = \exp\left(\frac{i2\pi L_G}{\lambda_G}\right)$$

Equation 2.24

where  $\lambda_G$  is the wavelength of light inside the gap coupler. Substantially the gap has been replaced by an interface with effective reflection coefficients are  $S_{11}$  and  $S_{22}$ . Meanwhile,  $S_{12}$  and  $S_{21}$  are the effective transmission coefficient from cavity 1 to cavity 2 and vice versa. The strength and phase dependence of the coupling can be expressed in the form of complex coupling parameter which is define as the ratio of the complex transmission and reflection coefficient:

$$\hat{C} = C \exp(i\theta) = \left(\frac{S_{12}S_{21}}{S_{11}S_{22}}\right)^{1/2}$$

Equation 2.25

Where  $C$  is the coupling magnitude and  $\theta$  is the coupling phase. Based on Equation 2.21 to Equation 2.25, the coupling of light between cavities depends on  $t_G$ , and both  $C$  and  $\theta$  vary with the width of the gap  $L_G$ . The assessment of  $C$  and  $\theta$  requires knowledge of the gap loss that arises mainly from the diffraction spreading of the beam inside the gap. This can be investigated with the analysis of far field diffraction of the light beam between the cavities.

### 2.4.1 Far Field Diffraction In The Coupled Cavity Laser Systems

The near field of the laser beam is the region around the beam waist that is emitted from the waveguide [2]. The far field refers to the beam profile far from the beam waist as compared to the effective Rayleigh length. In a coupled cavity laser system developed in

this work, the far field intensity profile, allows the strength of light from the source laser cavity after travelling through the microfluidic channel that will be coupled into the opposite detector laser to be computed. Figure 2.15 shows the schematic diagram of the far field divergence as the lasing transverse mode leaves the laser source waveguide.

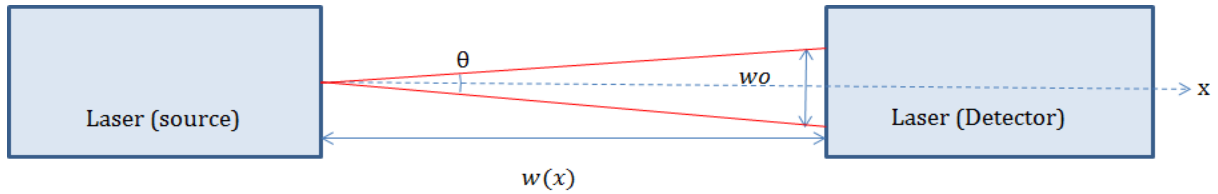


Figure 2.15: Schematic diagram of the far field beam divergence as the lasing transverse mode leaves the laser source waveguide.

As seen in Figure 2.15, the total mode width in the active medium is given by  $w_0$  and the distance between the source and the detector is given by  $w(x)$ . Hence, the angular divergence at which the fraction of light from the source coupled into the detector  $\theta$  in radian is given by:

$$\theta = \frac{w_0}{w(x)}$$

Equation 2.26

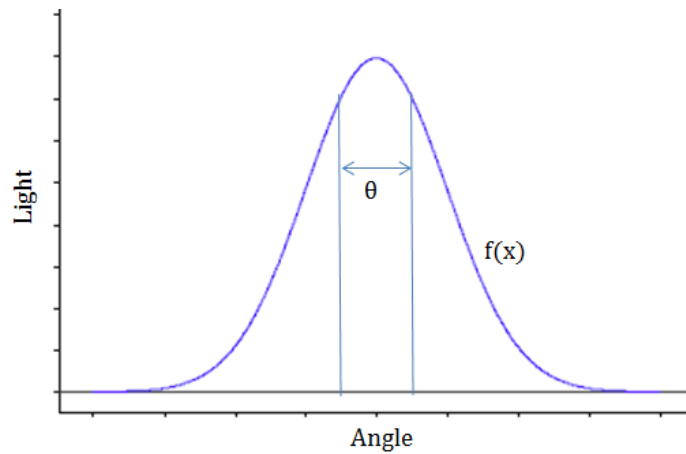


Figure 2.16 : Schema of the far field light distribution.

Therefore, the fraction of light emerging from the laser source that is coupled into the detector after travelling a distance  $x$  is given by:

$$F(x) = \frac{\int_{-\theta^o}^{\theta^o} f(x)}{\int_{-90^o}^{90^o} f(x)}$$

Equation 2.27

where  $f(x)$  is the far field function of the emerging light from the laser source.



## 2.5 Bibliography

- [1] W. W. Chow and S. W. Koch, *Semiconductor Laser Fundamentals : Physics of the Gain Materials*, Berlin: Springer, 1999.
- [2] L. A. Coldren, S. W. Corzine and M. L. Mashanovotch, *Diode Laser and Photonic Integrated Circuit*, New Jersey: Wiley, 2012.
- [3] T. Suhara, *Semiconductor Laser Fundamentals*, New York: CRC Press, 2004.
- [4] W. J. Wadsworth, "University of Oxford. Department of Physics," [Online]. Available: <http://www.physics.ox.ac.uk/al/research/groups/laser/diodes.html>. [Accessed 7 January 2015].
- [5] M. P. H.C. Casey Jr., *Heterostructure Lasers, Part A : Fundamental Principles*, New York San Fransisco London: Academic Press, 1978.
- [6] G. P. Agrawal and Niloy K Dutta, *Semiconductor Laser*, New York: Van Nostrand Reinhold, 1993.
- [7] J. Peter S. Zory, *Quantum Well Lasers*, San Diego: Academic Press, Inc., 1993.
- [8] P. Smowton and P. Blood, "Quantum Dot Lasers : Theory and Experiment," in *VLSI Micro- and Nanophotonics: Science, Technology, and Applications*, CRC Press, 2011, pp. 9-1 - 9-35.
- [9] V. M. Ustinov, A. E. Zhukov, A. Y. Egorov and A. N. Maleev, *Quantum Dot Lasers*, New York: Oxford University Press, 2003.
- [10] G. M. Lewis, J. Lutti, P. M. Smowton and P. Blood, "Optical Properties of InP/GaInP quantum dot laser structures," *Applied Physics Letters*, vol. 85, no. 11, pp. 1904 - 1906, 2004.
- [11] M. E. Fabian, *Semiconductor laser diodes : a users handbook*, Ayr, Scotland: Electrochemical Publications, 1981.

- [12] J. F. B. H. J Wilson, Lasers : principles and applications, New York London: Prentice Hall, 1987.
- [13] E. Hecht, Optics : 4th Edition, San Fransisco: Addison Wesley, 2002.

## Chapter 3 : Active Medium

### 3.1 Introduction

The active medium is the source of optical gain in a laser. It is a material with properties that allow it to amplify light by stimulated emission. There are varieties of material for active medium that are used in semiconductor lasers. For example gallium arsenide (GaAs), indium gallium arsenide (InGaAs) or gallium nitride (GaN). The thickness of active medium plays an important role as it becomes similar to the electron wavelength because it will modify the density of energy levels available for electrons and holes.

A quantum well active region is formed when the thickness of the active medium of the laser is reduced to the order of the de Broglie wavelength ( $\lambda = h/p$ ), typically at 100 Å. Carriers motion normal to the active layer in these structures is restricted. This restriction results in the kinetic energy of the carriers moving in that direction is quantized into discrete energy levels. A quantum well delivers more gain per injected carrier than conventional lasers, which results in lower threshold currents [1].

If the active region is further reduced to the point that the carrier motion is restricted in all three dimensions, the quantum dot active region is produced. The energy levels are now discrete as in atoms, although with smaller energy separation. The typical dimension of the quantum dot is around 1 - 10 nm so that the quantization effect will be apparent. The population inversion for lasing occurs more efficiently as the active layer material is scaled down from a bulk semiconductor to quantum dots. Therefore, quantum dots can provide much lower threshold current density at low loss as compared to the quantum well [2].

For the fabrication of the prototype of coupled cavity living laser, having an active medium that will exhibit maximum gain at a low current density with a low value of internal optical mode loss over a wide range of temperature is desirable. While a broad gain spectrum will give advantage for wavelength tuning later on. Nonetheless, an active medium that is able to produce sufficient gain to tolerate a considerable amount of loss due to difficulties in facet formation and cleaving process is more preferable. Therefore, this chapter presents the characterization of quantum well and quantum dot as the active medium. The multisection technique measurement has been done over a certain range of temperature for this purpose. The early part of this chapter presents the experimental techniques used to obtain the results of this thesis. Details of the multisection device and the measurement principle is discussed. The device check tests are explained as well as the experimental procedure for multisection technique.

The materials used for this study are UWIC 412 1608c AlGaInP single quantum well and MR2459 main GaInP quantum dot. The exact layer structure of the single quantum well wafer is proprietary information so cannot be included. Table 3.1 shows the layer structure of the MR2459 Main quantum dot wafer. Results obtained from these measurements will be discussed in the following sections. Finally, the best active medium for fabrication of a coupled cavity living laser will be suggested in Section 3.4.

Table 3.1 : Layer structure of MR2459 Main quantum dot wafer.

Layer no.	Material	x	Thickness (Å)	Ts	Dopant type	Conc
1	GaAs	-	3000	690	p	8e18
2	GaInP	-	100	690	p	2e18
3	Al(x)GaInP	1 to 0	200	690	p	3e17
4	AlInP	-	10000	690	p	3e17
5	(Al(x)Ga)InP	0.30	1000	730	Ud	-
6	GaIn(x)P	0.49	80	730	Ud	-
7	InP	-	6	730	Ud	-
8	(Al(x)Ga)InP	0.30	160	730	Ud	-

9	GaIn(x)P	0.49	80	730	Ud	-
10	InP	-	6	730	Ud	-
11	(Al(x)Ga)InP	0.30	160	730	Ud	-
12	GaIn(x)P	0.49	80	730	Ud	-
13	InP	-	6	730	Ud	-
14	(Al(x)Ga)InP	0.30	160	730	Ud	-
15	GaIn(x)P	0.49	80	730	Ud	-
16	InP	-	6	730	Ud	-
17	(Al(x)Ga)InP	0.30	160	730	Ud	-
18	GaIn(x)P	0.49	80	730	Ud	-
19	InP	-	6	730	Ud	-
20	(Al(x)Ga)InP	0.30	1000	730	Ud	-
21	AlInP	-	10000	690	n	1e18
22	Al(x)Ga)InP	0 to 1	200	690	n	1e18
23	GaInP	-	100	690	n	2e18
24	GaAs		3000	690	n	8e18

## 3.2 Multisection Technique

The multisection technique or segmented contact method (SCM) [3] is a method of analyzing the single pass amplified spontaneous emission (ASE). It enables the extraction of modal gain and modal absorption from the ASE spectra. I used this technique to obtain gain and absorption spectra to characterize and compare the gain media of quantum well and quantum dot material.

### 3.1.1 Multisection Device

Figure 3.1 shows the schematic diagram of a multisection device structure. Multisection devices fabricated for this work are based on oxide isolated stripe geometry with a 50  $\mu\text{m}$  stripe width. The top electrical contact of the device is segmented into sections of 300  $\mu\text{m}$  that can be electrically pumped separately. The metallic contact and capping layer of the device which are highly conductive are chemically etched to maximize electrical isolation and minimize current spreading between sections. To ensure the device only provides single pass ASE spectra, the device is processed to have 10° angled facets as well as leaving some of the sections at the back of the sample unpumped to prevent the feedback process.

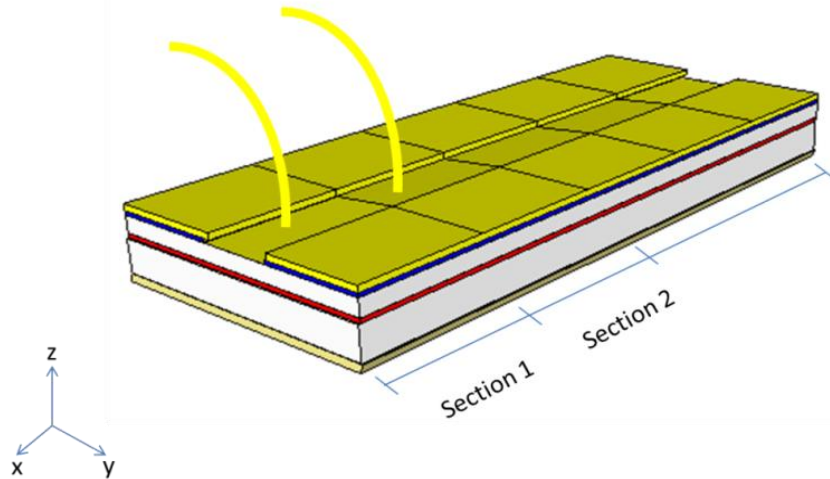


Figure 3.1 : Schematic diagram of a 50  $\mu\text{m}$  stripe multisection device (not to scale).

### 3.1.2 Multisection Technique Measurement Principle

If the total spontaneous emission rate for light of a specific polarization is  $I_{\text{spont}}$ , then the emission rate emitted at the end of the waveguide with the thickness of  $\Delta x$  after passing a distance  $x$  along the active region is:

$$I(x) = \beta I_{\text{spont}} e^{(G - \alpha_i) \Delta x}$$

Equation 3.1

where  $\beta$  is the fraction of the total spontaneous emission that is coupled into the waveguide,  $G$  is the modal gain and  $\alpha_i$  is the internal optical loss. We assume that  $I_{spont}$  is uniform along the waveguide and the total ASE of this polarization emerging from a length  $L$  of pumped material with the units of photons per second per unit stripe width per unit energy interval is:

$$I(L) = \int_0^L \beta I_{spont} e^{(G-\alpha_i)x} dx = \beta I_{spont} \frac{e^{(G-\alpha_i)L} - 1}{G - \alpha_i}$$

Equation 3.2

The measured ASE can be described in three situations:

- i.  $I(1)$  when only section 1 is pumped:

$$I(1) = (\beta I_{spont}) \left( \frac{e^{(G-\alpha_i)L} - 1}{G - \alpha_i} \right)$$

Equation 3.3

- ii.  $I(1+2)$  when section 1 and 2 are pumped:

$$I(1 + 2) = (\beta I_{spont}) \left( \frac{e^{(G-\alpha_i)2L} - 1}{G - \alpha_i} \right)$$

Equation 3.4

- iii.  $I(2)$  when only section 2 is pumped:

$$I(2) = (\beta I_{spont}) \left( \frac{e^{(G-\alpha_i)L} - 1}{G - \alpha_i} \right) e^{(-A-\alpha_i)L}$$

Equation 3.5

with the length of section 1 and 2 are the same and referred as  $L$  and  $A$  is the modal absorption in the unpumped section 1.

The net modal gain is given by Equation 3.4 divided by Equation 3.3 which gives:

$$(G - \alpha_i) = \frac{1}{L} \ln \left( \frac{I(1 + 2)}{I(1)} \right)$$

Equation 3.6

The net modal absorption is given by Equation 3.3 divided by Equation 3.5 which gives:

$$(A + \alpha_i) = \frac{1}{L} \ln\left(\frac{I(1)}{I(2)}\right)$$

Equation 3.7

The examples of typical measured ASEs are shown in Figure 3.2.

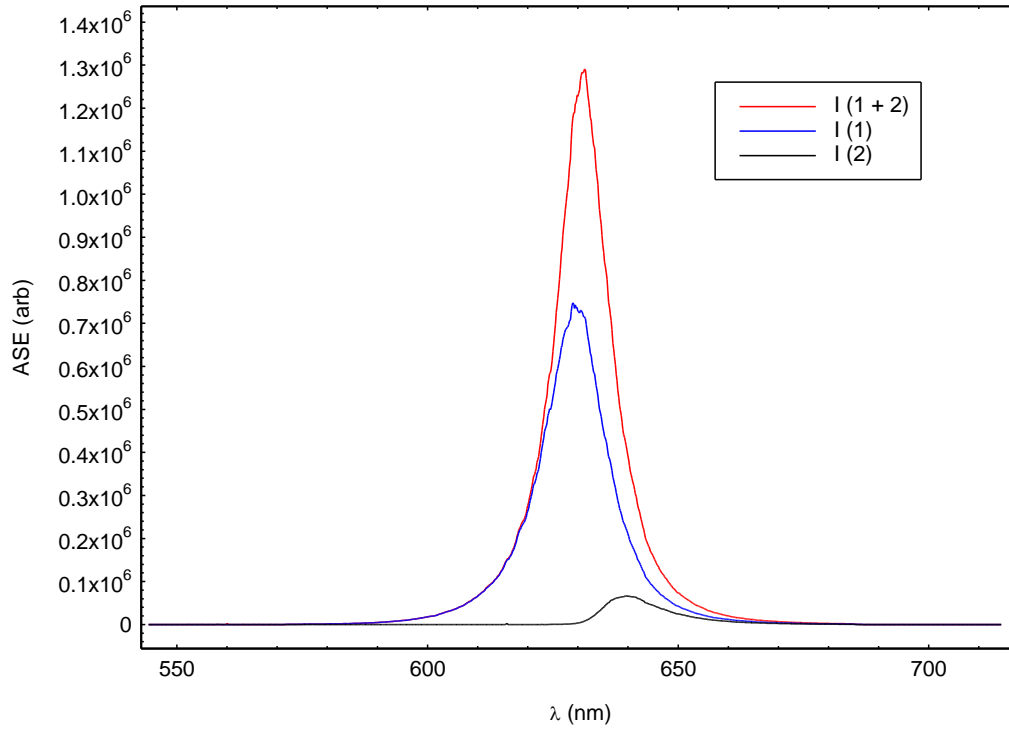


Figure 3.2 : The exemplary ASE spectra of a quantum well multisection device.

Figure 3.3 shows the examples of modal gain and absorption obtained from ASE using Equation 3.6 and Equation 3.7. The internal optical loss  $\alpha_i$  is extracted from the low energy region where the gain and absorption spectra meet. In this region, there is no gain or absorption, so the loss here is due to internal optical loss.



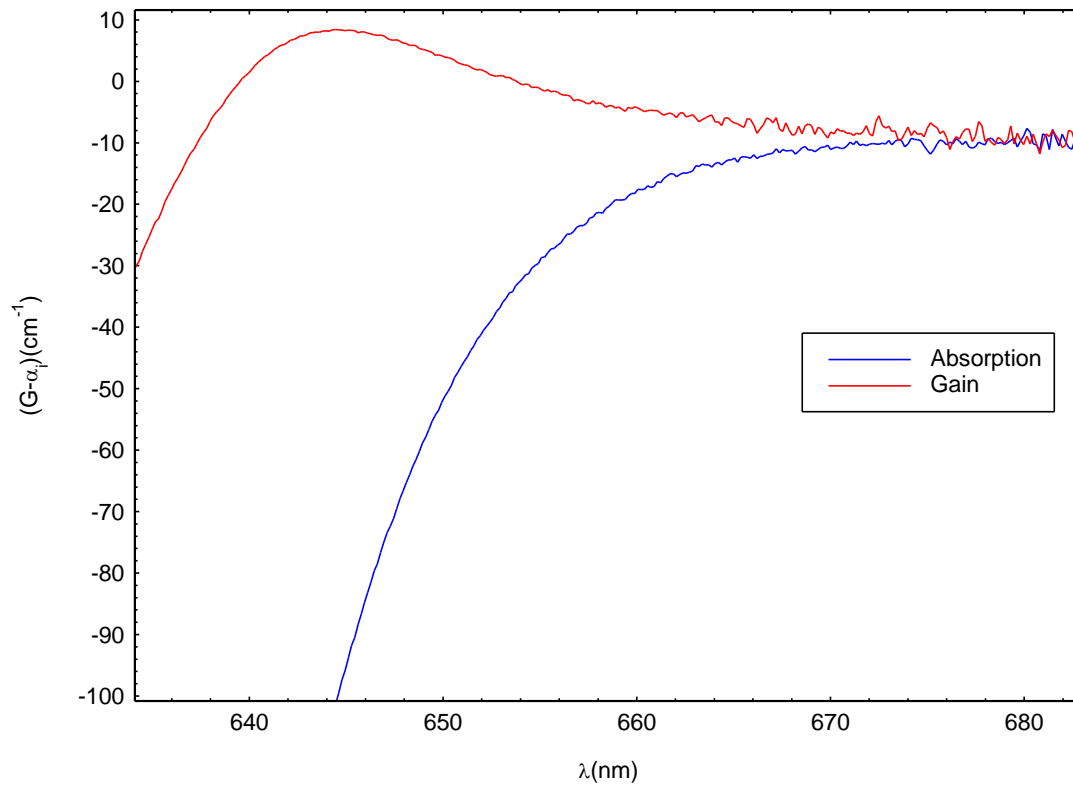


Figure 3.3 : Exemplary modal gain and absorption curves obtained from amplified spontaneous emission spectra of a quantum well material.

### 3.1.3 Device Checks

Prior to multisection technique measurement, some preliminary checks are done on the devices to ensure the results will be meaningful.

#### 3.1.3.1 Visual Inspection Of The Facets

The first check is a visual inspection of the facet under the microscope before attaching the wires to the sections. It is important that the front facet is mirror like especially in the area beneath the stripes where the ASE is emerging as any imperfection can scatter the light.

### 3.1.3.2 Intercontact Resistance

The intercontact resistance between sections should be at least  $200\ \Omega$  to ensure that there will be minimal current leakage from one section to another when one of them is being pumped.

### 3.1.3.3 Light – Current – Voltage (LIV) Measurement

The current – voltage (IV) and light - current (LI) characteristic of the device has been measured using light – current – voltage (LIV) experimental setup as shown in Figure 3.4. The red line shows the light path and black lines show electrical connections. The measurement is taken at room temperature. The device is held in the device holder and the light is detected by the photodiode sensor. The pulse generator is used to supply current to the device. The resulting pulsed light, current and voltage are all measured at the boxcar integrator that provides gated measurement triggered by the pulse generator. These measured values are recorded by a computer which increments in the current supplied to the device via the current controller and the measurement are all repeated. This measurement loop is repeated until the light measurement reached a preset limit.

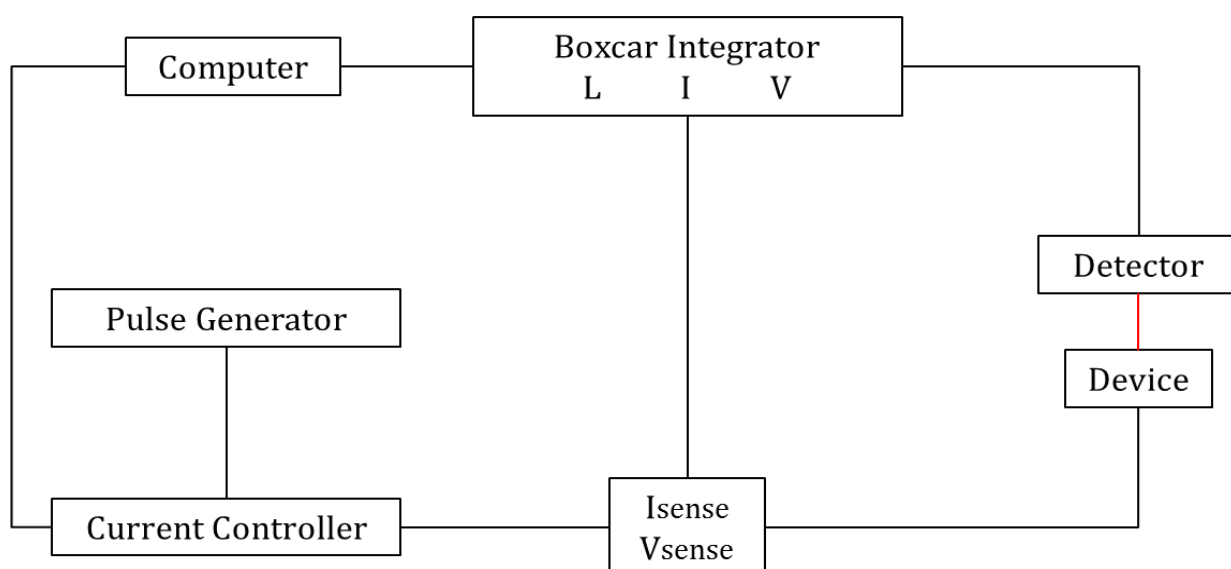


Figure 3.4 : Schematic diagram of experimental set up for light - current - voltage (LIV) measurement. The red line shows the light path and the black lines show electrical connections.

The current density of each section should be identical and this is most easily achieved when each section has an identical IV characteristic. Differences not more than 3% can still be tolerated. Any difference indicates the presence of extra current paths within the device or a difference in resistance which implies that the two sections are not identical. The IV characteristics of the two sections must be within this tolerance to ensure that the same current is applied to each section during segmented contact method measurement. Figure 3.5 shows the exemplary IV characteristic for section 1 and section 2 of a multisection device, in this example a quantum dot multisection.

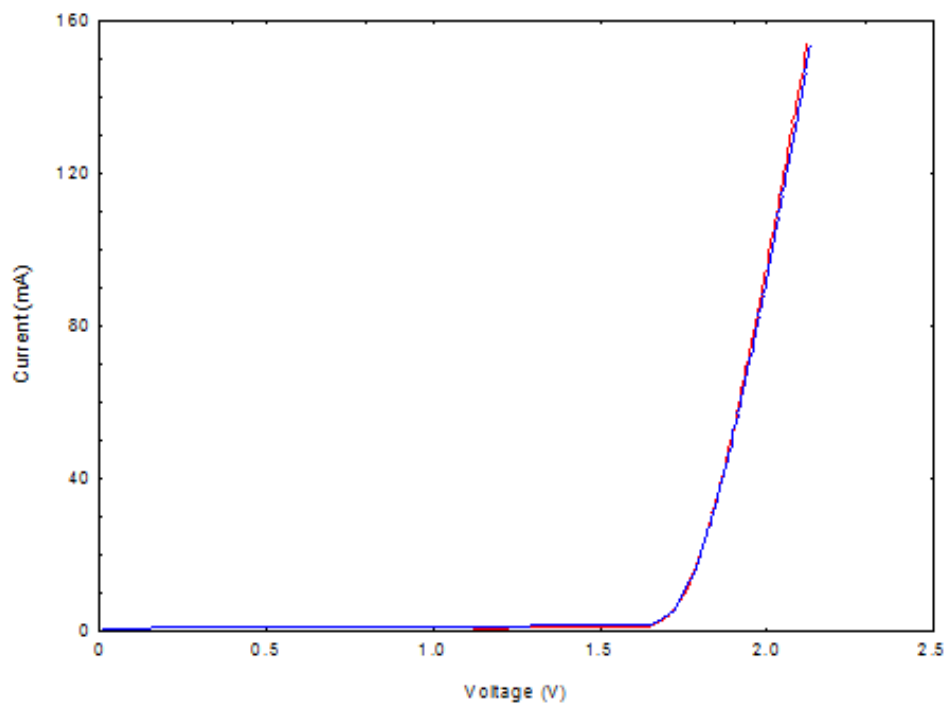


Figure 3.5 : I-V characteristic for section 1 (blue) and section 2 (red) of a multisection device.

### 3.1.3.4 Near Field Measurement

Near field refers to the field emitted from the laser waveguide [4], in this case this is the distribution of light intensity at the facet of the multisection device. The near field measurement can be used to check if there is any damage in the active region across the device facet and to ensure the optical mode for each section is identical. The width of the

active region where current flows can be estimated by measuring the full width half maximum (FWHM), allowing a determination of the current density.

Figure 3.6 shows the schematic diagram of the experimental set up for the near field measurement. The red line shows the light path and the black lines show electrical connections. A pulsed current with 1000 ns width and 2 kHz repetition rate is supplied to multisection device by the pulse generator. The section controller is used to selectively pump either section 1 or section 2 or both sections of the multisection device. The light emitted from the device then focuses on the CCD camera by the focusing lens. A set of neutral density filter is used to avoid saturation limit of the emitting light in the CCD camera. The CCD camera captures the image of the near field distribution which then will be analyzed using Easyplot software.

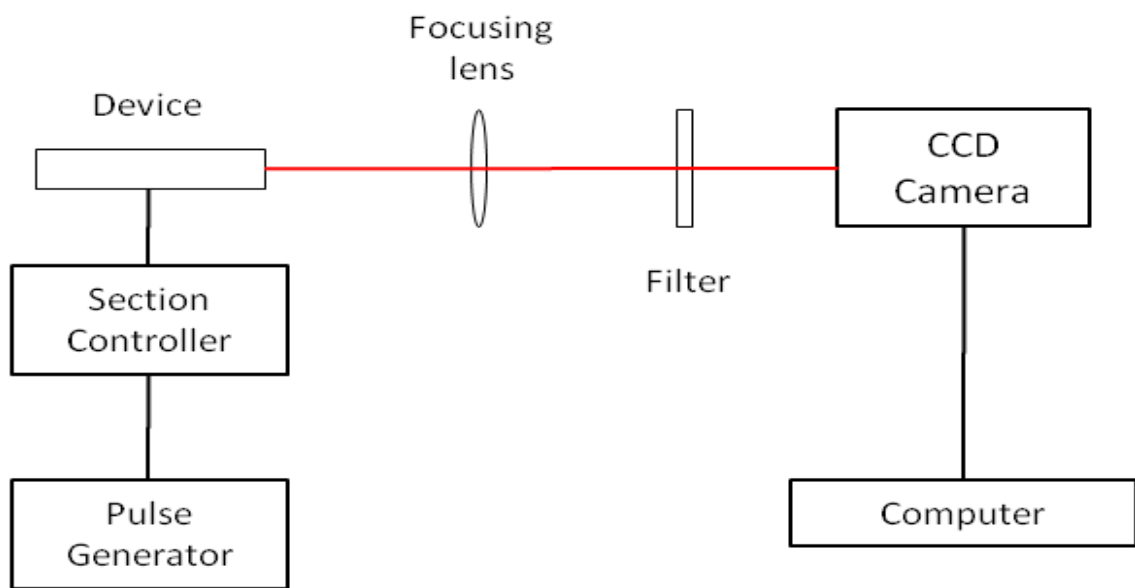


Figure 3.6 : Schematic block diagram of near field experimental setup.

Figure 3.7 shows the exemplary (a) uniform and (b) non uniform near field emission for a multisection device. The FWHM of the distribution which indicates the width of the active region is calculated by converting the pixel number to the real unit.

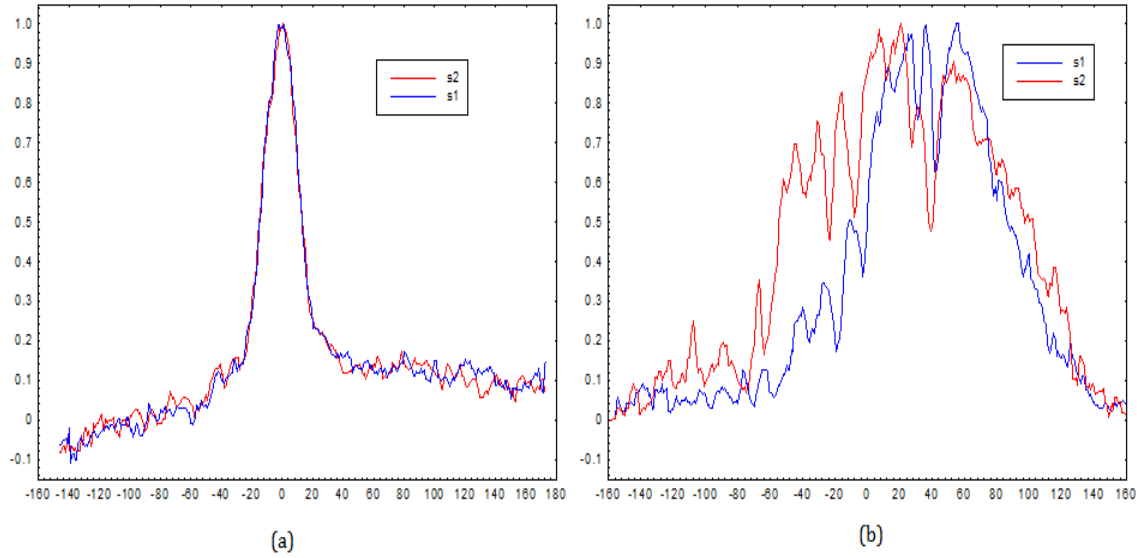


Figure 3.7 : Exemplary (a) uniform and (b) non uniform near field distribution of a multisection device.

### 3.1.4 Experimental Procedure

Samples were fabricated into 50  $\mu\text{m}$  wide oxide-isolated stripe multisection test structures and lasers. All devices have uncoated cleaved facets and were operated pulsed, with pulse length of 1000 ns and duty cycle of 0.1% to avoid self-heating. Measurement using the segmented contact method allow us to determine the net modal gain spectra and the optical loss spectra, the latter being the sum of the modal absorption and internal optical mode loss,  $\alpha_i$ .

The multisection device, that has passed the device checks described earlier, and that has been mounted onto a transistor header as in Figure 3.8 is placed into a vacuum cryostat. This allows the measurement to be taken at constant temperatures within the range of 260K to 360K. The crystal is mounted onto a micro positioning stage that has six degrees of freedom that allow the ASE from the front facet of the device to be accurately aligned to the slit of the spectrograph. The device in the cryostat is connected to pulse generator via a switch box. The switch box allows each section to be pumped separately. The current applied to each section is measured on an oscilloscope. Pulsed current is applied throughout the experiment to avoid self-heating of the device.

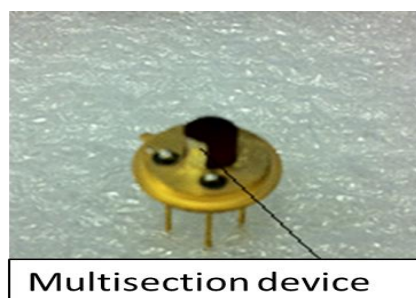


Figure 3.8 : A multisection device is mounted onto the transistor header.

The ASE from the front facet of the multisection device is collected by a microscope objective lens. It focused the ASE to the entrance slit of the spectrograph. The ASE passes through a polarizer before reaching the spectrograph so that either TE or TM emission can be measured. The signal from the spectrograph is then detected by the CCD camera which attached with a cooler used to maintain stability to work efficiently and minimise noise. The temperature of the sample can be varied by using a temperature controller that regulates the flow of liquid nitrogen into the cryostat using the transfer tube. The experimental setup used for multisection technique is shown in Figure 3.9.

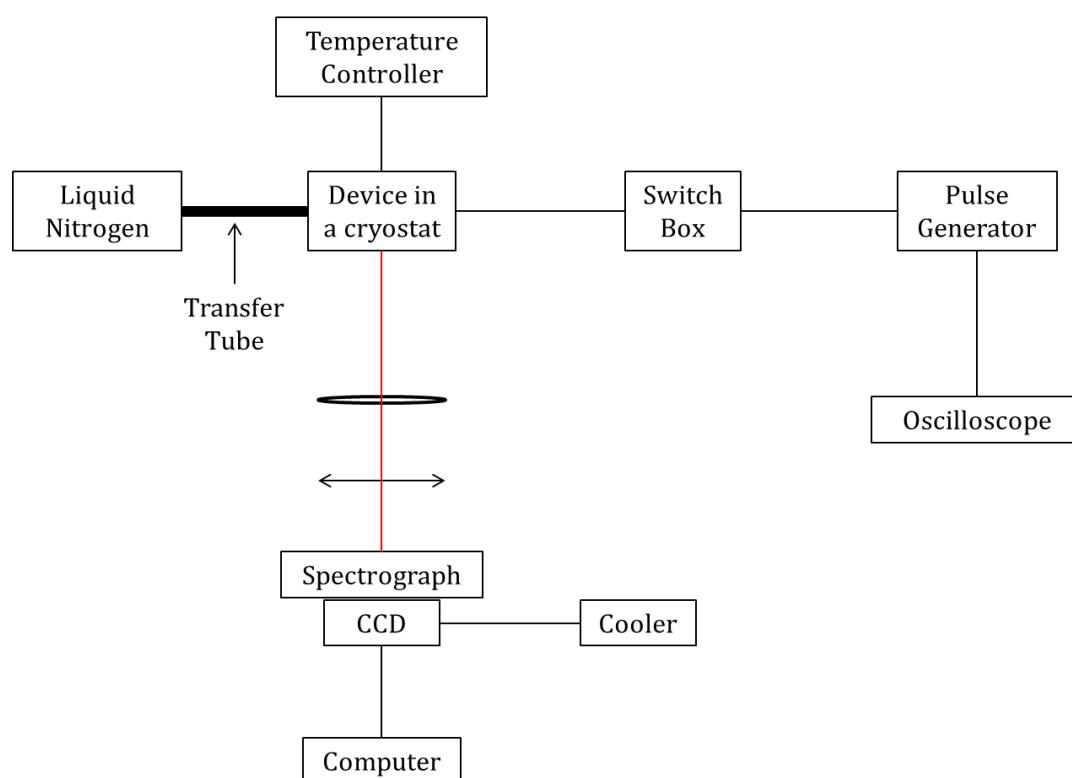


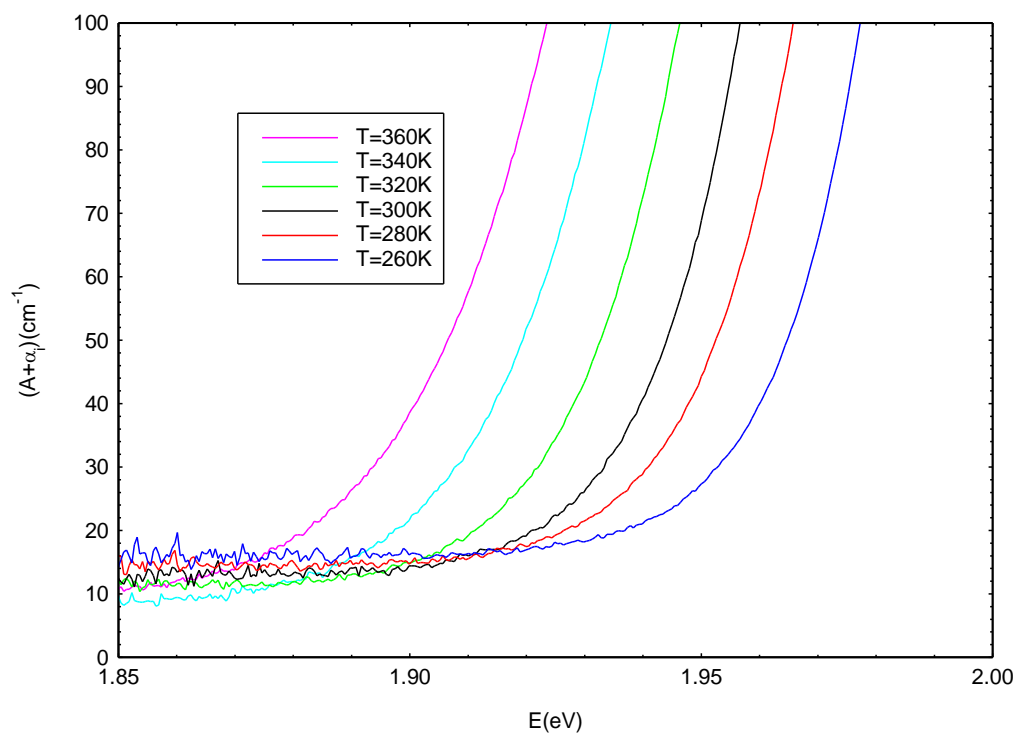
Figure 3.9 : Schematic diagram of experimental setup for multisection technique measurement.

### 3.3 Characterization Of Quantum Well And Quantum Dot Active Media

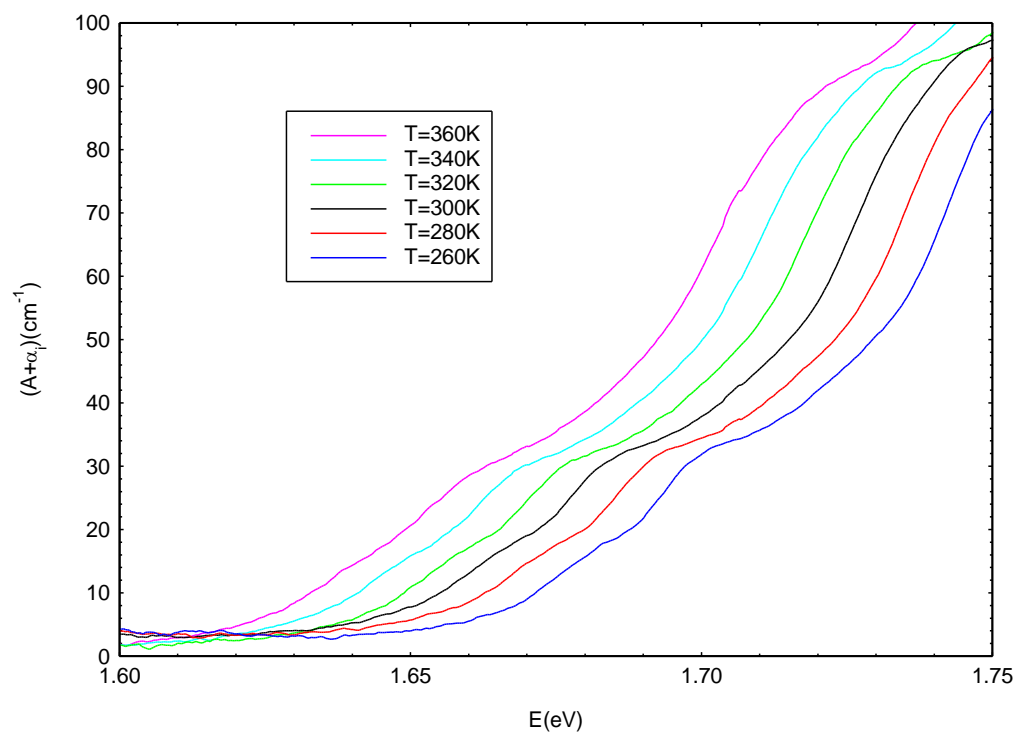
The quantum well and quantum dot material were investigated using multisection technique measurement. The most significant temperature for this study is room temperature, i.e. 300 K. This is because temperature greater than 41.6 °C (314.7 K) to 42.0 °C (315.2 K), which is the critical human body temperature point, may lead to cell death [5]. Meanwhile, there is no destruction of blood cell at the temperature of human body or below [6]. Besides, whole blood can be held at room temperature from 8 up to 24 hours [7] after collection before processing. However, application of low temperature on blood cells requires a slow programmable freezing system or else it may cause cell death as well [8]. Despite all that, the measurement was performed in the temperature range from 260 K to 360 K to observe the behavior of the active medium at a whole range of possible working conditions for the coupled cavity living laser.

#### 3.3.1 Absorption

Figure 3.10 shows the absorption spectra of (a) quantum well and (b) quantum dot samples measured at the temperatures ranging from 260 K to 360 K. The measurement was performed in random order of temperature to avoid any systematic error. The region where each curve goes flat at a low energy indicates the internal optical mode loss,  $\alpha_i$  of the sample. From the result obtained, the  $\alpha_i$  of both samples is the same for each temperature within the uncertainty of the experiment. Quantum well sample exhibits higher value of  $\alpha_i$  which is  $12 \pm 3 \text{ cm}^{-1}$  as compared to quantum dot sample which is  $2 \pm 1 \text{ cm}^{-1}$  at all temperatures. The uncertainty is due to experimental technique uncertainty such as difficulties in obtaining a perfectly aligned device with the best focus and contrast for each measured temperature.



(a)



(b)

Figure 3.10 : Absorption spectra of (a) quantum well and (b) quantum dot multisection devices.



The absorption edge shifts to lower energy with increasing temperature for both samples. This rigid shift reflects the shift in the energy of the constituent bandgap [9] [10]. An increase in thermal energy causes an increase in the amplitude of atomic vibration and consequently an increase in interatomic spacing, which leads to a reduction in the size of the energy bandgap.

### 3.3.2 Modal gain

The net modal gain,  $(G - \alpha_i)$  is the minimum gain required to overcome the mirror losses,  $\alpha_m$ . Figure 3.11 shows the gain and absorption spectra as a function of wavelength of the multisection device with parameters that will be used in the analysis later in this chapter. The transparency energy measured in eV corresponds to the quasi-Fermi level separation of the system in thermal equilibrium. This is the point on the gain spectra on the higher energy side where the modal gain,  $G$  is zero, where the light could propagate in the cavity with no change of light intensity. Absorption edge energy is the value chosen at the half height of the absorption spectra of the sample. Inversion level is the difference between the transparency energy with the absorption edge energy [11] for a given sample of a given current represents the carrier density in the working sample.

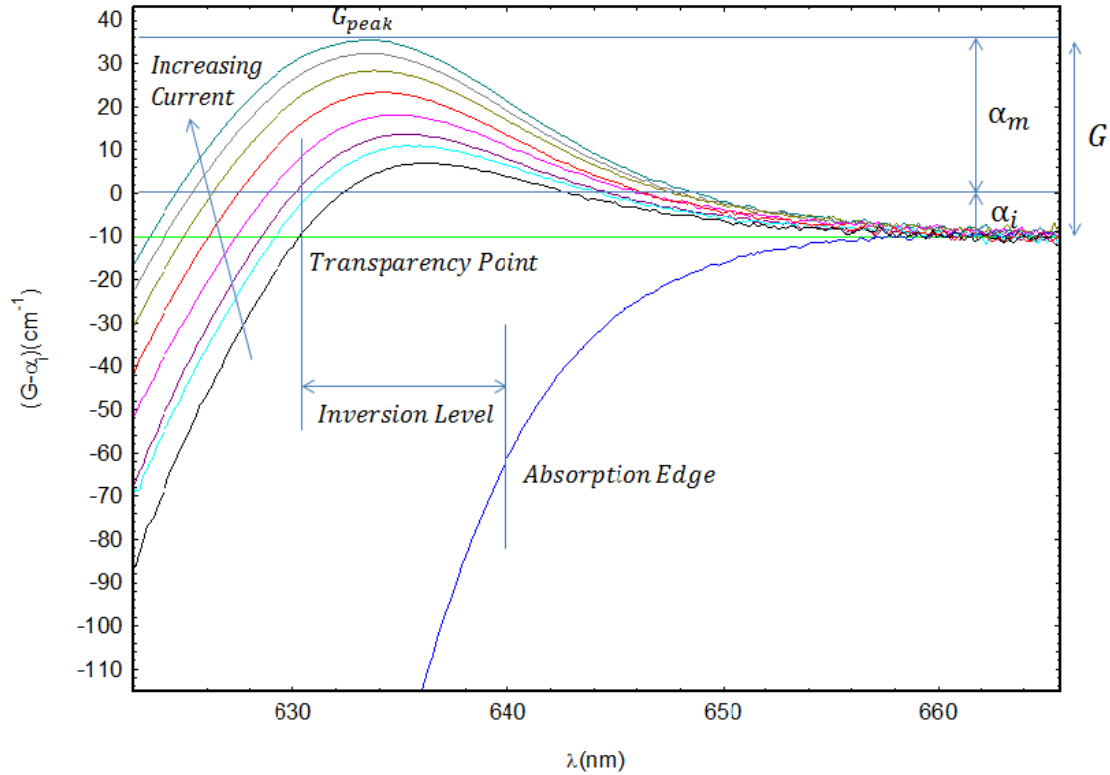
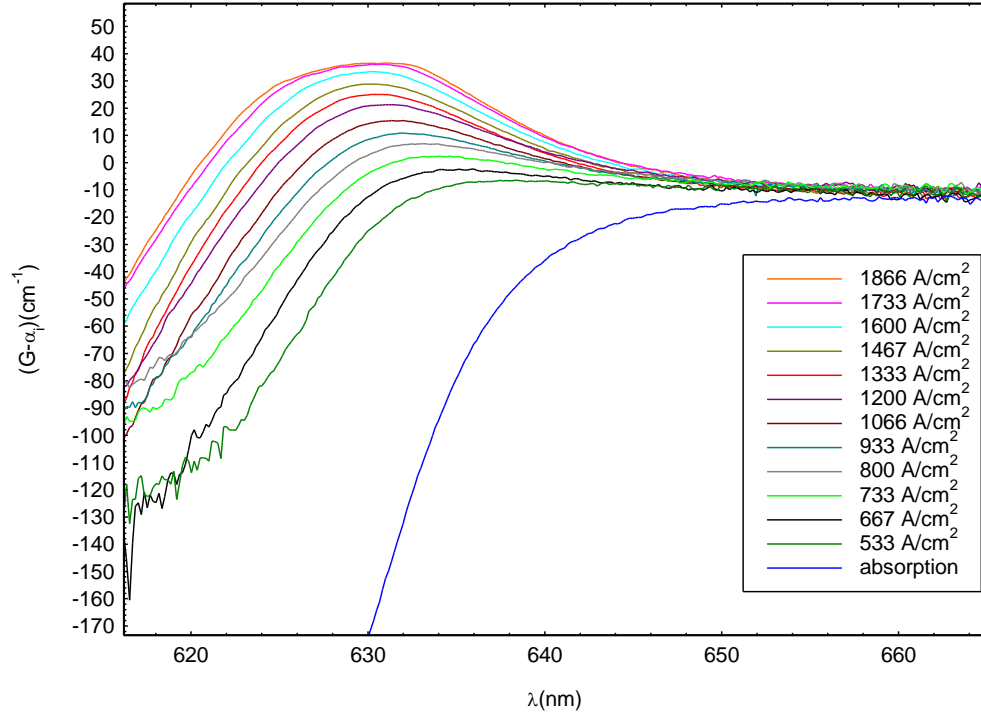
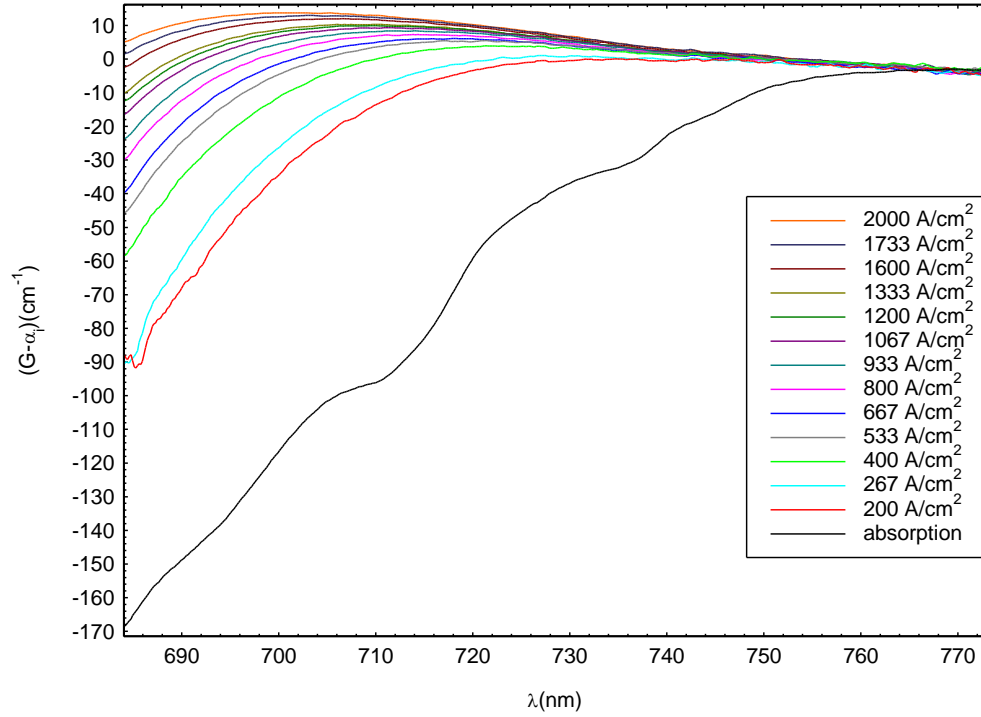


Figure 3.11 : The gain and absorption of the multisection device.

Figure 3.12 shows the net modal gain spectra of (a) quantum well and (b) quantum dot samples as a function of injection current density at room temperature 300K as examples. The measurement was performed at temperatures ranging from 260K to 360K with the pulse width of 1000 ns and 0.1 % duty cycle to avoid self-heating of the device. Quantum well active medium shows transverse magnetic (TM) polarized gain while quantum dot active medium shows transverse electric (TE) polarized gain. TM mode gain arises from the electron – hole recombination between the conduction band to light-hole subband. Meanwhile TE mode gain arises from electron – hole recombination between the conduction band to heavy – hole subbands. The net modal gain spectra for the rest of measured temperatures shows similar curves, but with shift in energy or wavelength as influenced by the operating temperature.



(a)



(b)

Figure 3.12 : Net modal gain spectra of (a) quantum well and (b) quantum dot multisections at room temperature.

The measured gain spectra show an increasing continuous broadening and the peak gain is shifted towards the shorter wavelength region with an increasing of injection current density for both samples. These effects are attributed to the free carrier effect within the active medium. At a low injection current densities, all the carriers are relaxed from the excited state to the ground state and will contribute to the gain at the ground state wavelength. When the injected current density is increasing, the ground state gets more occupied. As a result, the carriers can't relaxed from the excited state to the ground state anymore. Therefore, they are contributing the gain at excited state wavelength. A further increase of injection current will only increase the gain from excited state or even higher energy states.

The other effect that can cause the shift in the gain spectrum is band filling of the inhomogeneously broadened states that occur due the differences in the size, shape, width and composition of dots or in the width and composition of the well in the active medium [12] [13] [14] as well as the carrier relaxation lifetime with regard to energy and momentum [14]. The carrier escape rate from the quantum dot or well to the wetting layer is reliant on the well state or dot size. The carrier capture time from the wetting layer to the dot or well is the same for all the dot or well because it only influenced by the occupation probabilities in the different states. But the escape time of the carrier does depend on the dot size or the well state. This is because the escape time depends on the energy difference of the energy state in the dot or well and the wetting layer. The energy difference in a small dot or well is smaller than it is for a large one caused by the relative higher energy level in the small dot or well. As a result of variation in escape time, the large dot and well will be more populated than the small one at low injection current densities and start to contribute gain at the longer wavelength. When injection current densities are increased beyond the level where the lower energies are already highly populated further increases in population occur mainly in the higher energy states and the spectrum shifts to shorter wavelength or high energy. As more carriers fill the dots or well the renormalization of energy bands increases due to stronger Coulomb attractions that arise from increased number of carriers. This latter effect accounts for a shift of the gain spectrum to longer wavelength. In dots this latter shifter is much smaller than that due to the filling of the higher energy states.

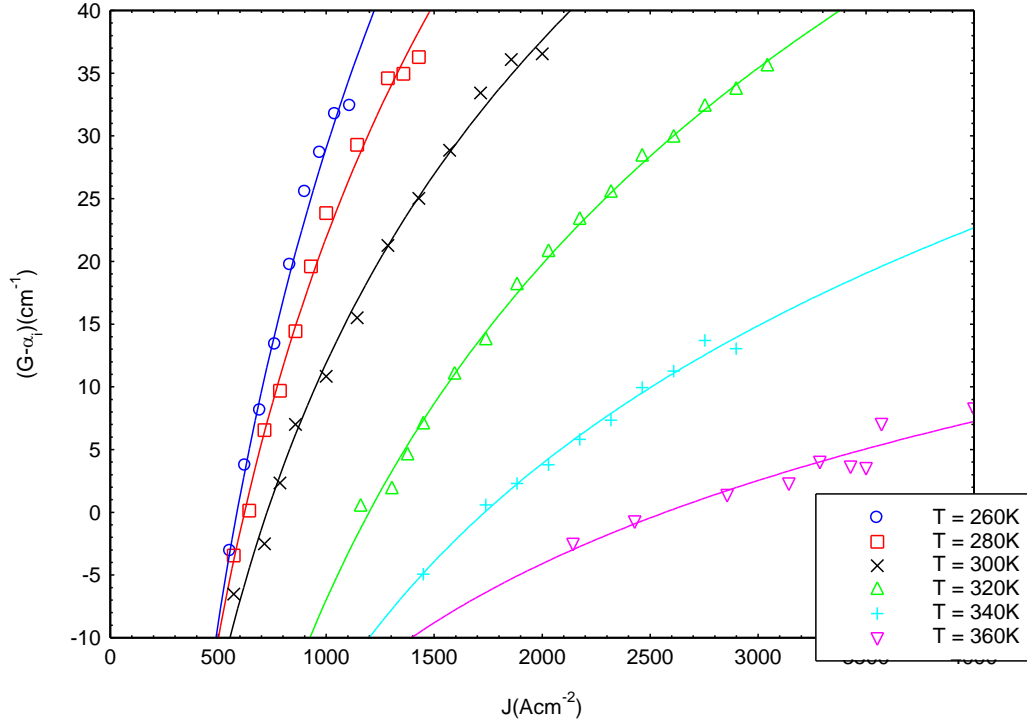
Since the quantum dot sample has a smaller number of states than the quantum well sample, the quantum dot gain spectra are observed to saturate at lower gain as compared to the quantum well ( $10 \text{ cm}^{-1}$  to  $38 \text{ cm}^{-1}$ ). Besides, the spectral shift of peak gain in quantum dot is larger compared to quantum well sample. This change in gain spectrum with increasing injection current density can affect the performance of a device. For instance, when this material is used in a laser, the lasing wavelength is strongly influenced by the length of the device. The longer the laser, the lower the gain (per unit length) or the lower the required injection current. Consequently the laser will operate at a longer wavelength than one that is about twice as short.

Figure 3.13 shows the plot of the peak gain spectra against applied current density for all measured temperatures. The current density is figured out from current per unit area which is given by:

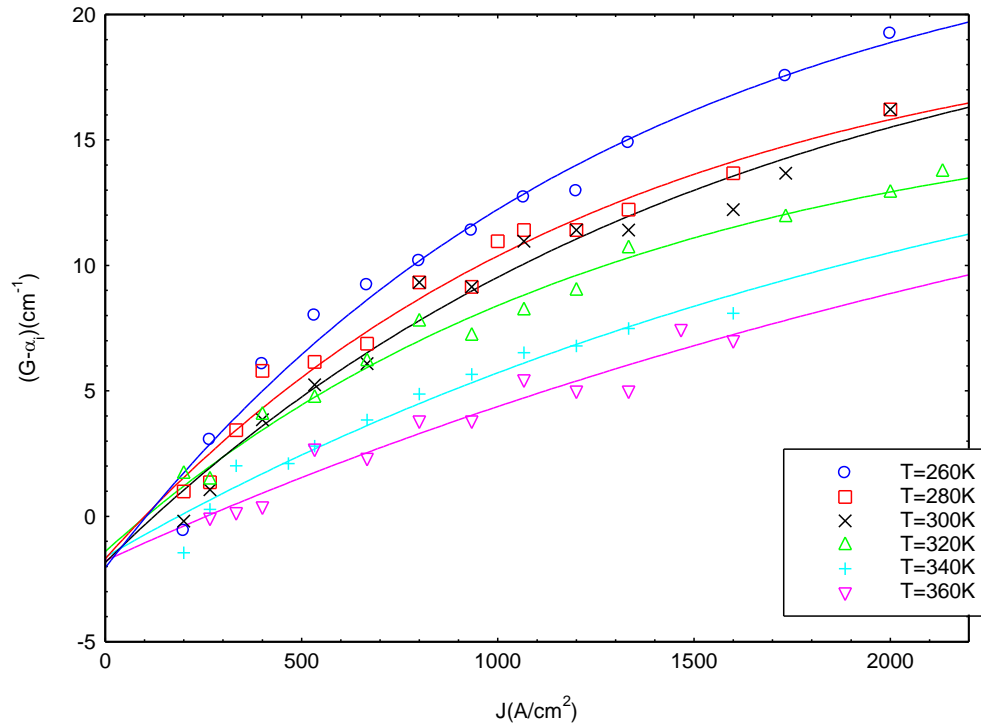
$$J = \frac{I}{A}$$

Equation 3.8

where  $I$  is the applied current and  $A$  is the product of device length and the pumped stripe width. The pumped stripe width is taken from the FWHM measurement of near field as mentioned in Section 3.1.3.4. Measurement of near field was done at all measured temperatures to ensure there is no influence of current spreading in wells and dots due to mobility and doping intensity that are temperature dependants. The results show that the amplitude of the peak gain for both samples decreased as the operating temperature increases. This is due to the carriers that are populated over more states at higher temperature causing the spectrum to broaden hence reducing the peak gain [10] [15].



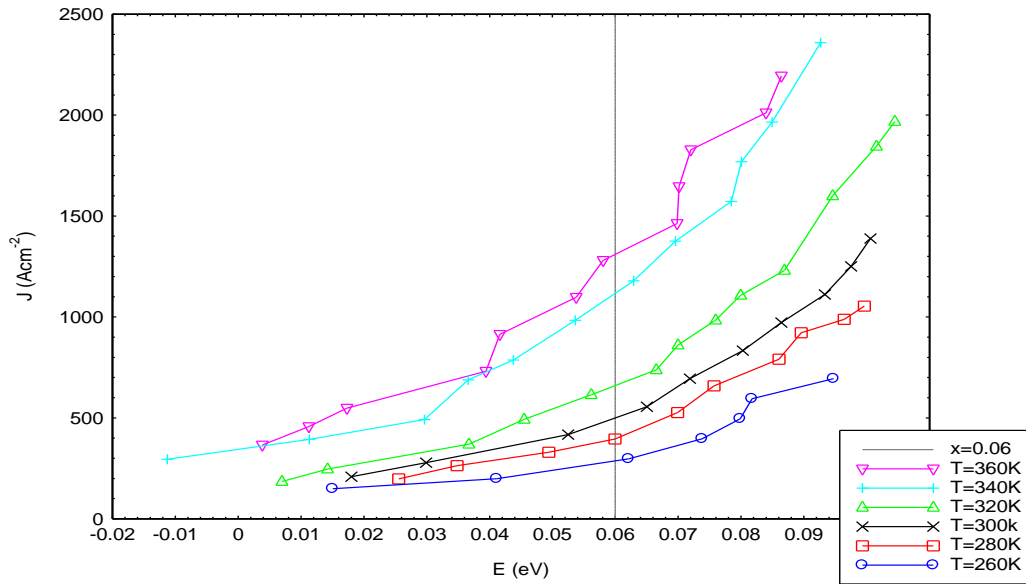
(a)



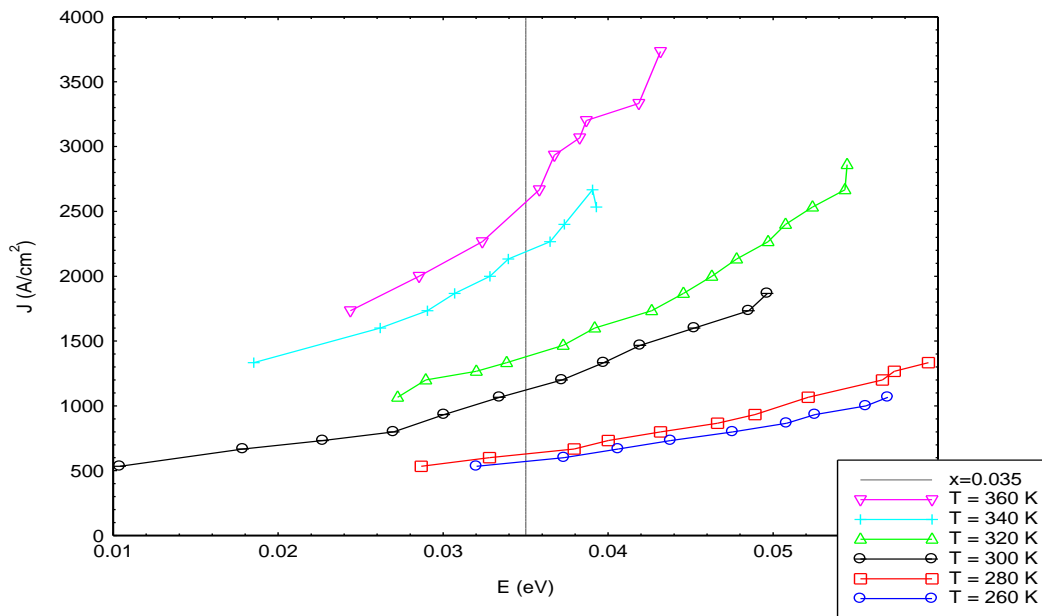
(b)

Figure 3.13 : Plot of peak gain against applied current density as a function of temperature for (a) quantum well and (b) quantum dot samples.

Figure 3.14 shows the current density applied against inversion level as a function of temperature for (a) quantum well and (b) quantum dot samples. The inversion level for both samples change with temperature. As the temperature increases, higher values of current density are needed to achieve the inversion level.



(a)



(b)

Figure 3.14 : Plot of the applied current density against inversion level as a function of temperature for (a) quantum well and (b) quantum dot sample.

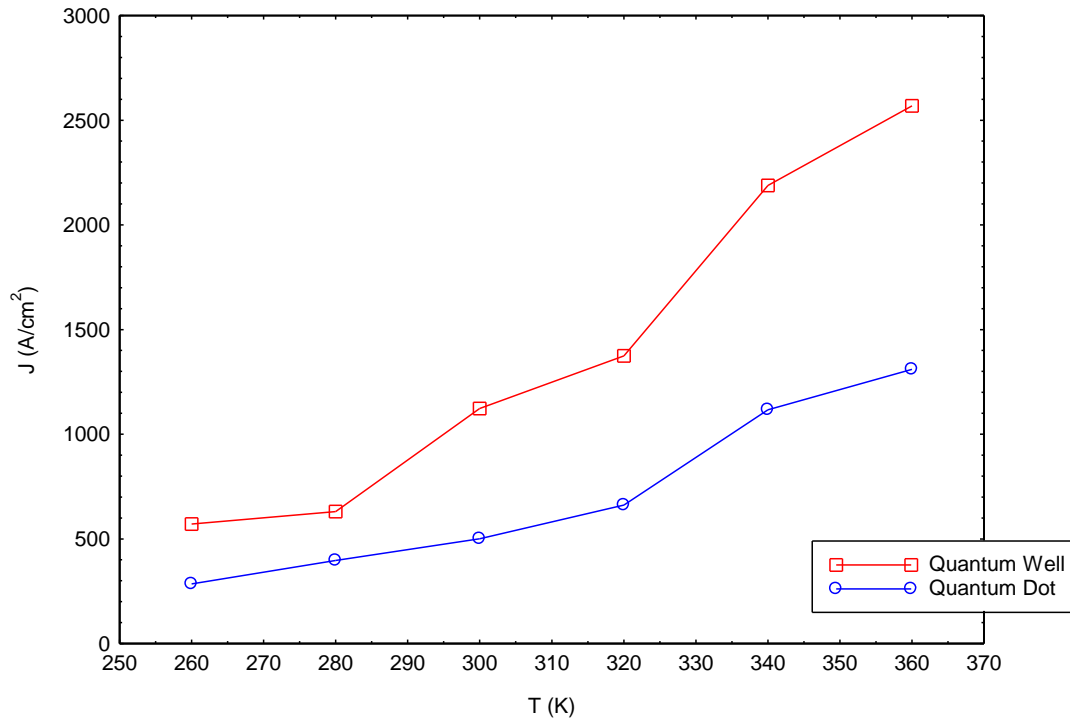


Figure 3.15 : Plot of applied current density as a function of temperature at a constant value of the inversion level of quantum well and quantum dot samples.

Figure 3.15 shows the applied current density at the constant inversion level of quantum well and quantum dot sample. The quantum well sample requires higher current density as compared to the quantum dot sample to achieve the inversion level at all temperatures because there are more states in the quantum well sample. But the maximum gain is also higher because there are more states at a given energy in the quantum well sample. This is a fundamental difference between the quantum dot and quantum well material, and is nothing to do with the non-radiative recombination, which occurs and may be due to differences in different samples grown at different times. To see which sample is best at 300 K, the quantum well and quantum dot data is plotted on the same graph as a function of current density, which does include all processes as shown in Figure 3.16.



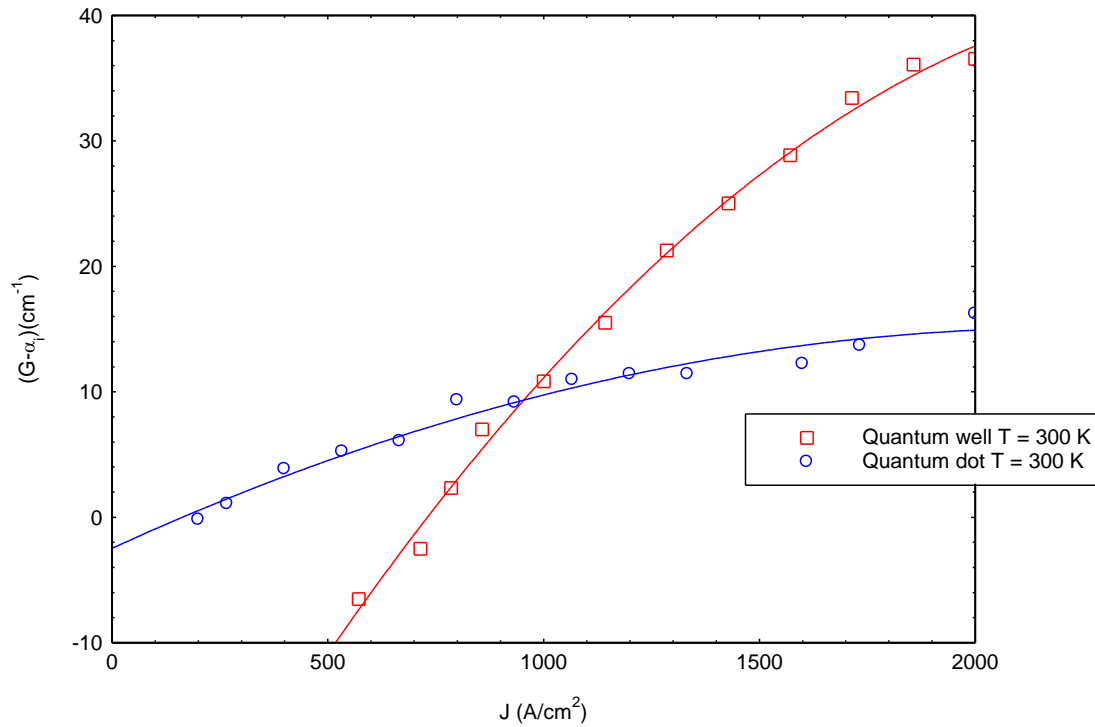


Figure 3.16 : Plot of peak gain against applied current density at  $T = 300$  K.

From the graph in Figure 3.16, the maximum gain obtainable from quantum dot material at the best operating temperature for the prototype of a coupled cavity living laser is lower ( $15 \text{ cm}^{-1}$  of  $37 \text{ cm}^{-1}$ ). Since the etched facet mirror may occur a large loss and because I have access to a more quantum well material, I will use the quantum well material.

### 3.4 Conclusion

The multisection measurement technique was used for characterization of quantum well and quantum dot gain media. The ASE spectra produced by this measurement were then computed to produce absorption and gain spectra for further analysis. The measurement was done in the temperature range from 260 K to 360 K.

The absorption edge energy for both samples show rigid shift to higher energy as the operating temperature increased. This is due to the shift in energy of the constituent

bandgap. The internal optical loss,  $\alpha_i$  for both samples remain the same with temperature change within the experimental uncertainty. The quantum well sample has higher  $\alpha_i$  value which is  $12 \pm 3 \text{ cm}^{-1}$  compared to the quantum dot sample which is  $2 \pm 1 \text{ cm}^{-1}$ .

From the gain spectra of both samples, quantum dot sample show broader gain spectra with reduced peak gain magnitudes as compared to the quantum well sample that have narrow gain spectra with higher peak gain. This is due to free carrier effect and band filling of inhomogeneously broaden state in the active medium.

Lower  $\alpha_i$  and broader gain spectra gives advantage to quantum dot sample to be used as the active medium as it allows fabrication of the prototype of a coupled cavity living laser with a longer cavity whilst the device still operating at the saturated part of the gain. The saturated part of the gain is where the coupled cavity sensing effect, when both cavities are operated as lasers, is at its greatest because changes in loss in the gap would produce larger changes in the output.

The peak gain for both samples is observed to have a spectral shift to a lower wavelength as the current density increase. The spectral peak gain shift of quantum dot is larger than of quantum well. This larger wavelength shift implies much greater scope for wavelength tuning of the coupled cavity device [16].

The maximum gain can be achieved by quantum dot sample at 300 K is only  $15 \text{ cm}^{-1}$  as compared to quantum well with a maximum peak gain of  $37 \text{ cm}^{-1}$ . For the device with  $\alpha_i$  of  $10 \text{ cm}^{-1}$  and lower, quantum dot is better to be used in the fabrication of coupled cavity living laser due to the factors mentioned above. However, for the device with higher loss, quantum well active medium would be a better option since it can provide much higher gain with a small increase in current density. Because of that and since I have access to a more quantum well material, I will use quantum well active medium for the fabrication of a prototype in this work.

### 3.5 Bibliography

- [1] P. S. Z. Jr, Quantum Well Lasers, Boston San Diego New York London Sydney Tokyo Toronto: Academic Press, Inc., 1993.
- [2] V. M. Ustinov, A. E. Zhukov, A. Y. Egorov and A. N. Maleev, Quantum Dot Lasers, New York: Oxford University Press, 2003.
- [3] P. Blood, G. M. Lewis, P. M. Smowton, H. Summers, J. Thomson and J. Lutti, "Characterization of Semiconductor Laser Gain Media by the Segmented Contact Method," *IEEE Journal of Selected Topics in Quantum Electronics*, vol. 9, no. 5, pp. 1275-1282, 2003.
- [4] L. A. Coldren, S. W. Corzine and M. L. Mashanovotch, Diode Laser and Photonic Integrated Circuit, New Jersey: Wiley, 2012.
- [5] Y. Sakaguchi, L. C. Stephens, M. Makino, T. Kaneko, F. R. Strebel, L. L. Danhauser, G. N. Jenkins and J. M. C. Bull, "Apoptosis in Tumors and Normal Tissues Induced by Whole Body Hyperthermia in Rats," *Cancer Research*, no. 55, pp. 4559 - 5464, 1995.
- [6] N. L. Gershfeld and M. Murayama, "Thermal Instability of Red Blood Cell Membrane Bilayers : Temperature Dependence of Hemolysis," *The Journal of Membrane Biology*, vol. 101, pp. 67 - 72, 1988.
- [7] J. A. C. R. C. D. V. D. H. G. Pieter F. van der Meer, "Evaluation of overnight hold of whole blood at room temperature," *Transfusion*, vol. 51, pp. 15S - 24S, 2011.
- [8] J. E. Lovelock, "The Haemolysis of HUMAN Blood Cells by Freezing and Thawing," *Biochimica Et Biohysica Acta*, vol. 10, pp. 414 - 426, 1953.
- [9] J. Lutti, P. M. Smowton, G. M. Lewis and P. Blood, "Gain saturation in InP/GaInP quantum dot lasers," *Applied Physics letter*, vol. 86, 2005.

- [10] P. M. Smowton, S. N. Elliot , S. Shutts, M. S. Al Gahmdi and A. B. Krysa, "Temperature - Dependent threshold current in InP quantum dot lasers," *IEEE Journal of Selected Topics in Quantum Electronics*, vol. 17, no. 5, pp. 1343 - 1348, 2011.
- [11] P. Smowton and P. Blood, "Quantum Dot Lasers : Theory and Experiment," in *VLSI Micro- and Nanophotonics: Science, Technology, and Applications*, CRC Press, 2011, pp. 9-1 - 9-35.
- [12] A. Sobiesierski and P. Smowton, "Quantum Dot Laer : Physics and Applications," in *Comprehensive Semiconductor Science and Technology : Materials, Preparations and Properties*, Elsevier, 2011, pp. 354 - 384.
- [13] S. Shutts, P. M. Smowton and A. B. Krysa, "InP quantum dot lasers with temperature insensitive operating wavelength," *Applied Physics Letter*, vol. 103, 2013.
- [14] D. V. Karasyov and V. K. Kononenko, "Broadening of Gain Spectra of Quantum Well Lasers," *Journal of Applied Spectroscopy*, vol. 61, no. 5-6, pp. 739 - 743, 1994.
- [15] M. Kasim, S. N. Elliot, A. B. Krysa and P. M. Smowton, "Reducing Thermal Carrier Spreading in InP Quantum Dot Lasers," *IEEE Journal of Selected Topics in Quantum Electronics*, vol. 21, no. 6, 2015.
- [16] R. Thomas, Monolithic Coupled Cavity Laser Diodes For Bio Sensing Applications, PhD Thesis, Cardiff University, 2012.
- [17] M. Abderrezek, M. Fathi, S. Mekhilef and F. Djahli, "Effect of Temperature on the GaInP/GaAs Tandem Solar Cell Performances," *International Journal of Renewable Energy Research*, vol. 5, no. 2, pp. 629-634, 2015.
- [18] "AZO Material," AZO Material, 16 August 2013. [Online]. Available: <http://www.azom.com/article.aspx?ArticleID=8510>. [Accessed 29 December 2015].

## Chapter 4 : Etched Facet

### 4.1 Introduction

The optical resonator plays an important role in the generation of the laser output. It consists of two mirrors, or in the example of semiconductor laser, facets, which offer an optical feedback for producing gains in the active medium. Fabrication of high quality facets is crucial as facet reflectivity affects mirror loss, hence affecting laser gain as explained in Section 2.2.24.

The preferred method for facet formation in most semiconductor systems is cleaving the substrates and epilayers on a mutual cleavage plane because it is a robust method for forming atomically smooth, vertical facets. However, the cleaving process is a mechanical process that causes the wafer to be broken into bars and is incompatible with monolithic integration. Due to difficulties of forming cleaved inner facets in the monolithic coupled cavity design, an etching technique has been applied as an alternative. In this work, the facets have been etched using an inductively coupled plasma (ICP) reactive ion etching (RIE) process. The aim is to produce laser facets that are vertical, nearly atomically flat and etched through the vertical extent of the epitaxial growth layer on the semiconductor crystal into the GaAs substrate that is comparable with the cleaved facet.

Fabrication of etched facet involves selection of material to be used as a mask for plasma etch as well as an electron beam lithography (EBL) process for patterning of the mask. In this chapter, I explain the working principle of EBL and ICP as well as fabrication process of the etched facet and all the issues involved. Performance of etched facet laser is compared with cleaved facet laser by measuring their current density threshold,  $J_{th}$ . Facet reflectivity is then derived from the value of current density threshold. All the devices that were used in the study uses UWIC 412 1608c single quantum well material unless stated otherwise.

## 4.2 Electron Beam Lithography

Due to the complex nature of the fabrication process, a series of highly advanced equipment had to be used in order to be able to complete the different process steps of the fabrication process. Fabrication of the prototype of couple cavity living laser in this study involves the use of electron beam lithography and inductively coupled plasma etching systems. The detail processing procedure of the devices will be explained in Section 4.4. The following sections focus only on electron beam lithography and ICP etching system and some of the principles behind them.

Electron beam lithography (EBL) is a technique for creating extremely fine pattern down to submicron patterns, 0.1  $\mu\text{m}$  and below. Such patterns can be made because of the spots of electrons are very small, whereas the optical lithography is limited by the wavelength of light which is used for exposure. The wavelength of the electron is so small that diffraction no longer determines the lithographic resolution. The main attributes of EBL technology are (i) it is capable of very high resolution, almost to the atomic level; (ii) it is a flexible technique that can work with a variety of materials and an almost infinite number of patterns; (iii) it is slow, being one or more orders of magnitude slower than optical lithography; and (iv) it is expensive and complicated [1]. Despite its flexibility and ability to produce high resolution patterns, it is hard to precisely control the final EBL pattern dimension due to many factors such as beam size, focus, exposure dose, developer chemicals, development time, development temperature and a few others. Table 4.1 shows some of the parameters affecting the EBL process and the final product.

Table 4.1 : Parameter affecting EBL process. Ref [3].

<b>Parameter</b>	<b>Process impact</b>
Exposure energy	Resolution, sensitivity, proximity
Exposure dose	Pattern quality
Pattern density	Proximity, quality of the pattern
Resist material	Sensitivity, resolution, contrast
Resist thickness	Sensitivity, resolution, quality of the pattern
Developer	Sensitivity, resolution
Development temperature	Sensitivity, resolution
Development time	Sensitivity, resolution

The prototype and devices in this work were fabricated in the clean room in Cardiff University. The electron beam lithography system available is a Raith e-line lithography system.

The Raith e-line is a low-energy (10-30 kV acceleration voltage) electron beam lithography (EBL) machine. The advantage of low energy is that a smaller focus (higher resolution) can be achieved with the electron optics. The disadvantage is that the write time is longer.

Firstly, the design of the mask pattern is created using Klayout software. This freeware is able to save the design in the form of GDSII file that later can be transferred to eline machine. Figure 4.1 shows the screen shot of the design page of Klayout software that were used.

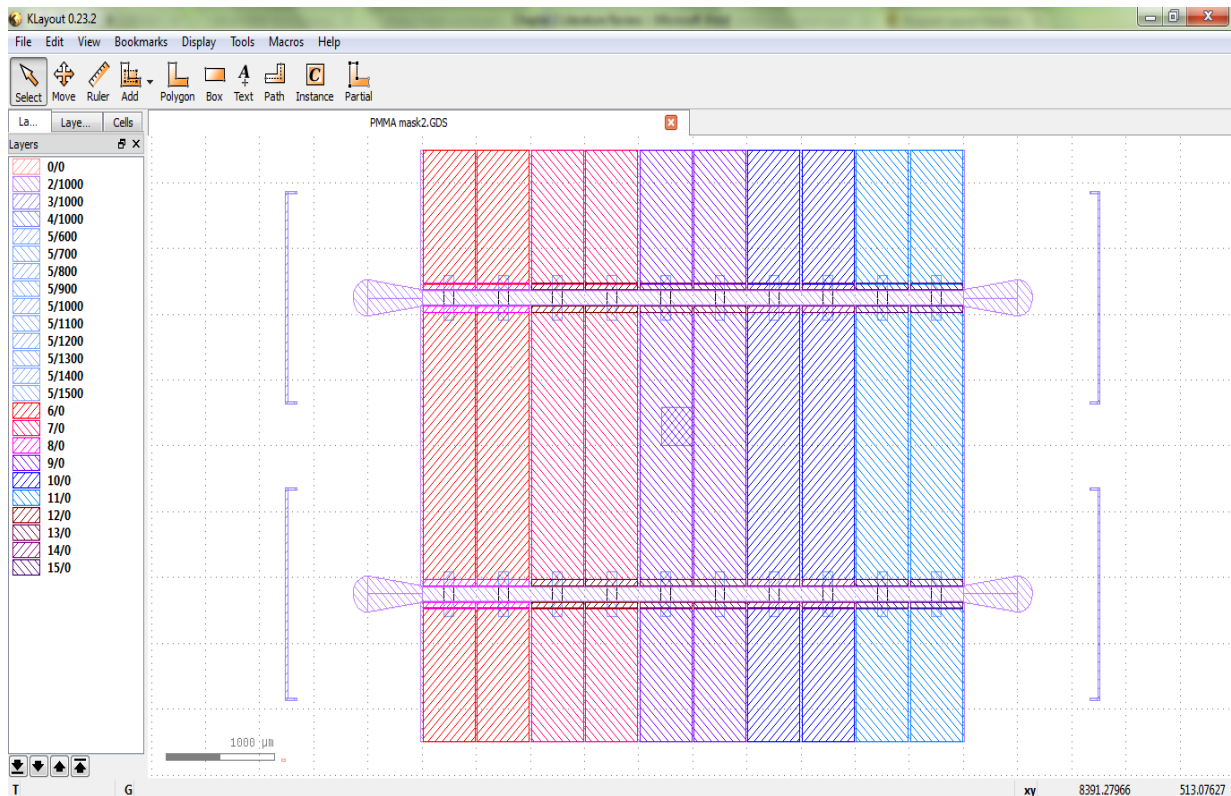


Figure 4.1 : Screen shot of the design page of Klayout software.

An electron beam lithography (EBL) system closely resembles a scanning electron microscope (SEM) system. The primary difference between EBL and SEM systems is that in an EBL the beam is scanned onto the sample according to the instructions given by the pattern generator, while in SEM the beam is raster scanned over the sample in order to collect secondary electron to work an image [2].

The prepared sample (coated with PMMA and baked) is placed onto the sample holder as seen in Figure 4.2. The sample holder contains a Faraday-cup-holder which is used to measure the beam – current. This is crucial in order to calculate the correct parameters for the EBL to expose a sample with a certain dose. In this work, the measured beam current value is 0.16 nA.



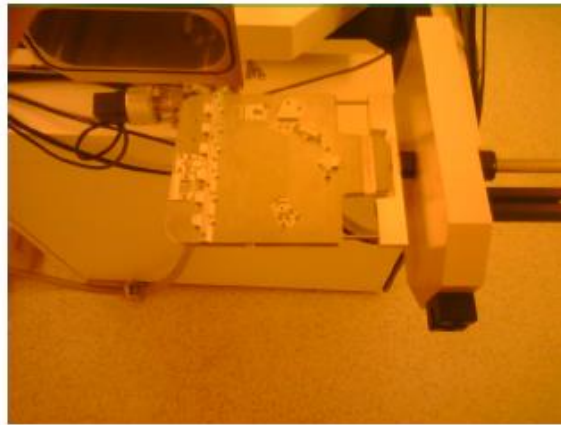


Figure 4.2 : Image of sample holder used in e-line Raith system.

The sample is then loaded into the loadlock chamber. The loadlock chamber will raise the pressure to the vacuum pressure before transfer the sample holder into and out from the sample chamber.

The sample chamber is where the exposure of the sample takes place. To direct an electron beam, an acceleration voltage is applied between a cathode and an electrode. The magnitude of the acceleration voltage that is used in this work is 10 kV.



Figure 4.3 : Image of e-line Raith Electron beam lithography system available in the clean room of Cardiff University.

In the sample holder, the beam stays fixed in one position, while the stage is moved. The beam aperture has a diameter of 20  $\mu\text{m}$ . In order to expose a large area when only moving

the stage in one direction, the beam can move in a fixed pattern. The electron beam gun moves in a circular pattern, indicated by red circles. Simultaneously, the stage is moving in the direction as indicated in Figure 4.4 in a fixed step size or spacing. In this work, the step size is  $0.02\text{ }\mu\text{m}$  in U as well as V directions. The resulting line is indicated by the darker shades at the edge of the electron beam path. The interaction between electron and resist during exposure will be discussed in detail later in Chapter 4. Table 4.2 summarize all the parameters used in the fabrication work of the prototype of the coupled cavity living laser and other testing device. The electron beam lithography process in this work is done with supervision of Dr. Phil Buckle or Dr. Rob Thomas.

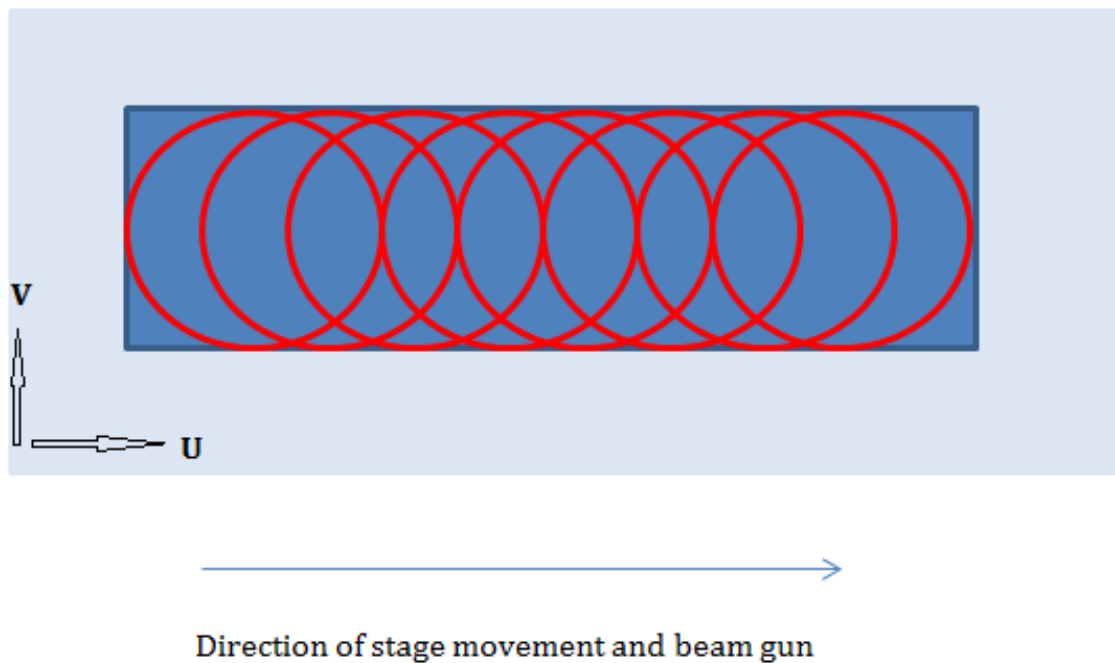


Figure 4.4 : Illustration of the electron beam gun and stage movement during exposure.

Table 4.2 : Summary of parameters used in fabrication of a prototype of a coupled cavity living laser.

Parameter	Value used in fabrication process
Working distance	10 mm
Acceleration voltage	10 kV
Beam aperture	20 $\mu\text{m}$
Beam current	0.16 nA
Exposure step size U	0.02 $\mu\text{m}$
Exposure step size V	0.02 $\mu\text{m}$
Nominal exposure dose	165 $\mu\text{C}/\text{cm}^2$

### 4.3 Inductively Coupled Plasma Etching

Fabrication of the etched facets of this work is realized by an inductively coupled plasma (ICP) etching technique due to difficulties of forming cleaved inner facets in the monolithic coupled cavity design. The ICP etching system available in the Cardiff University clean room is Plasmalab System 100 from Oxford Instruments as shown in Figure 4.5.



Figure 4.5 : Plasmalab System 100 by Oxford Instruments available in the clean room of Cardiff University.

A schematic diagram of the gas chamber is shown in Figure 4.6. In this system, the radio frequency (RF) power is applied to the induction coil. The RF current flows in the coil generate changing electric field via inductive coupling. A high density plasma is produced by the ICP power which is coupled inductively to a low pressure gas mixture. The energy of the ions hitting the sample is monitored by measurement of the direct current (DC) bias generated on the lower electrode. This energy is controlled by the reactive ion etching (RIE) or forward RF power applied to the lower electrode. The independent control of plasma density and ion energy allows high etch rates to be achieved with reduced ion bombardment to minimize surface damage by high energy ions.

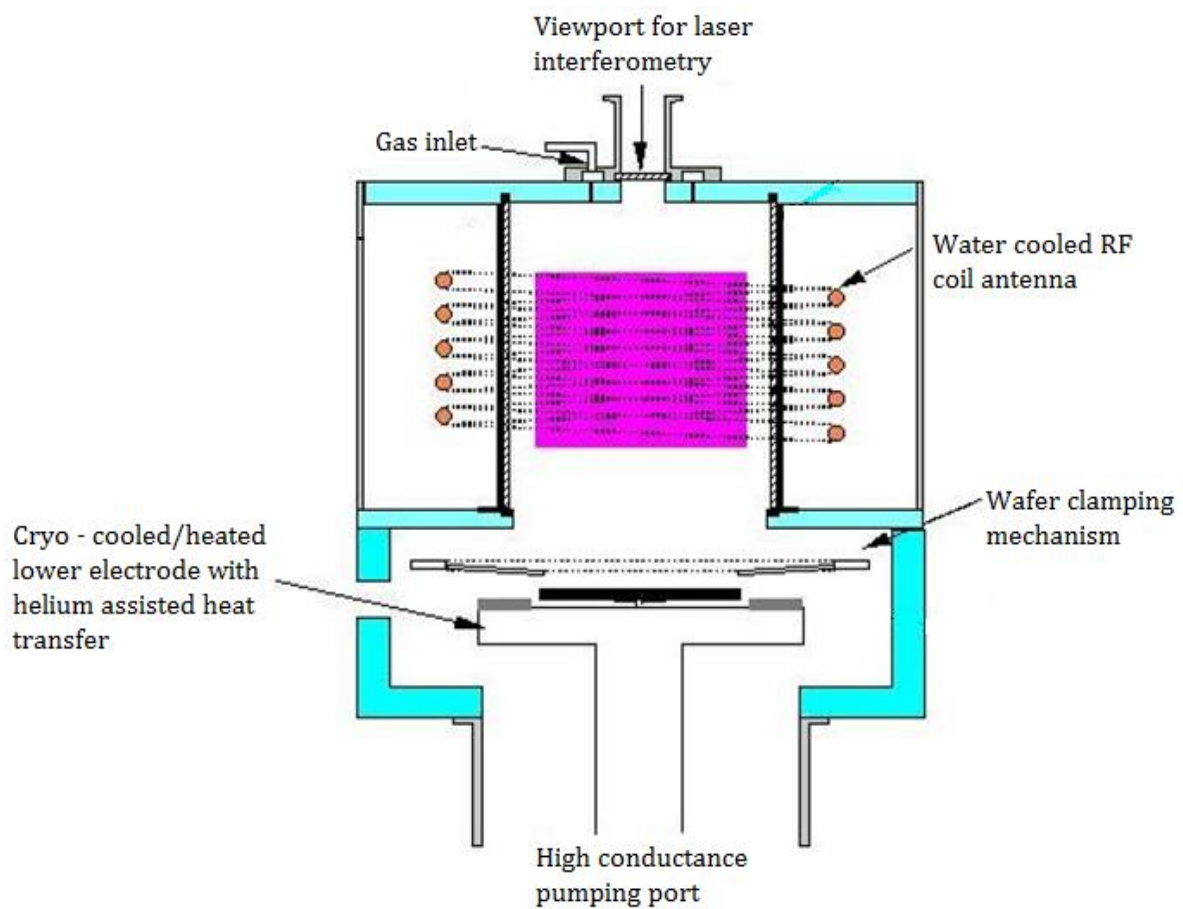


Figure 4.6 : Schematic diagram of gas chamber for Plasmalab System 100 [3].

The sample that is placed on the carrier wafer is loaded into the chamber via a loadlock to maintain good stability of chamber vacuum. Helium pressure is applied to the back of the carrier wafer to provide good thermal conductance between the chuck and the wafer. The  $\text{Cl}_2/\text{Ar}$  dry etch recipe is used in this work to etch the semiconductor at high temperature, i.e. 180 °C. Table 4.3 summarizes all the parameters used in the etching

process of inner facet if the prototype of a coupled cavity living laser in this work. The inductively coupled plasma etching of semiconductor crystal in this work is done with supervision of Dr. Rob Thomas or Dr. Angela Sobiesierski.

Table 4.3 : Summary of parameters used in fabrication of etched facet for the prototype of a coupled cavity living laser.

Parameter	Value used in fabrication process
Gas Cl <sub>2</sub>	4 sccms
Gas Ar	36 sccms
Helium pressure	10 mtorr
Chamber pressure	10 mtorr
RIE power	200 W
ICP power	500 W
Table temperature	180°C

## 4.4 Fabrication Of Etched Facet

### 4.4.1 Selection Of Material For The Mask

Silicon dioxide (SiO<sub>2</sub>) and nickel were both tested for use as plasma etch masks. Procedures for mask preparation and patterning are a bit different for each material and described below. The results for the facets fabricated with both masks are shown in Section 4.4.1.4.

#### 4.4.1.1 Sample Preparation

A rectangular 6 x 9 mm sample is cleaved from an AlGaInP semiconductor wafer. The longest dimension is cleaved along the (001) crystallographic plane in order to provide a reference edge for the alignment of the etched facet and the laser contact stripe patterns. The sample is then cleaned using acetone in an ultrasonic bath for 10 minutes, followed

by trichloroethylene, acetone, methanol and isopropyl cleaning on a hot plate at 80 °C for 5 minutes for each of the solvents to remove any contaminations on the surface of the wafer. The sample is then blown dried using a nitrogen gun.

#### **4.4.1.2 The Etch Mask Preparation And Patterning**

For the sample with SiO<sub>2</sub> mask, a 280 nm thick SiO<sub>2</sub> layer is deposited on to the upper surface of the sample using an Edwards electron beam evaporator. The sample is then baked in the rapid thermal anneal (RTA) machine for 30 minutes at 400 °C in an inert nitrogen atmosphere to remove all the moisture trapped in the SiO<sub>2</sub> layer. For non-conductive material, substrate charging can deflect the electron beam during patterning causing severe problems in pattern placement accuracy. Therefore, a 20 nm nickel layer is then deposited using the same system on top of the SiO<sub>2</sub> layer. The nickel functions as a charge dissipation layer [4] [5] providing stable, conductive, grounding layer to circumvent electron beam deflection due to sample charging. This will minimize pattern displacement and subfield stitching error [6].

A 250 nm type A4 polymethyl-methacrylate (PMMA) positive resist is spin-coated on top of the nickel layer by spinning it on the sample for 45 seconds at the speed of 5000 rpm. The subsequent bake step at 180 °C for 3 minutes is performed in order to dry the resist films, which would otherwise stick to the mask. Furthermore, the resist layer is hardened during this step, making it more resistant.

For the sample with a nickel mask, the wafer is coated straight away with A4 PMMA positive resist after the cleaning process. The recipe for resist coating is the same as described previously.

The mask pattern for the etch is then transferred to the resist by direct write exposure using an Eline electron beam lithography machine system. Exposure to the electron beam breaks the long polymer chains of resist into smaller fragment, which when developed in a methyl isobutyl ketone:isopropyl (MIBK:IPA) solution, becomes more easily dissolved than the unexposed regions. The sample is then rinsed with IPA for 30 seconds. The high

resolution and sharp contrast that can be achieved with this system leaves a pattern with a relatively sharp edge and near vertical step profile in the resist. This profile is very important as any deviation from vertical will ultimately be transferred into the semiconductor etch, affecting the efficiency of the resulting facet.

For the sample with the SiO<sub>2</sub> mask, the pattern on the PMMA layer is now serving as a mask for a nickel etching process to remove all the nickel from the top of SiO<sub>2</sub> layer that will be the mask for semiconductor etches later on. Nickel is etched until a sign of undercutting is observed under the microscope to make sure that there is no influence of nickel that will involve in the formation of facet.

Meanwhile, for the sample with the nickel mask, the wafer with a developed pattern of PMMA layer undergoes 10 seconds oxygen etch, that is done under supervision of Dr. Angela Sobiesierski or Dr. Rob Thomas, with 50 W of RIE power at room temperature to remove any remaining resist at the bottom of the developed pattern. A 60 nm layer of nickel is then deposited onto the surface using the Edwards electron beam evaporator. The nickel mask is made by lifting off the resist in acetone leaving the metal pattern in contact with the wafer.

An air plasma etch has also been tested for stripping resist at the bottom of the pattern before nickel evaporation. Nevertheless, it is found that air plasma etch left residues on the sample. This is due to contamination in the chamber redeposited back on the surface of the sample. When nickel is evaporated at a later stage bubbles are created on or by the redeposited residues as shown in Figure 4.7. Therefore, air plasma is not used in the process. The air plasma etch has been performed by Mr. Chris Dunscombe.

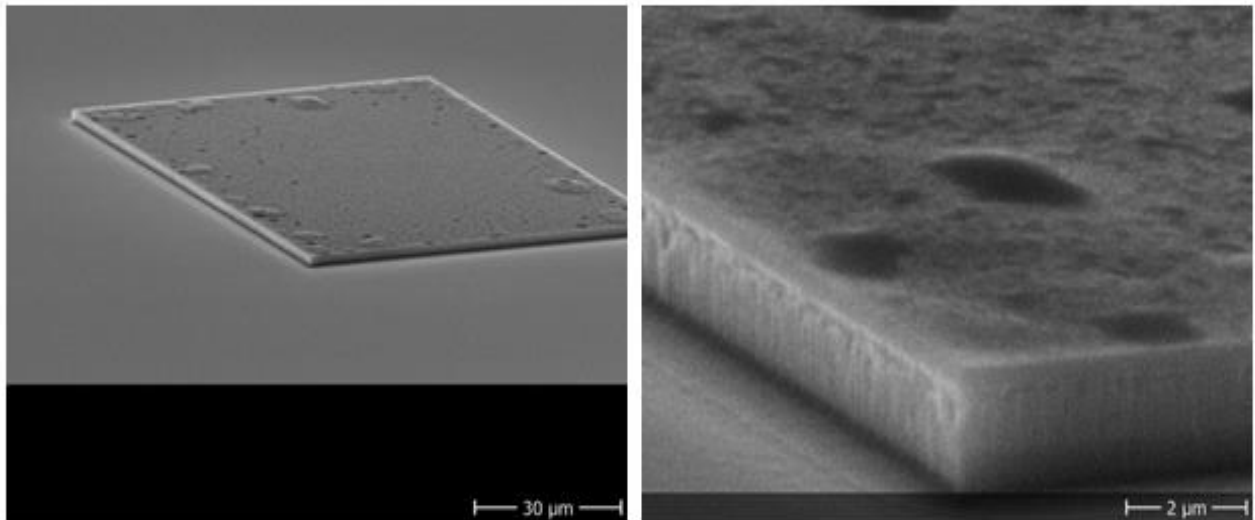


Figure 4.7 : Sample with a nickel mask that undergone air plasma etch to stripping resist before evaporation of metal.

#### 4.4.1.3 Inductively Coupled Plasma (ICP) Reactive Ion Etching (RIE) Process

For the sample with  $\text{SiO}_2$  mask, the pattern of PMMA layer is transferred onto the  $\text{SiO}_2$  etch mask at room temperature by the  $\text{C}_4\text{F}_8/\text{Ar}$  ICP RIE process. The remaining PMMA is then removed using acetone and the surface is de-contaminated with followed oxygen plasma etch.

The  $\text{SiO}_2$  mask is then used to transfer the pattern into the semiconductor crystal using a high temperature ( $200\text{ }^\circ\text{C}$ )  $\text{Ar}/\text{Cl}_2$  ICP etch. The same temperature and gas composition is used to etch the semiconductor with nickel mask. Figure 4.8 shows the diagram of the process flow of fabrication of the etched facet using  $\text{SiO}_2$  and nickel mask.



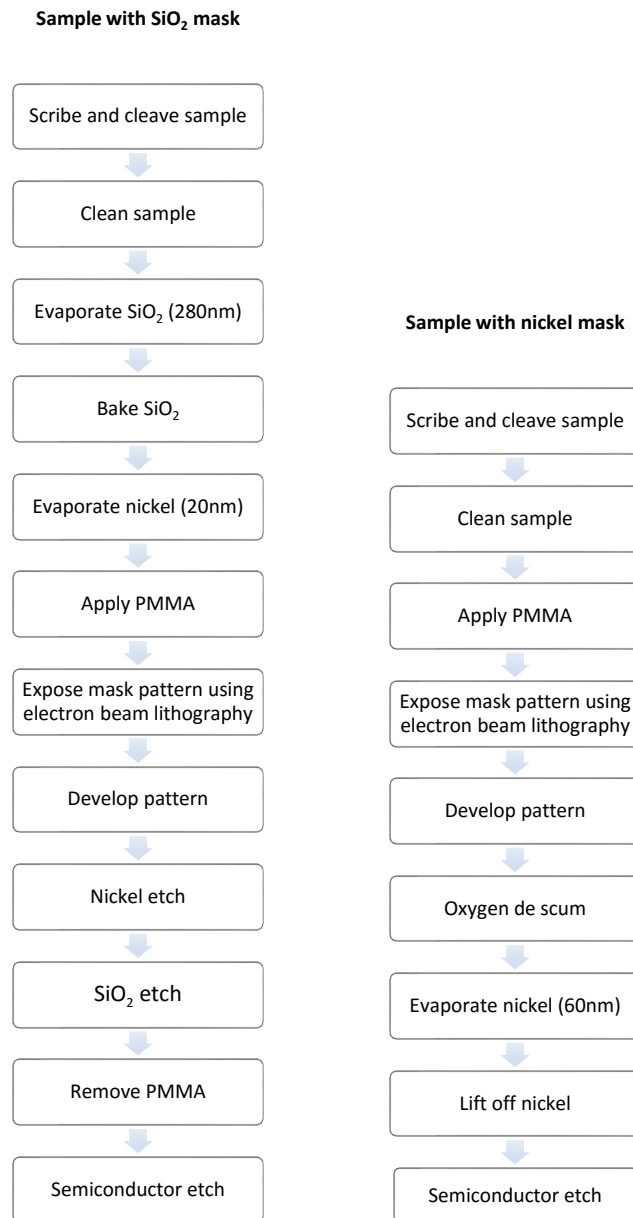


Figure 4.8 : Processing procedure of fabrication of etched facet using SiO<sub>2</sub> and nickel mask.

#### 4.4.1.4 Fabricated Etched Facet

Figure 4.9 shows the representative scanning electron microscope (SEM) images of facet formed by a dry etching technique using SiO<sub>2</sub> as a mask.

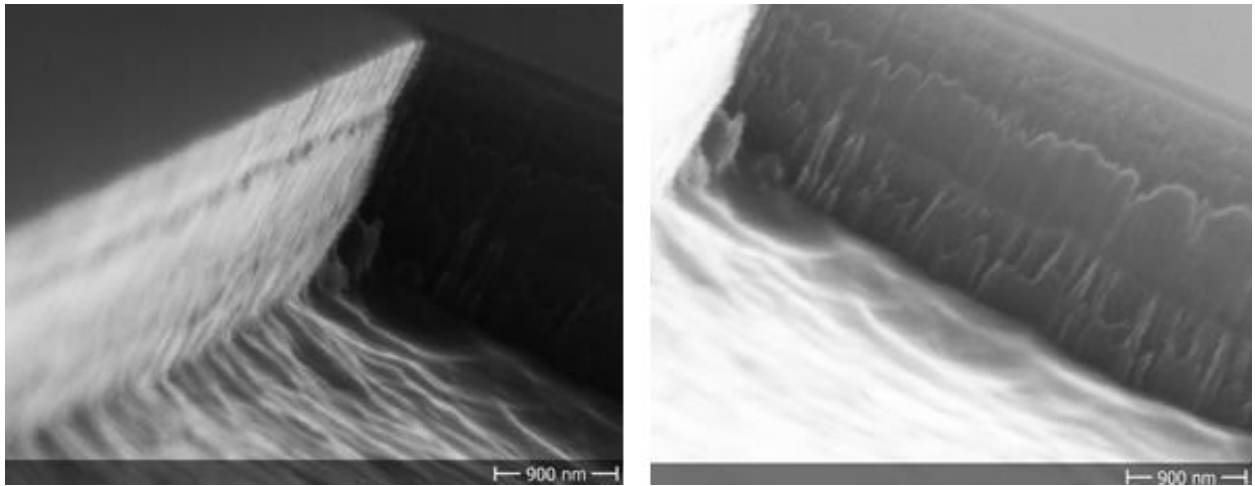


Figure 4.9 : SEM images of facets formed by a dry etching technique using  $\text{SiO}_2$  as a mask.

The facet for a sample that is fabricated with  $\text{SiO}_2$  mask was observed to have a terracing effect with a striated pattern. An experiment has been done to investigate the cause of the terracing effect. Therefore, exactly the same processing procedure has been done using a bare GaAs wafer sample. It is observed that the etched facet fabricated with a bare GaAs wafer sample, using  $\text{SiO}_2$  as a mask for dry etching, shows striated pattern as appeared in the etched facet fabricated with a single quantum well wafer sample but without the terracing effect as shown in Figure 4.10.

Reactive ion etching process uses an inert gas argon, Ar in an ion source to generate an ion beam, which directed towards the sample. This is done in conjunction with a flow of a reactive gas chlorine,  $\text{Cl}_2$  near the sample. The ion beam provides the physical component of the etching process, while the reactive gas provides the chemical component. The etching is anisotropic as the etching only takes place in the direction of the ion beam. There is independent direct control over both the physical and chemical component of etch. This independent control allows the possibility of selective etch between etched mask and the material that is etched.

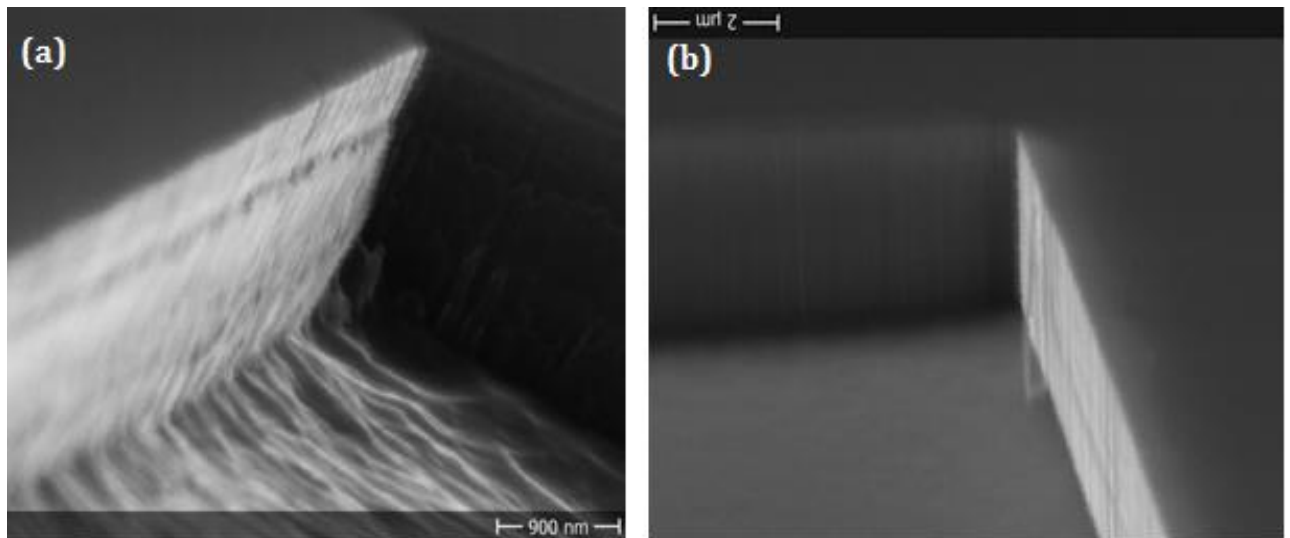


Figure 4.10 : Facet formed using SiO<sub>2</sub> mask on (a) single quantum well wafer sample and (b) bare GaAs wafer sample.

Selective etching occurs during the etching process of semiconductor crystal in the high temperature RIE process. The semiconductor crystal is etched rapidly while the SiO<sub>2</sub> mask is etched very slowly in Ar/Cl<sub>2</sub> plasma environment. Hence, a thick layer of SiO<sub>2</sub> (about 280 nm) is deposited as a mask. At the end of the etching process, about 160 nm (as being measured using Dektak system) of SiO<sub>2</sub> is left on the sample that later on can be used as the insulating layer for the laser. However, the energetic plasma is reacting with the SiO<sub>2</sub> and producing a volatile etch product [7]. Combination of different etch rate of material in the structure with reactive sputtering of SiO<sub>2</sub> with the etchant causes the terracing effect. Figure 4.10 shows that there are four terraces and they correspond to the four different materials in the structure which are GaAs cap, AlInP upper cladding, AlGaInP active material and AlInP lower cladding.

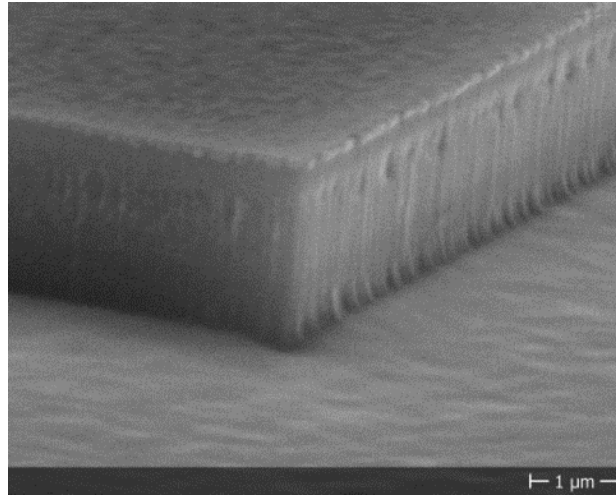


Figure 4.11 : SEM image of facets formed by a dry etching technique using nickel as a mask.

A nickel mask is used to overcome the terracing effect as nickel will not interact with plasma etchant during the semiconductor crystal etch. Figure 4.11 shows the resulting facet fabricated using nickel mask. It was observed to be heavily striated along the growth direction without any terracing. These striated patterns correspond to the fabricated mask during electron beam lithography process. However, it is believed that a good laser can still be made with a striated facet as reported by [8] [9] [10]. In terms of verticality of the pattern, both fabricated facets shows high vertically as seen in Figure 4.12.

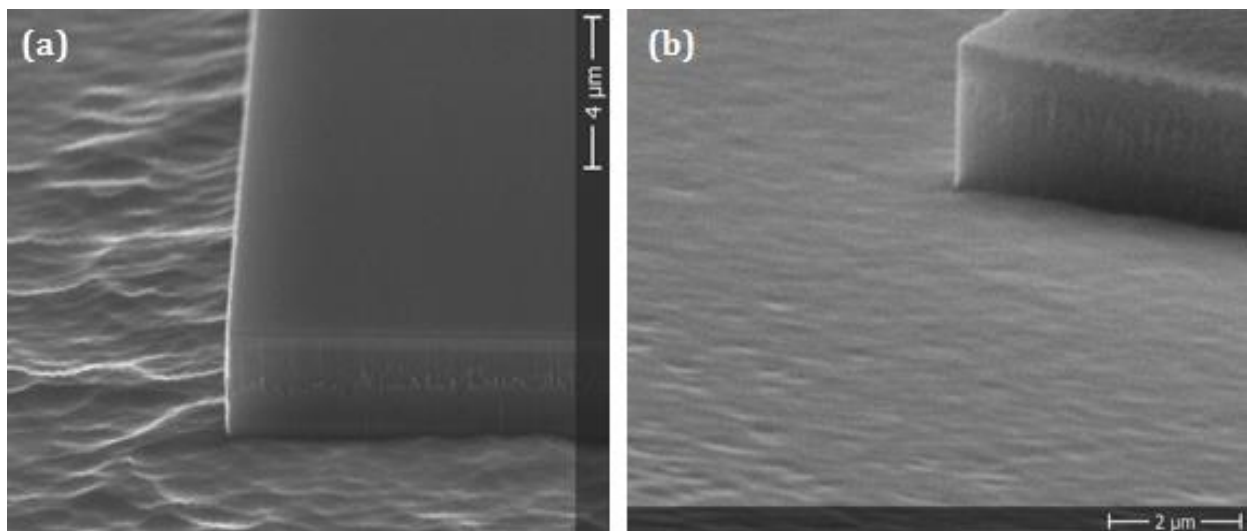


Figure 4.12 : High verticality pattern was observed on both facets fabricated using (a) SiO<sub>2</sub> and (b) nickel mask.

From the results discussed earlier, there are two mechanisms which lead to facet roughness. The first is residual roughness caused by the etching process as observed in the sample with SiO<sub>2</sub> mask. The second source of facet roughness is the mask used in the electron beam lithography process which defines the facets as observed in all samples.

As a conclusion, both types of mask, i.e. SiO<sub>2</sub> and nickel are capable of producing a high verticality facet with fine striated pattern on the etched facet. However, there is no terracing effect observed in the sample fabricated using nickel mask. This is because there is no reaction between metal mask and etchant during plasma etching of semiconductor crystal.

#### **4.4.2 Selection Of Exposure Dose And Development Time For Mask Patterning**

A sample has been prepared to investigate the impact of exposure dose and development time to the mask pattern of the etched facet. Correct selection of exposure and development conditions can ensure the necessary higher resolution and desired resist profiles and dimensions of the mask pattern that will consequently affect the fabricated etched facet. Before processing the samples, a standard cleaning process as explained in Section 4.4.1.1 was employed. A layer of A4 PMMA films were spin-coated onto the sample at a speed of 5000 rpm for 45 seconds and post-application baked at 180 °C for 3 minutes. Two series of facet mask patterns are written with different exposure dose factors (0.7 to 1.5) during the EBL process. The electron beam diameter is 20 µm with acceleration voltage 10kV, beam current 0.16 A and area dose 165 µC/cm<sup>2</sup>. The exposed sample is then cleaved into two. One of the exposed samples is developed in development solvent of MIBK:IPA at the ratio of 1:3 at room temperature for 40 seconds and the other sample at 60 seconds. Then the samples were dipped into IPA for 30 seconds and blow drying with nitrogen. Both developed samples being processed until etched facet is fabricated by using nickel as a mask for ICP RIE process.

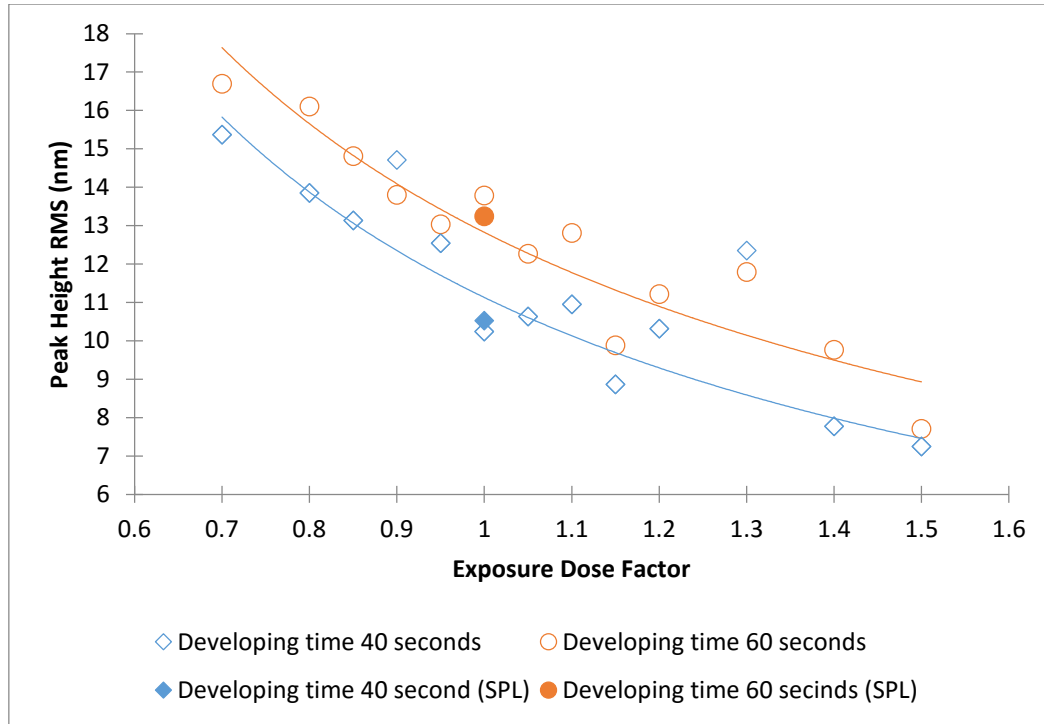
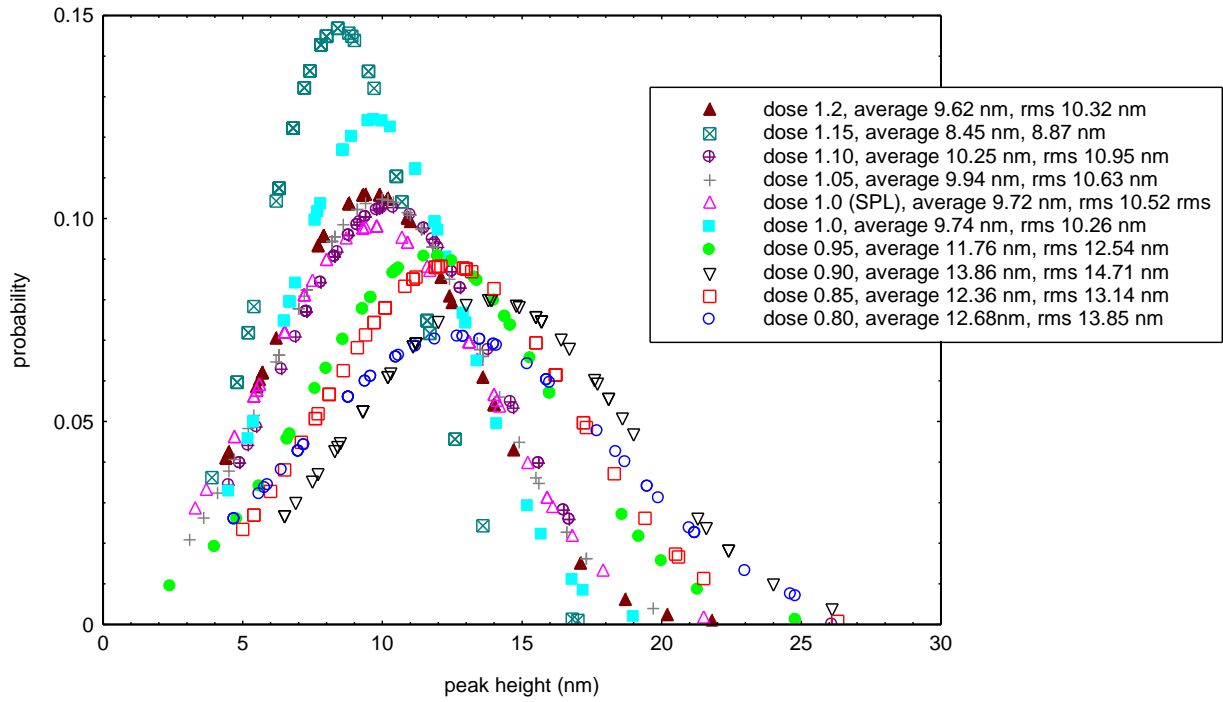


Figure 4.13 : Plot of the peak height of the striated etched facet as a function of exposure dose and development time.

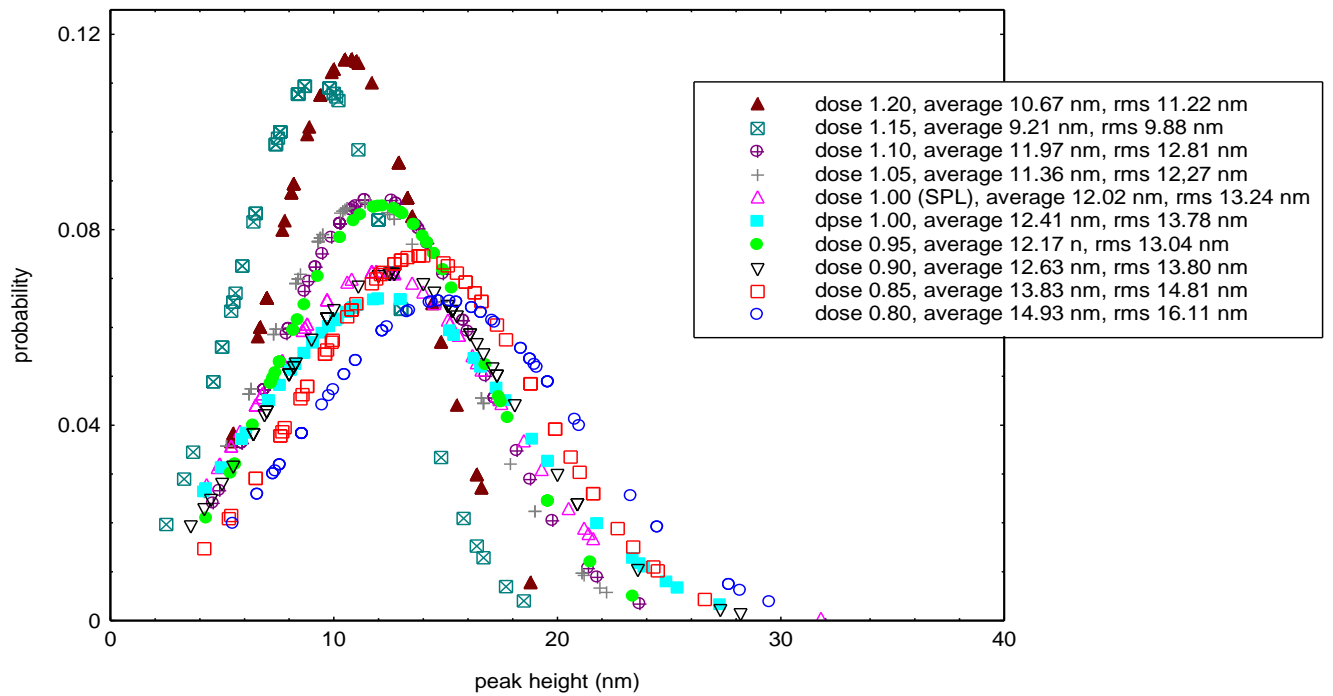
The peak height of the striated pattern is measured and represents the surface roughness of the etched facet. The surface roughness of the facets have been measured in three different areas on the same facet. Figure 4.13 shows the peak height of the striated pattern on the etched facet against exposure dose factor at development time of 40 seconds (blue line) and 60 seconds (red line). The solid markers represent the facet fabricated with a nickel mask with an additional single pixel line exposure at the edge of the pattern during mask patterning. Single pixel line exposure is usually performed for a pattern with crucial dimension criteria. In this study, it was performed to test its capability of performing smooth facet surface. The fabricated etched facet has a Gaussian roughness distribution as shown in Figure 4.14.

As seen in Figure 4.13, the root mean square (rms) surface roughness of facets fabricated with low dose of exposure varies exponentially from 15.37 nm at a dose factor of 0.7 to 7.25 nm at a dose factor of 1.5 for 40 seconds developing time in developing solvent. Similarly for the facets developed for 60 seconds in MIBK:IPA shows the same trend with the surface roughness of facet for a dose factor of 0.7 is 16.70 nm and 7.70 nm for a dose

factor of 1.5. Additional single pixel line exposure doesn't show significant differences from the one without it.



(a)



(b)

Figure 4.14 : The Gaussian roughness distributions for the samples fabricated at different dose factor with a development time of (a) 40 seconds and (b) 60 seconds.

Exposing a mask pattern onto PMMA involves creating regions with a changed solubility [11]. For positive resists, the exposed regions exhibit enhanced solubility of the resists in the development solvent. In PMMA, the increase in solubility is related to changes in the molecular weight distribution [12]. When PMMA is exposed to particles with sufficient energy, in this case it is the electrons, to break chemical bonds in the polymer backbone, it causes scissions in the polymer chain. Main-chain scissions lower the average molecular weight of the polymer. However, these scissions occur at random locations along the polymer chains [13]. Thus, even a polymer chain that experienced a large number of scissions along its backbone may leave polymer fragments with large molecular weights [13].

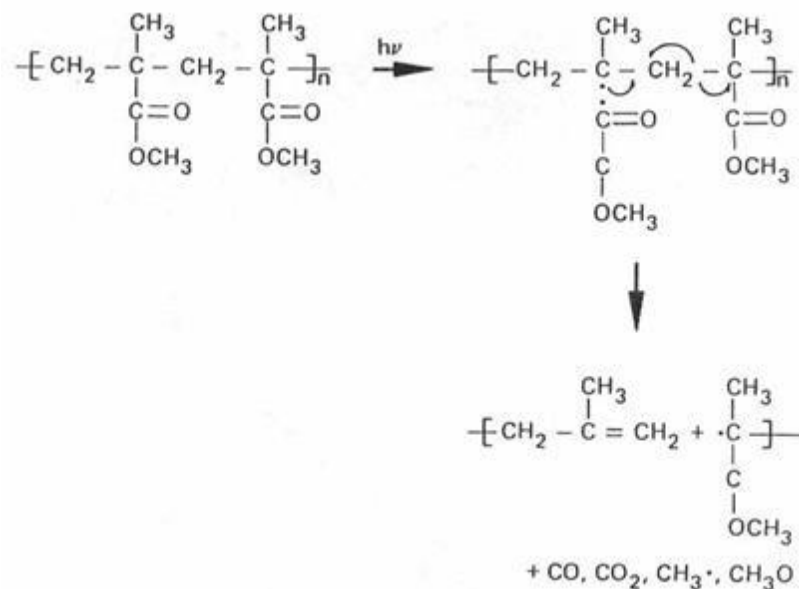


Figure 4.15 : Mechanism of radiation-induced chain scission in PMMA [14].

As the dose increases, the more main chain scissions occurs. Therefore, the average PMMA molecular weight is decreased, resulting in an increase in the solubility of PMMA in the development solvent. The differential dissolution rate between exposed and unexposed PMMA is due to the changes in the molecular weight distribution [15]. The unexposed polymer chains are not free to dissolve, due to entanglement.

The exposed sample has then undergone development process. The development of PMMA is accomplished by removing the exposed material, by dissolution in a developer bath. The developer is only able to dissolve lower molecular weight PMMA [13] [15].



The most common mixture for PMMA development is MIBK and IPA. The ratio of MIBK to IPA can be modified. By varying the ratio of MIBK to IPA, we vary the solubility parameters of the resulting mixture. Increasing the concentration of MIBK increases the solubility of PMMA in the mixture. Ideally, the ratio of MIBK to IPA is selected to optimize the aggressiveness and selectivity of the development solution. However, varying the aggressiveness of the MIBK:IPA developer leads to a trade-off between contrast and sensitivity [16]. For example, increasing the concentration of MIBK:IPA from 1:3 to 1:1 leads to a developer that is a better solvent for PMMA, doubling the sensitivity. However, the unfortunate side effect is that the contrast is nearly halved [17].

In this work, the mixture of MIBK and IPA at the ratio of 1 to 3 is used for developing the samples and the development is done at room temperature. This concentration is favoured because the dissolution rate of unexposed PMMA is almost negligible at this concentration [16]. Stronger developers begin to attack unexposed PMMA while weaker developers sacrifice sensitivity.

Ideally, the developer is thermodynamically a poor solvent, to minimize swelling of the resist, while simultaneously being kinetically a good solvent, to ensure rapid development. This is unfortunately difficult to achieve, as a thermodynamically favorable reaction can have slow kinetics but not vice versa.

During development, the solvent penetrates into the polymer matrix and start to surrounds the fragments. As the molecules start to interact, gel is formed. The thickness of the gel layer will depend on the amount of fragmentation and the strength of the solvent. Swelling of the polymer can also occur. The swelling causes narrow features to close-off during development. Once completely surrounded by solvent, the fragments detach from the matrix and diffuse into solvent [12]. Longer fragments are less mobile and more strongly bound to the matrix and take long time to dissolve.

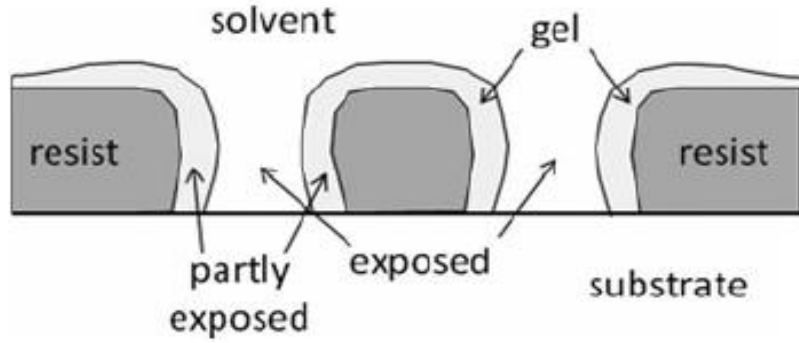


Figure 4.16 : Polymer-solvent interactions can result in gel formation & swelling [6].

After development in MIBK:IPA mixture, the samples is rinsed in IPA to quench the process. However, rinsing can lead to redeposition [12]. In addition to leaving a residue in, otherwise, nominally cleared areas, rinsing will increase the surface roughness [12]. This occurs because the IPA dilutes the developer solution to a weaker solvent, causing PMMA to precipitate out of solution. Hence, a shorter development time is observed to produce better facet.

As mentioned previously, the resist's development involves removal of low molecular weight fragments from the exposed region. This removal can be described as a kinetic diffusion-like process, with a molecular mobility represented by diffusivity,  $D$

$$D \sim n^{-\alpha} \exp\left(-\frac{U}{kT}\right)$$

Equation 4.1

where  $U$  in the activation energy and the factor  $n^{-\alpha}$  describes the mobility fragments of size  $n$  in a medium whose properties are represented by power  $\alpha$ ,  $k$  is Boltzmann constant and  $T$  is temperature [6]. For a moderate exposure dose, the mean size of fragments  $\langle n \rangle$  is inversely proportional to the local probability of a scission which in turn is related to exposure dose,  $d$  so that  $\langle n \rangle \sim 1/d$ , and the diffusivity of fragments in exposed PMMA can be approximately described by:

$$D = cd^{\alpha} \exp\left(-\frac{U}{kT}\right)$$

Equation 4.2

where  $c$  is a location-dependent model coefficient of proportionality [6].

Considering the resist development as a kinetic process involving the diffusion of fragments from exposed resist into a developer solvent, the duration of development is expected to be a controlling factor. Assuming the Fick law of diffusion, removal of resist associated with the diffusion length of PMMA fragments  $(Dt)^{\frac{1}{2}}$ , where effective diffusivity  $D$  is given by Equation 4.1 [6]. As a result, for the width of the development pattern  $\Delta x$ , we can expect the proportionality:

$$\Delta x \sim dt^{\frac{1}{2}}$$

Equation 4.3

where  $d$  is exposure dose. This indicates that optimal dose and development time are related by an inverse proportionality [6]. This theory agrees with the result observed in this work as shown in Figure 4.13 which higher dose factor applied to shorter development time on the sample produces smaller surface roughness. Moreover, reducing the surface roughness value by reducing the development time has also been reported by other authors as well [12] [18].

Electron beam has a very small beam width which only allows local exposure at one time. The beam width that is used in this work is 20  $\mu\text{m}$  with 10 kV accelerating voltage. To write the whole pattern of the facet mask, the beam is doing point by point scanning and each exposure is within a predetermine write field. This serial process makes the writing process a very slow process. As dose increases, the electrons are having more irradiation time at each write field. Thus, more electrons irradiate the resist results in a higher chance main-chain scission to occur. This situation could lead to having a slightly bigger pattern than expected since the average fragment size decreases and solubility in the developer increases causing more fragment to be carried away during development. Additionally, electron irradiation may create secondary electrons [19], which, because they are undirected, effectively widen the beam.

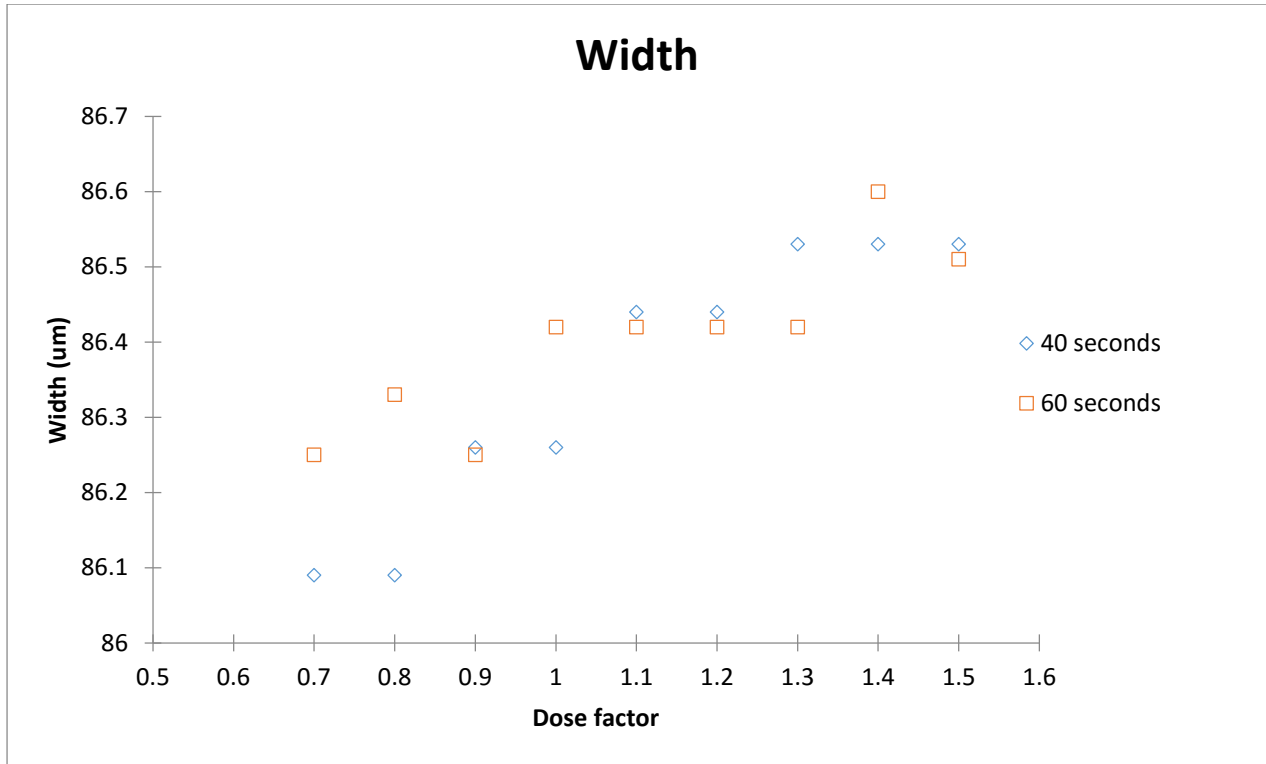


Figure 4.17 : Width of the etched facet pattern for the sample fabricated with different dose factor and were developed at 40 seconds and 60 seconds.

Figure 4.17 shows the width of the etched facets that were fabricated using a nickel mask with different applied dose factor during mask patterning. Facets fabricated at both development time show similar trend which is the width of facet increases as the applied dose factor increasing. However, the increment is not really significant as the difference between the highest and smallest value measured is just 0.51  $\mu\text{m}$ .

The standard roughness assumed tolerable is  $\lambda/10$  [20]. The wafer used in this work has the wavelength  $\lambda$  of 635 nm. The highest value of surface roughness obtained from the sample with 40 seconds development time is 15.37 nm while the lowest is 7.25 nm. The surface roughness value of the sample with 60 seconds development time is 16.70 nm the highest and 7.70 nm the lowest. Since the surface roughness value obtained in this work has been much lower than  $\lambda/10$ , the aims mentioned in the introduction section to produce laser facets that are vertical, nearly atomically flat and etched through the vertical extent of the epitaxial growth layer on the semiconductor crystal into the GaAs substrate that is comparable with the cleaved facet is considered accomplished. However,

since the facet roughness will consequently affect the laser performance, some measurement has been performed in order to characterize this facet performance.

## 4.5 Characterization of Cleaved Facet and Etched Facet

### 4.5.1 Reflectivity

There is no minimum reflectivity required for laser action as the round trip gain can be increased by lengthening the cavity or coating the facet. However, the performance and efficiency of the fabricated laser device are strongly affected by facet roughness. To determine the reflectivity of the fabricated etched facet, the reflected wave is treated as a superposition of Huygens elementary waves generated at the facet surface. For a laser cavity, only the specular reflection of normally incident light at the facet is considered. The optical path length difference experienced by each wave as it is reflected from the uneven surface, introduces a corresponding phase difference with respect to the rest. Since the laser cavity has facet with the rms roughness of  $\Delta d$  that follows a Gaussian distribution, an analytical expression for the ratio of the actual power reflectivity to the power reflectivity for a perfectly smooth facet,  $R_o$  has been derived [21] and is given by:

$$\frac{R(\Delta d)}{R_o} = e^{-16\pi^2 \left(\frac{n\Delta d}{\lambda}\right)^2}$$

Equation 4.4

where  $\Delta d$  is the root mean square roughness of the facet surface,  $\lambda$  is the wavelength of the laser light inside the semiconductor and  $n$  is the refractive index of the semiconductor. The  $\lambda$  for the wafer used in this work is 635 nm and the corresponding refractive index,  $n$  is 3.42. Table 4.4 shows the rms surface roughness and reflectivity value of the entire fabricated etched facet calculated from the Equation 4.4.

A typical power reflectivity for a cleaved facet  $R_o$  is 0.3. From the data in Table 4.2, a fabricated etched facet with dose factor of 1.5 and development time of 40 seconds has the highest value of facet reflectivity which is 0.24. The reduced reflectivity of the etched facet laser is due to a phase broadening effect [21].

Table 4.4 : Summary of the measured value of surface roughness and calculated efficiency.

Dose factor	Development time 40 seconds		Development time 60 seconds	
	RMS of surface roughness, $(\Delta d)$ (nm)	Reflectivity, $R (\Delta d)$	RMS of surface roughness, $(\Delta d)$ (nm)	Reflectivity, $R (\Delta d)$
0.70	15.37	0.10	16.70	0.08
0.80	13.85	0.12	16.11	0.09
0.85	13.14	0.14	14.81	0.11
0.90	14.71	0.11	13.80	0.13
0.95	12.54	0.15	13.03	0.14
1.00	10.25	0.19	13.78	0.13
1.00 (SPL)	10.52	0.18	13.24	0.13
1.05	10.63	0.18	12.27	0.15
1.10	10.95	0.18	12.81	0.14
1.15	8.87	0.21	9.88	0.19
1.20	10.37	0.18	11.22	0.17
1.30	12.35	0.15	11.79	0.16
1.40	7.77	0.23	9.77	0.19
1.50	7.25	0.24	7.70	0.23

### 4.5.2 Threshold Current Density

Measurement of current threshold and near field were conducted in order to determine the efficiency of laser fabricated with etched facet as compared to cleaved facet. Etched facet laser devices fabricated with different dose factor during mask patterning were prepared for this purpose. Only the device with 40 seconds development time were fabricated since it is proven that it has a better surface roughness compared to the one with 60 seconds development time.

### 4.5.2.1 Oxide Stripe Laser Device

The oxide stripe lasers with cleaved-cleaved facets and cleaved-etched facets were used to measure a threshold current and near field for characterization of the etched facet and cleaved facet. Figure 4.18 shows the schematic diagram of cleaved-cleaved facets laser and cleaved-etched facets laser. Like the multisection device mentioned in previous chapter, the lasers also have an oxide isolated stripe geometry with a  $50\text{ }\mu\text{m}$  stripe width. The p-contact layer at the top of the device consists of Gold-Zinc (Au-Zn), while n-contact layer at the bottom of the device consists of GoldGermanium-Nickel-Gold (AuGe-Ni-Au). The device length corresponds to the cavity length and reflectivity is due to semiconductor air-interface and electromagnetic modes emit from both facets. However, for cleaved-etched facets laser, the p-contact layer is patterned  $5\text{ }\mu\text{m}$  short of the edge of the etched facet to avoid loss of pattern definition due to over exposure of the thinner resist in this area. The fabricated lasers are from the same wafer as multisection devices and exposed to similar processing conditions throughout fabrication. The devices were held on a copper mount.

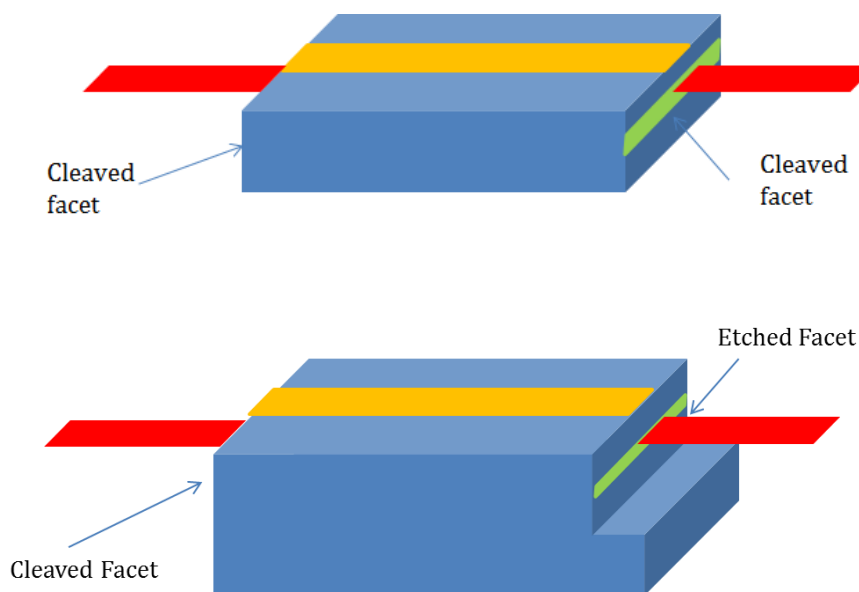


Figure 4.18 : Schematic diagram of cleaved-cleaved facets laser and cleaved-etched facets laser.

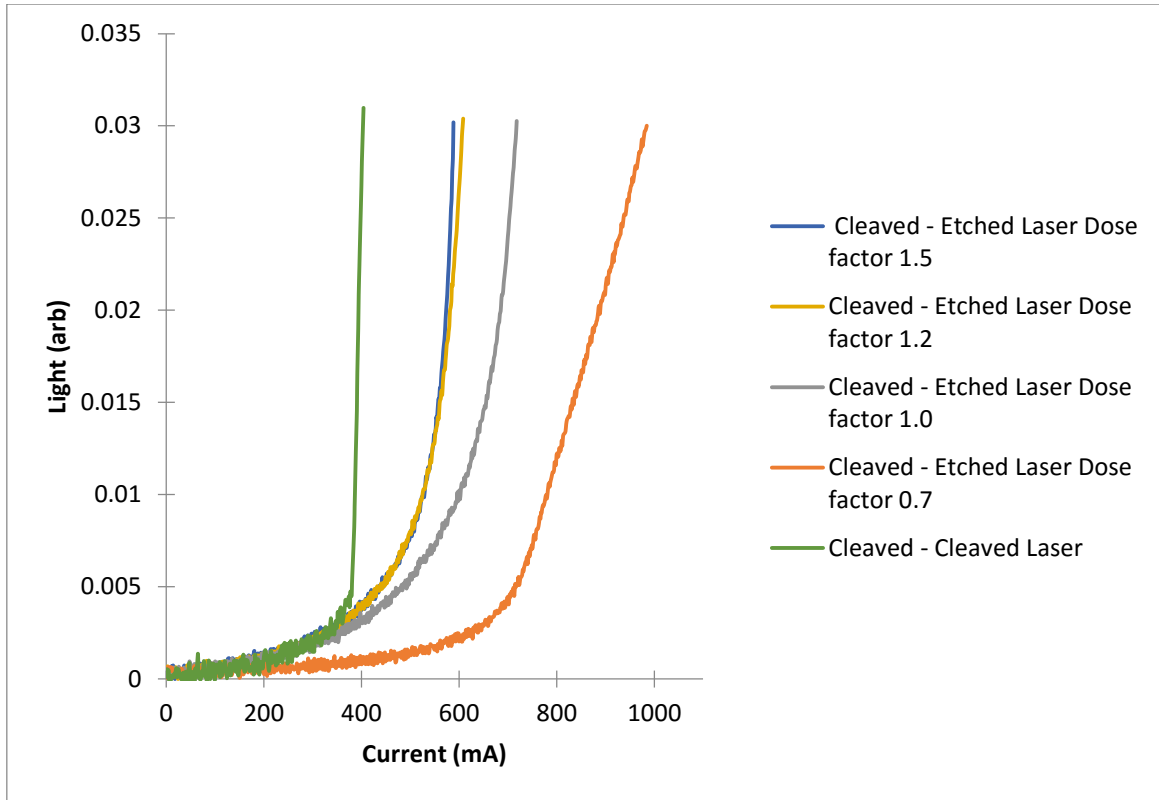


Figure 4.19 : Light-current (L-I) curves for a cleaved – cleaved facets laser and cleaved-etched facets lasers for various dose factors applied during the mask patterning process.

Figure 4.19 shows the light-current (L-I) curves for a cleaved – cleaved facets laser and cleaved-etched facets laser fabricated with various dose factors applied during the mask patterning process. Laser threshold current,  $I_{th}$  is obtained from the knee in L-I curve. The mode width of each of the devices has been calculated by measuring the full width half maximum (FWHM) value of near field intensity distribution across the facet. The length of each device has been measured using a calibrated optical microscope. These measurements allow the threshold current density,  $J_{th}$  to be calculated by dividing the measured  $I_{th}$  by the product of device length and mode width as mentioned in Equation 3.8. This information has been summarized in Table 4.5.



Table 4.5 : Summary of the measured values used to calculate device threshold current density.

Device	$I_{th}(mA)$	Length ( $\mu m$ )	Width ( $\mu m$ )	$J_{th}$ ( $A/cm^2$ )
Cleaved – etched laser with exposure dose factor of 0.7	714	1018	68	1024
Cleaved – etched laser with exposure dose factor of 1.0	632	981	66	980
Cleaved – etched laser with exposure dose factor of 1.2	541	991	70	776
Cleaved – etched laser with exposure dose factor of 1.5	541	934	77	754
Cleaved – cleaved laser	378	1001	53	705

The threshold current densities,  $J_{th}$  for cleaved-etched devices has been plotted in Figure 4.20. The result shows that the threshold current density,  $J_{th}$  is decreasing with an increasing application of dose factor. Meanwhile, the device with cleaved – cleaved device has the lowest value of threshold current density. This result proves that surface roughness do have a significant effect on the performance of laser devices.

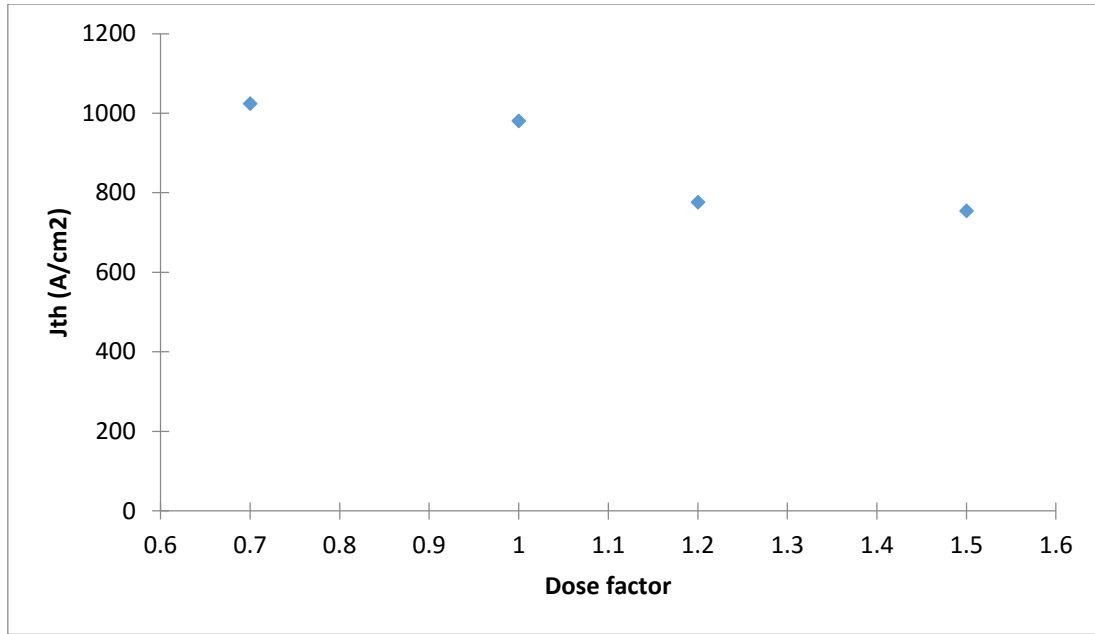


Figure 4.20 : Plot of threshold current density,  $J_{th}$  for cleaved-etched devices that were fabricated with various dose factors applied during mask patterning.

### 4.5.3 Efficiency

A direct measure of the ability of the device converting the input electric power to output light power is done by measuring the slope of the light output power – current curve, as shown in Figure 4.21.  $\frac{\Delta P}{\Delta I}$  which is the slope of the light output power - current curve above the threshold current,  $I_{th}$ , represents how many Watts of power the laser outputs for every 1 Amp increase in its input current. External quantum efficiency,  $\eta_{ext}^d$  and internal quantum efficiency,  $\eta_{int}^d$  can be extracted from the measurement of  $\frac{\Delta P}{\Delta I}$  parameter. The device is placed in the integrated sphere during the measurement to ensure that all generated light is detected and measured.

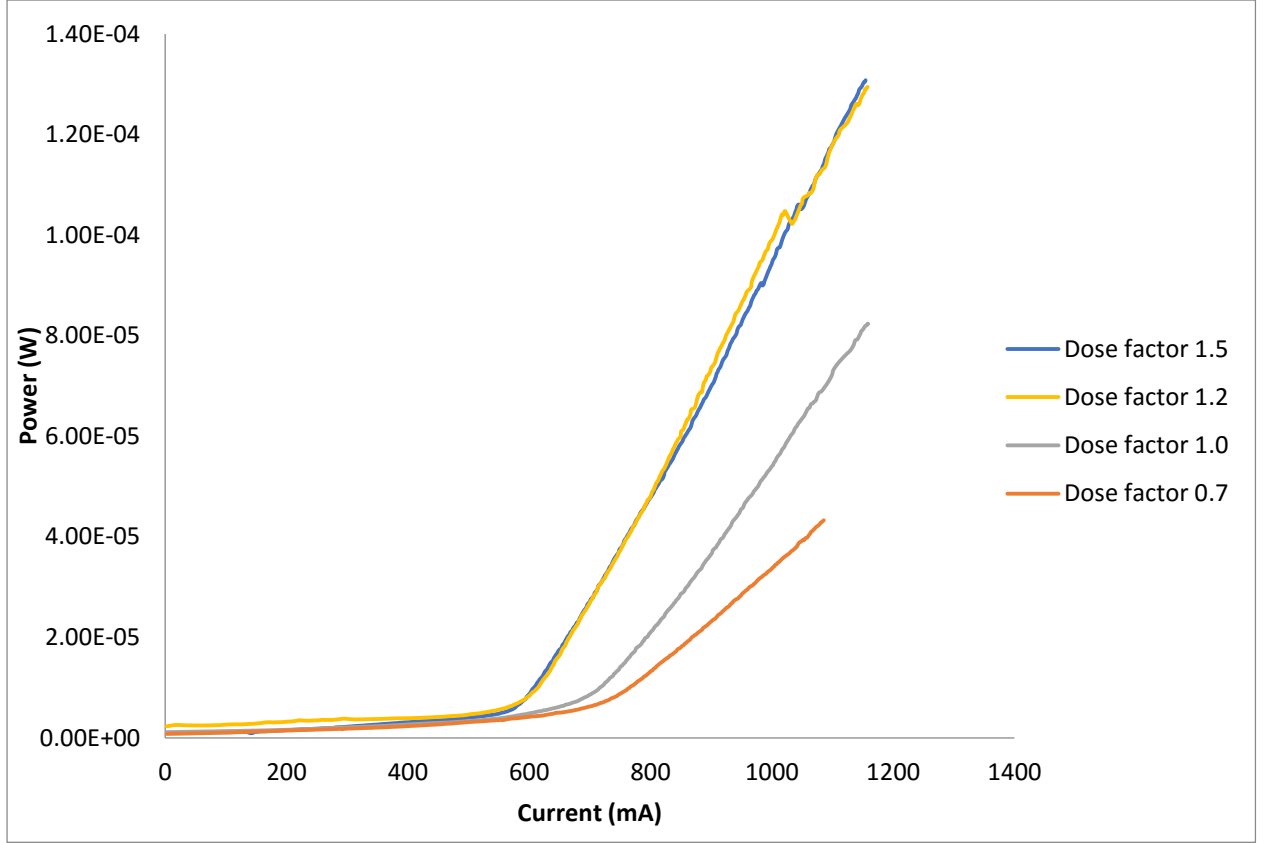


Figure 4.21 : Plot of power against current for cleaved-etched devices that were fabricated with various dose factors applied during mask patterning.

#### 4.5.3.1 External Quantum Efficiency, $\eta_{ext}^d$

External quantum efficiency,  $\eta_{ext}^d$  indicates the efficiency of laser device in converting the injected electron-hole pairs to photon emitted from the device. It is obtained from the slope of light output power,  $P$  plotted as a function of injected current,  $I$  that is measured above threshold current,  $I_{th}$ . External quantum efficiency is a unit-less parameter given in percentage form and it is describe as:

$$\eta_{ext}^d = \frac{2e}{hv} \frac{\Delta P}{\Delta I}$$

Equation 4.5

where  $hv$  is the photon energy of the laser light and  $e$  is the electric charge. The devices used in this measurement have cleaved-etched facets. All the light detected and measured in this measurement is coming from the front facet which is the etched facet and therefore the calculated  $\eta_{ext}^d$  is per one facet.

### 4.5.3.2 Internal Quantum Efficiency, $\eta_{int}$

Internal quantum efficiency,  $\eta_{int}^d$  is a parameter that indicates the efficiency of laser in converting electron-hole pair (injected current) into photons within the laser structure.

This parameter is related to  $\eta_{ext}^d$  by:

$$\frac{1}{\eta_{ext}^d} = \frac{1}{\eta_{int}^d} \left[ \frac{\alpha_i L}{\ln \frac{1}{R_1 R_2}} + 1 \right]$$

Equation 4.6

where  $L$  is the length of the laser cavity,  $R_1$  is the reflectivity of the cleaved facet,  $R_2$  is the reflectivity of the etched facet and  $\alpha_i$  is the internal mode loss. The measurement of  $\alpha_i$  for this material has been performed (discussed in chapter 3) and the measured value of  $\alpha_i$  for this material at room temperature is  $13 \text{ cm}^{-1}$ . Table 4.6 gives the summary of the measured  $\frac{\Delta P}{\Delta I}$ , calculated  $\eta_{ext}^d$  and  $\eta_{int}^d$  of laser devices fabricated with different value of dose factor during mask patterning.

Table 4.6 : Summary of the measured slope and calculated external quantum efficiency of laser devices fabricated with different value of dose factor during mask patterning.

Dose factor	$\Delta P / \Delta I$	$\eta_{ext}^d$ (%)	$\eta_{int}^d$
0.7	$1.04 \times 10^{-04}$	10.7	0.12
1.0	$1.70 \times 10^{-04}$	17.4	0.22
1.2	$2.54 \times 10^{-04}$	26.0	0.32
1.5	$2.35 \times 10^{-04}$	24.1	0.32

Results from Table 4.5 show an increasing  $\eta_{ext}^d$  as well as  $\eta_{int}^d$  as the application of dose factor is increasing. These results indicate that the device fabricated with higher dose factor is able to produce more photon emitted from the device, therefore producing more gain, as compared to the device fabricated with lower dose factor.

### 4.5.4 Mirror Loss

The proposed prototype of a coupled cavity living laser in this study has the minimum length of 600  $\mu\text{m}$ . This length is chosen because it is easy to facilitate the cleaving process with the length of 500  $\mu\text{m}$  and above. The detail dimension and design of the proposed prototype will be discussed in Chapter 6. From the results obtained in this chapter, the proposed prototype of a coupled cavity living laser will use dose factor of 1.5 and 40 seconds developing time during electron beam lithography process with nickel mask for semiconductor etch. With  $R_1$  as the reflectivity of cleaved facet is 0.30 and  $R_2$  as the reflectivity of etched facet is 0.24, the mirror loss,  $\alpha_m$  for the individual laser can be calculated from the equation below:

$$\alpha_m = \frac{1}{2L} \ln \frac{1}{R_1 R_2}$$

Equation 4.7

The calculated value of  $\alpha_m$  for 600  $\mu\text{m}$  laser with cleaved-etched facet is  $21 \pm 1 \text{ cm}^{-1}$ .

## 4.6 Conclusion

This chapter discusses the fabrication process of etched facet and its characterization. Starting from a selection of the etching mask, nickel and silicon dioxide were tested as a mask for the etching process. Silicon dioxide produced a striated etched facet with terracing effect due to volatile etchant reaction with a silicon dioxide mask during inductively couple plasma etching process. On the other hand, etched facet fabricated with nickel mask is free from terracing effect since there is no reaction between metal mask and etchant during plasma etching of semiconductor. The air plasma etch and oxygen plasma etch has been tested to remove the remaining resist on the bottom of the mask pattern. Air plasma has not been used for the fabrication of etched facet because the redeposited residue on the nickel mask creates bubble on the mask.

The best recipe for electron beam lithography process that is able to produce the etched facet with the smooth surface is investigated. Varies dose factor were applied during exposure of the electron beam as well as developed the mask at the different development time. The surface roughness of fabricated etched facets were measured. The results show that the fabricated etched facet has a Gaussian surface height distribution with the best facet fabricated with high dose factor, i.e. 1.5, and low development time, i.e. 40 seconds, has a reflectivity of 0.24 as compared to cleaved facet with a reflectivity of 0.30. Application of high dose doesn't have a significant effect on the size of the pattern.

Devices with cleaved-etched facets fabricated with different dose factor at 40 seconds development time were prepared for characterization of etched facet. A light – current characteristics of the cleaved – etched devices have been measured and used to calculate the threshold current densities and efficiencies of these devices. The results show that a device with better surface roughness, i.e. device fabricated with high dose at low development time, gives low current threshold density,  $J_{th}$  which is  $754 \text{ Acm}^{-2}$  with the external quantum efficiency,  $\eta_{ext}^d$  of 24.1% and internal quantum efficiency,  $\eta_{int}^d$  of 0.32. Lastly, the calculated mirror loss  $\alpha_m$  for the proposed prototype of a coupled cavity living laser for the minimum cavity length of  $600 \mu\text{m}$  is  $21 \pm 1 \text{ cm}^{-1}$ .

## 4.7 Bibliography

- [1] P. Rai-Choudhury, Handbook of Microlithography, Micromachining and Microfabrication Volume 1 : Microlithography, USA: SPIE, 1997.
- [2] M. Altissimo, "E-beam lithography for micro-/nanofabrication," *Biomicrofluidics*, vol. 4, 2010.
- [3] "AZoNano," [Online]. Available: <http://www.azonano.com/article.aspx?ArticleID=2953#14>.
- [4] E. A. Dobisz, R. Bass, S. L. Brandow, M.-S. Chen and W. J. Dressick, "Electroless metal discharge layers for electron beam lithography," p. 478, 2003.
- [5] M. A. McCord and M. j. Rooks, Handbook of Microlithography, Micromachining and Microfabrication, Bellingham, Washington: SPIE Optical Engineering Press, 1997.
- [6] M. Stepanova and S. K. Dew, Nanofabrications Techniques and Principles, New York: Springer, 2012, pp. 11 - 41.
- [7] N. R. Rueger, M. F. Doemling, M. Schaepekens, J. J. Beulens, T. E. F. M. Standaert and G. S. Oehrlein, "Selective Etching of SiO<sub>2</sub> over Polycrystalline Silicon using CHF<sub>3</sub>," *Vacuum Science and Technology A*, vol. 17, no. 5, p. 2492, 1999.
- [8] P. S. Hsu, R. M. Farrel, J. J. Weaver, K. Fujito, S. P. DenBaars, J. S. Speck and S. Nakamura, "Comparison of Polished and Dry Etched Semipolar (1122) III-Nitride Laser Facet," *IEEE Photonics Technology Letters*, vol. 25, no. 21, pp. 2105-2107, 2013.
- [9] A. C. Abere, M. P. Mack, M. Hansen, R. K. Sink, P. Kozodoy, S. Keller, J. S. Speck, J. E. Bowers, U. K. Mishra, L. A. Coldren and S. P. DenBaars, "Cleaved and Etched Facet Nitride Laser Diodes," *IEEE Journal of Selected Topics in Quantum Electronics*, vol. 4, no. 3, pp. 505-509, 1998.

- [10] H. Saito and Y. Noguchi, "InGaAs/InP Etched Mirror Laser Fabricated by Inclined RIE," *Japanese Journal of Applied Physics*, vol. 28, no. 10, pp. 1836-1842, 1989.
- [11] M. Mohsin and M. G. Cowie, "Enhanced sensitivity in the electron beam resist poly(methyl methacrylate) using improved solvent developer," *Polymer*, vol. 29, no. 12, pp. 2130-2135, 1988.
- [12] S. Yasin, M. N. Khalid and D. G. Hasko, "Reduction in Roughness of Resist Features in PMMA due to the Absence of a Rinse," *Japanese Journal of Applied Physics*, vol. 43, no. 10, pp. 6984-6987, 2004.
- [13] R. A. Harris, "Polymethyl methacrylate as an electron sensitive resist," *Journal of the Electrochemical Society*, vol. 120, no. 2, pp. 270-274, 1973.
- [14] "Henderson Research Group, School of Chemical and Biomolecular Engineering, Georgia Institute of Technology," [Online]. Available: <http://henderson.chbe.gatech.edu/Introductions/intro%20to%20e-beam%20lithography.htm>.
- [15] H. Y. Ku and L. C. Scala, "Polymeric Electron Beam Resist," *Journal of the Electrochemical Society*, vol. 116, no. 7, pp. 980-985, 1969.
- [16] A. Olzierski and I. Raptis, "Development and molecular-weight issues on the lithographic performance of poly (methyl methacrylate)," *Microelectronic Engineering*, vol. 73, no. 74, pp. 244-251, 2004.
- [17] S. Yasin, D. G. Hasko and H. Ahmed, "Fabrication of <5 nm width lines in poly(methylmethacrylate) resist using a water:isopropyl alcohol developer and ultrasonically assisted development," *Applied Physics Letters*, vol. 78, no. 18, pp. 2760-2762, 2001.
- [18] J.-S. Wi, H.-S. Lee and K.-B. Kim, "Enhanced Development Properties of IPA(Isopropyl Alcohol) on the PMMA Electron Beam Resist," *Electronics Materials Letters*, vol. 3, no. 1, pp. 1-5, 2007.



- [19] S. P. Beaumont, P. G. Bower, T. Tamamura and C. D. W. Wilkinson, "Sub20nmwide metal lines by electronbeam exposure of thin poly(methyl methacrylate)," *Applied Physics Letters*, vol. 38, no. 6, pp. 436-439, 1981.
- [20] D. A. Francis, C. J. ChangHasnain and K. Eason, "Effect of Facer Roughness in Etched Facet Semiconductor Laser Diodes," *Applied Physics Letters*, vol. 68, no. 12, pp. 1598-1600, 1996.
- [21] D. A. Stocker, E. F. Schubert, W. Grieshaber, K. S. Boutros and J. M. Redwing, "Facet Roughness Analysis for InGaN/GaN Lasers with Cleaved Facets," *Applied Physics Letters*, vol. 73, no. 14, pp. 1925-1927, 1998.

## **Chapter 5 : The Prototype Of A Coupled Cavity Living Laser**

### **5.1 Introduction**

The development of microfluidic lab-on-chip systems for full blood count or cell analysis has exploited the use of integrated circuits with basic building blocks such as resistors, capacitors, transistors and comparable set of mechanisms such as valves [1], pumps [2] and mixers [3] for cell sorting and parameter detection. On the other hand, the application of lasers in a bulky flow cytometer system is common [4] [5] [6]. In this work, I take the first steps to integrate the application of a laser as a source and/or detector in the microfluidic lab-on-chip system.

The development of a procedure for the fabrication of a prototype of a couple cavity living laser device that can operate as a lab-on-chip for cell analysis has been one of the primary objectives of this work. A microfluidic channel will be integrated in an optically active semiconductor substrate. This chapter describes the design and fabrication work that I have undertaken during the project to develop a prototype of a coupled cavity living laser. The choice of active medium material and the technique used for fabrication of etched facets are determined by the preliminary characterization experiments and test results obtained in previous chapters. Then, the measurement taken for the operational trial of the prototype will be reported.

## 5.2 Design And Fabrication Of The Prototype Of A Coupled Cavity Living Laser

The proposed design of the prototype of a coupled cavity living laser is shown in Figure 5.1. The device consists of a pair of coupled cavity broad area oxide stripe lasers separated by a channel etched into the semiconductor wafer. The fabrication of this prototype is made with the quantum well material. These laser cavities are fabricated from UWIC 412 1608c single quantum well material of GaInP/AlGaInP on a n-type GaAs substrate emitting at 635 nm. The wafer was commercially grown by IQE using metal-organic chemical vapour deposition (MOCVD). The operating characteristics of the detector cavity will be dependent on the light which is coupled to it from the opposite source cavity.

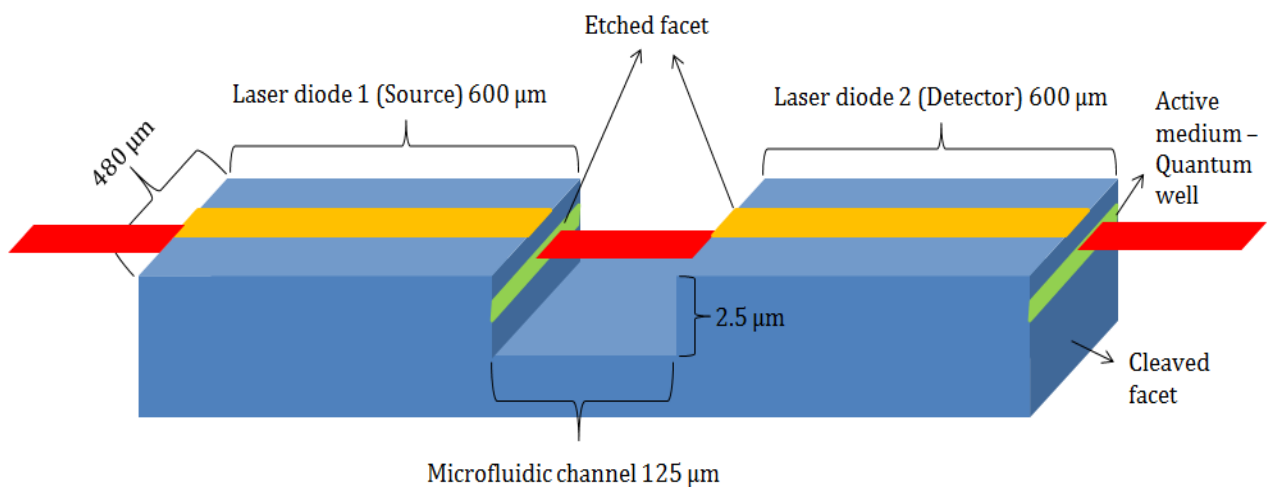


Figure 5.1 : Proposed design of the prototype of coupled cavity living laser.

The monolithic nature of the device gives an intrinsic alignment of the active layers of the material. Integrating a microfluidic system into the channels allows the cells to be delivered directly between opposite cavities of the coupled cavity lasers. The width of the channel is 125 μm and its depth is about 2.5 μm. This dimension is chosen in order to facilitate a stream of red blood cells that having an individual average dimension of

approximately 7.5 to 8.7  $\mu\text{m}$  in diameter and 1.7 to 2.2  $\mu\text{m}$  in thickness [7]. The channel is formed by inductively coupled plasma etching (ICP) process as described in Chapter 4. This ICP etching process also formed the inner facets for the laser cavities. The detailed recipe and procedure for electron beam lithography (EBL) involved prior to etching process is described in Chapter 4. The attenuation of light caused by absorption and scattering from the cells will affect the strength of the light being coupled into the detector cavity. This effect will have a measurable result of the spectral and power output of the device.

Like the oxide stripe cleaved- etched laser device mentioned in Chapter 4, the lasers in this prototype also have an oxide isolated stripe geometry with a 50  $\mu\text{m}$  stripe width. The p-contact layer at the top of the device consists of Gold-Zinc (Au-Zn), while the n-contact layer at the bottom of the device consists of GoldGermanium-Nickel-Gold (AuGe-Ni-Au). In the end, the device is cleaved into desired length, forming the outer cleaved facets. For the testing measurement purposes, the device is mounted onto the transistor header. Table 5.1 shows the complete processing procedure of the prototype of a coupled cavity living laser made in this work.

Table 5.1 : Processing procedure of the prototype of coupled cavity living laser.

No.	Processing steps	Details
1	Scribe and cleave sample.	The sample is scribed and cleaved with the dimension of 6 mm x 9 mm.
2	Clean.	The sample is cleaned using acetone in an ultrasonic bath for 10 minutes, followed by trichloroethylene, acetone, methanol and isopropyl cleaning on a hot plate at 80 °C for 5 minutes for each of the solvents to remove any contaminations on the surface of the wafer. The sample is then blown dried using a nitrogen gun.

3	Electron beam lithography for the mask of laser/channel.	<p>The recipe for this process are as follows:</p> <ol style="list-style-type: none"> <li>i. Spin coated PMMA A4 at 5000 rpm for 45 seconds.</li> <li>ii. Bake PMMA A4 for 3 minutes on 180 °C hot plate.</li> <li>iii. Expose in Eline Lithography Machine with operating parameter as below: <ul style="list-style-type: none"> <li>- Working distance 10 mm</li> <li>- EHT voltage 10kV</li> <li>- Aperture 20 um</li> <li>- Beam current 0.16 nA</li> <li>- Magnification 1000x</li> <li>- Step size U 0.02 um</li> <li>- Step size V 0.02 um</li> <li>- Dwell time 0.004178 ms</li> <li>- Nominal dose 165 uC/cm<sup>2</sup></li> <li>- Dose factor 1.5</li> </ul> </li> <li>iv. Developed the sample in 1 potion of MIBK to 3 potions of isopropyl for 40 seconds, followed by isopropyl rinse for 30 seconds.</li> </ol>
4	Oxygen etch.	<p>To remove any PMMA left on the facet/channel pattern, oxygen etch is performed using the ICP machine with following working parameter:</p> <ul style="list-style-type: none"> <li>- 50 W of RIE power</li> <li>- 40 sccms of oxygen</li> <li>- 50 forward bias</li> <li>- 10 torr chamber pressure</li> <li>- 10 torr helium</li> <li>- 28 °C room temperature</li> <li>- 10 secs etch time</li> <li>- no ICP power</li> </ul>

5	Formation of nickel mask.	<p>The procedure for formation of nickel mask are as follows:</p> <ol style="list-style-type: none"> <li>Evaporate nickel with thickness of 60 nm.</li> <li>Lift off nickel in acetone.</li> </ol>
6	ICP etch semiconductor.	The nickel mask is used to transfer the pattern into the semiconductor crystal using a high temperature (200 °C) Ar/Cl <sub>2</sub> ICP etch.
7	Nickel etch.	To remove the nickel mask, the sample is dipped into 42.5 ml DI water and 5 ml HNO <sub>3</sub> for 2 minutes, followed by a deionized water rinse for another 2 minutes.
8	SiO <sub>2</sub> evaporation.	The thickness of SiO <sub>2</sub> is 120 nm.
9	Bake SiO <sub>2</sub> .	The SiO <sub>2</sub> is then baked in the Rapid Thermal Annealing (RTA) machine to remove all the moisture trapped inside it.
10	Photolithography of 50 µm oxide stripes.	<p>The recipe for photolithography of 50 µm oxide stripes are as follows:</p> <ol style="list-style-type: none"> <li>Spin coated resist S1813 for 45 seconds with the speed of 6000 rpm.</li> <li>Soft bake the resist for 3 minutes on 100 °C hot plate.</li> <li>Expose the pattern with high precision setting for 6 seconds.</li> <li>Develop the pattern with AZ developer for 45 seconds, followed by a deionized water rinse for 45 seconds.</li> <li>Hard bake the resist on a 100 °C hot plate for 3 minutes.</li> <li>Etch the oxide with HF etch for 9 seconds.</li> </ol>

		<p>vii. Remove the resist by dipping the sample in acetone on 80 °C hot plate for 10 minutes, followed by isopropyl rinse afterwards.</p>
11	Formation of p- contact layer.	<p>The process of forming p-contact of the device are as follows:</p> <ol style="list-style-type: none"> <li>i. Evaporation of of GoldZinc (AuZn) with the thickness Zn is 10 nm and Au is 300 nm. The evaporation is done at high temperature (220 °C).</li> <li>ii. Photolithography of contact pads that will be the mask for Gold etch later on to remove the AuZn from the channel and spaces in between the lasers.</li> <li>iii. Spin coated resist S1813 for 45 seconds with the speed 6000 rpm.</li> <li>iv. Soft bake the resist for 3 minutes on 100 °C hot plate.</li> <li>v. Apply contact pad mask.</li> <li>vi. Expose the pattern with high precision setting for 6 seconds.</li> <li>vii. Develop the pattern with AZ developer for 45 seconds, followed by a deionized water rinse for 45 seconds.</li> <li>viii. Hard bake the resist on a 100 °C hot plate for 3 minutes.</li> <li>ix. Gold etch AuZn for about 2 minutes, followed by a deionized water rinse for another 2 minutes.</li> <li>x. Remove the resist by dipping the sample in acetone on 80 °C hot plate for 10 minutes, followed by isopropyl rinse afterwards.</li> <li>xi. Anneal the p-contact layer in the RTA machine.</li> </ol>

12	Formation of n-contact layer. Lap & polish (KB)	<p>The process of forming n-contact of the device are as follows:</p> <ol style="list-style-type: none"> <li>Lap the bottom side of the sample until the thickness become about 100 <math>\mu\text{m}</math>.</li> <li>Polish the sample for 2 minutes.</li> <li>Evaporate AuGe/Ni/Au with the thickness of AuGe 100 nm, Ni 28 nm and Au 300 nm.</li> <li>Anneal the n-contact layer in the RTA machine.</li> </ol>
13	Cleave and mount.	Cleaved the outer facets of the device with the desired cavity length and finally mount it on the transistor header or further analysis.

### 5.3 Far Field Measurement

The far field measurement is used to establish the fraction of light passed from one section of laser (source) to the other (detector).

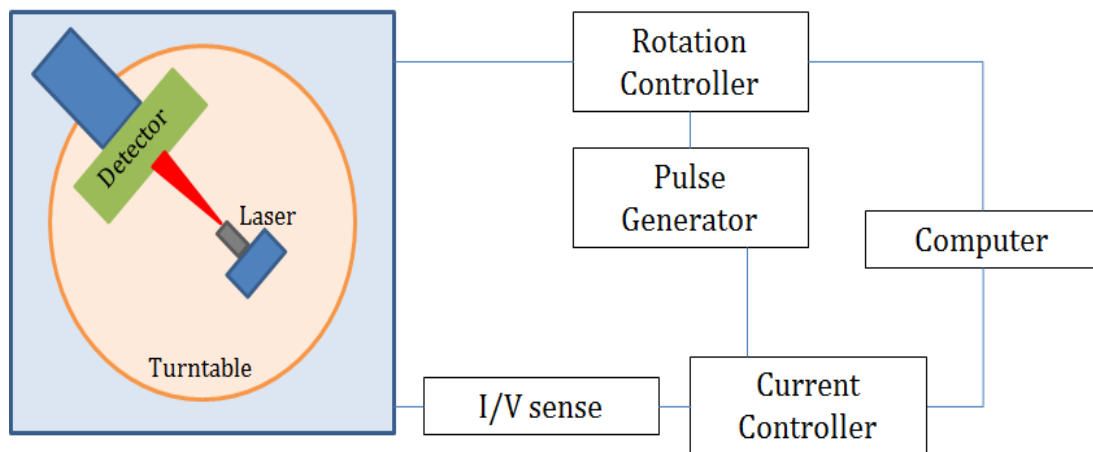


Figure 5.2 : Schematic diagram of far field measurement apparatus.

Figure 5.2 shows the schematic diagram of the far field measurement apparatus used in this work. The cleaved – etched laser device that is fabricated with quantum well active



medium with an optimum recipe for electron beam lithography during facet formation as described in Chapter 4 was mounted on the translation stage at the center of rotation of the turntable. The light from etched facet is detected by the photodetector mounted in a fixed position facing towards the device. The photodetector was mounted on an adjustable arm which allows the distance between the laser device and the photodetector to be varied. The current is supplied to the device through the pulse generator. This current was set using a computer operated current controller in combination with current/voltage (I/V) detector. A computer operated rotation controller allow the device to be rotated, which progressively steps the far field beam profile of the laser device across the detector. Every step of movement by turntable give  $0.67^\circ$  of angular movement.

The width of the active medium under the contact stripe is  $50\text{ }\mu\text{m}$  (parallel to the plane of epitaxial growth) is much larger than the emitted wavelength of the device which is  $635\text{ nm}$ . Therefore, the diffraction is considered to be negligible in this direction. However, the thickness of active medium (perpendicular to the plane of epitaxial growth) is very small, and is in the order of the wavelength of emission of the devices. Hence, the diffraction is the greatest in this plane. Therefore, in order to measure the angular far field intensity profile caused by this diffraction, the device is mounted on the device holder with the plane of active medium perpendicular to the plane of rotation. In order to improve the angular resolution of the measurements, only light that passed through a narrow slit mounted on the front of photodetector was measured.

Figure 5.3 shows the normalized angular far field profile of etched facet operating above threshold current having an angular far field divergence  $\theta$  of  $25^\circ$  at  $1/e$  of the amplitude. From a private communication with Prof. Peter Smowton, the total mode width of this particular material which represented by  $w_0$  is  $0.25\text{ }\mu\text{m}$ . The fractional overlap of the electric field profile which leaves the waveguide and the electric field profile after travelling a distance of  $125\text{ }\mu\text{m}$  which is the width of the channel is 0.004.

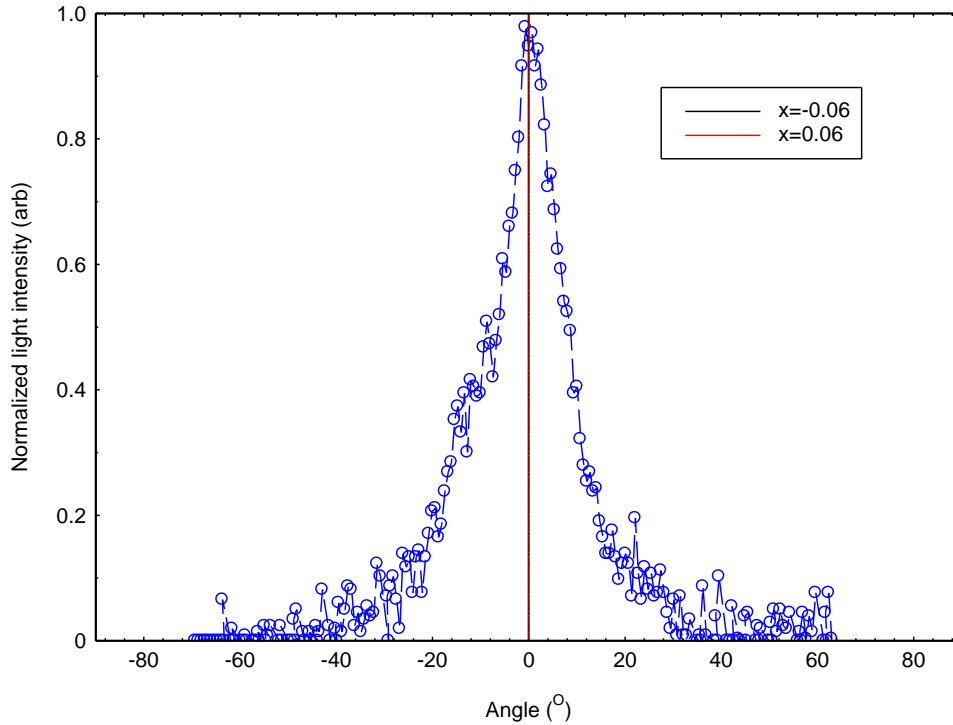


Figure 5.3 : The normalized angular far field profile of etched facet operating above threshold current.

This fraction is probably too small to be measured operating as one laser as a detector, but may influence the operation when the second section is operated as a laser as feedback on  $10^{-4}$  is known to affect the performance of solitary laser.

## 5.4 Light – Current –Voltage (LIV) Measurement

### 5.4.1 Laser 1 And Laser 2 As An Individual Laser

The light – current – voltage (LIV) measurement was performed on the fabricated prototype of a coupled cavity living laser. The individual laser cavity was checked by performing LIV test to ensure each of them are lasing and functioning well. The measurement of current – voltage (IV) characteristic is important to check that there are no irregularities from expected behavior, and that good electrical contact have been formed with no leakage current. The experimental setup for LIV measurement is shown in Section 3.1.3.3. The device was driven in pulsed operation with pulse width of 2000 ns,

1 kHz repetition rate and duty cycle of 0.2%. A longer pulse width is used in this experiment to allow measurement in the presence of interference effects, particularly at the beginning and the end of the pulse. The photodetector is placed in close proximity to the cleaved facet to detect the incoming light.

Figure 5.4 and Figure 5.5 show the current – voltage (IV) and light – current (LI) curves of laser 1 and laser 2 of the prototype of a coupled cavity living laser respectively. Both lasers are expected to have a diode-like behavior with turn on voltage approximately at 1.75 V. This turn on voltage corresponds to the internal field formed at the junction. The result shows that there is a negligible difference in I-V curves.

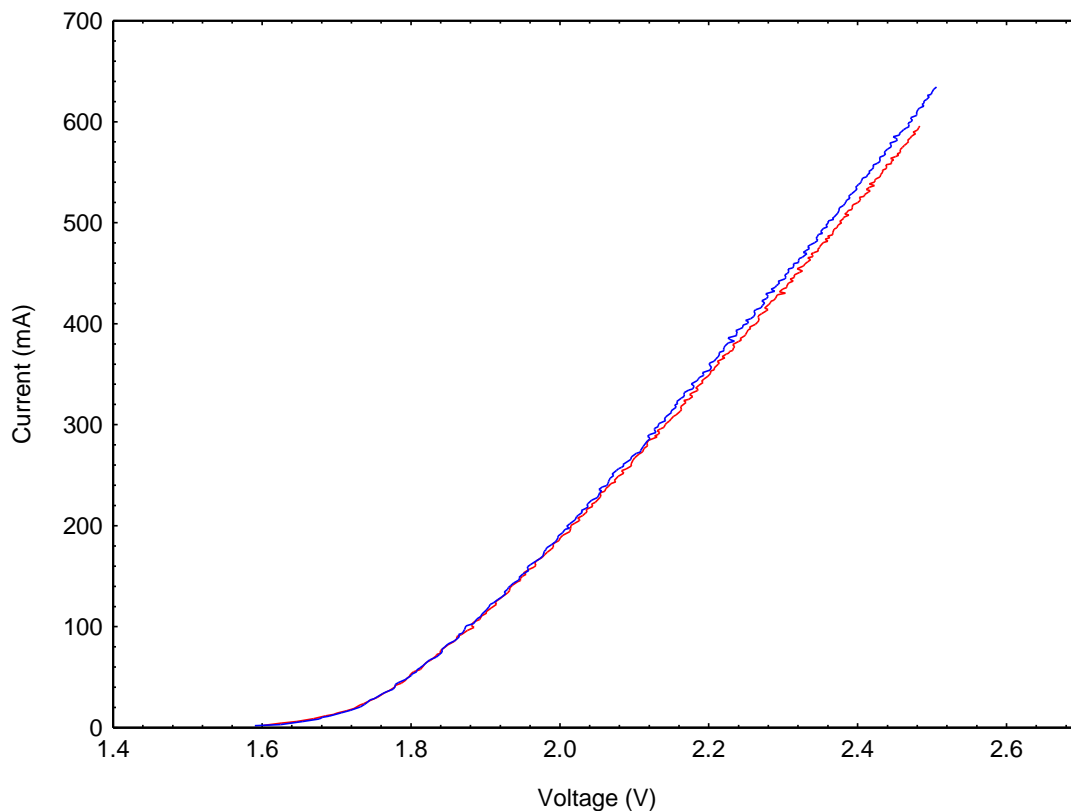


Figure 5.4 : Current - voltage (IV) curves of laser 1 (blue) and laser 2 (red) on a prototype of a coupled cavity living laser.

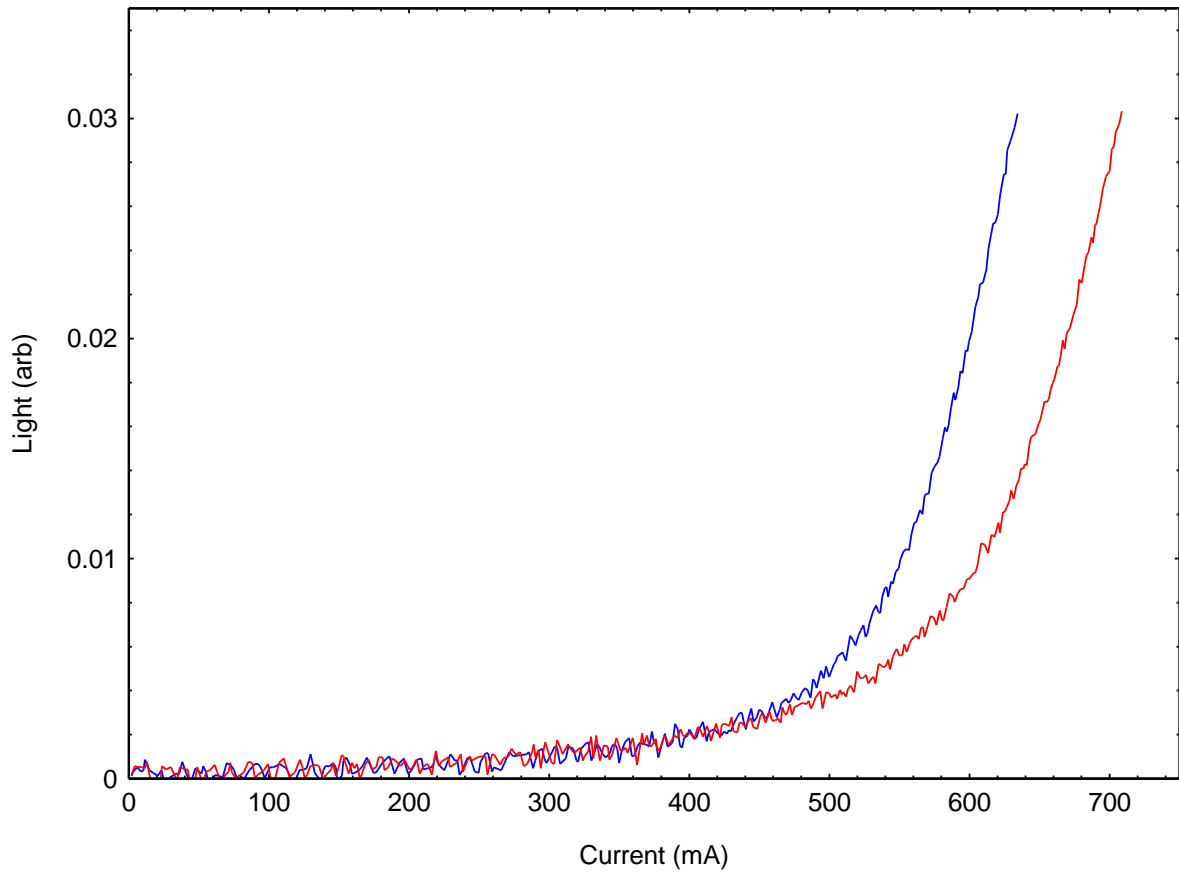


Figure 5.5 : Light - current (LI) curves of laser 1 (blue) and laser 2 (red) on a prototype of a coupled cavity living laser.

The LI curves for laser 1 and laser 2 show a difference in threshold current, which are 538 mA for laser 1 and 588 mA for laser 2. There is a small difference in length (laser 1 is 569  $\mu\text{m}$  and laser 2 is 605  $\mu\text{m}$ ) and the threshold current density will depend on length due to the different cavity losses. The threshold current density for laser 1 is 1231  $\text{A}/\text{cm}^2$  and 1265  $\text{A}/\text{cm}^2$  for laser 2. As the longer laser still has the larger threshold current density the difference cannot be explained by length and may be due to small differences in mirror quality. Nevertheless, the results prove that both lasers are lasing and functioning well individually. Hence, the device is expected to function well as a whole coupled cavity system.

### 5.4.2 Laser 1 And Laser 2 As A Source – Detector

The coupled cavity living laser in its simplest form may be able to operate in a source – detector mode. To test its function in a source – detector mode, one of the laser cavity is connected to the pulse generator. By forwards biasing it, the resulting light that is transmitted across the gap into and coupled into the active region of the opposing laser that function as a detector, can be detected by measuring photo-current generated in that laser.

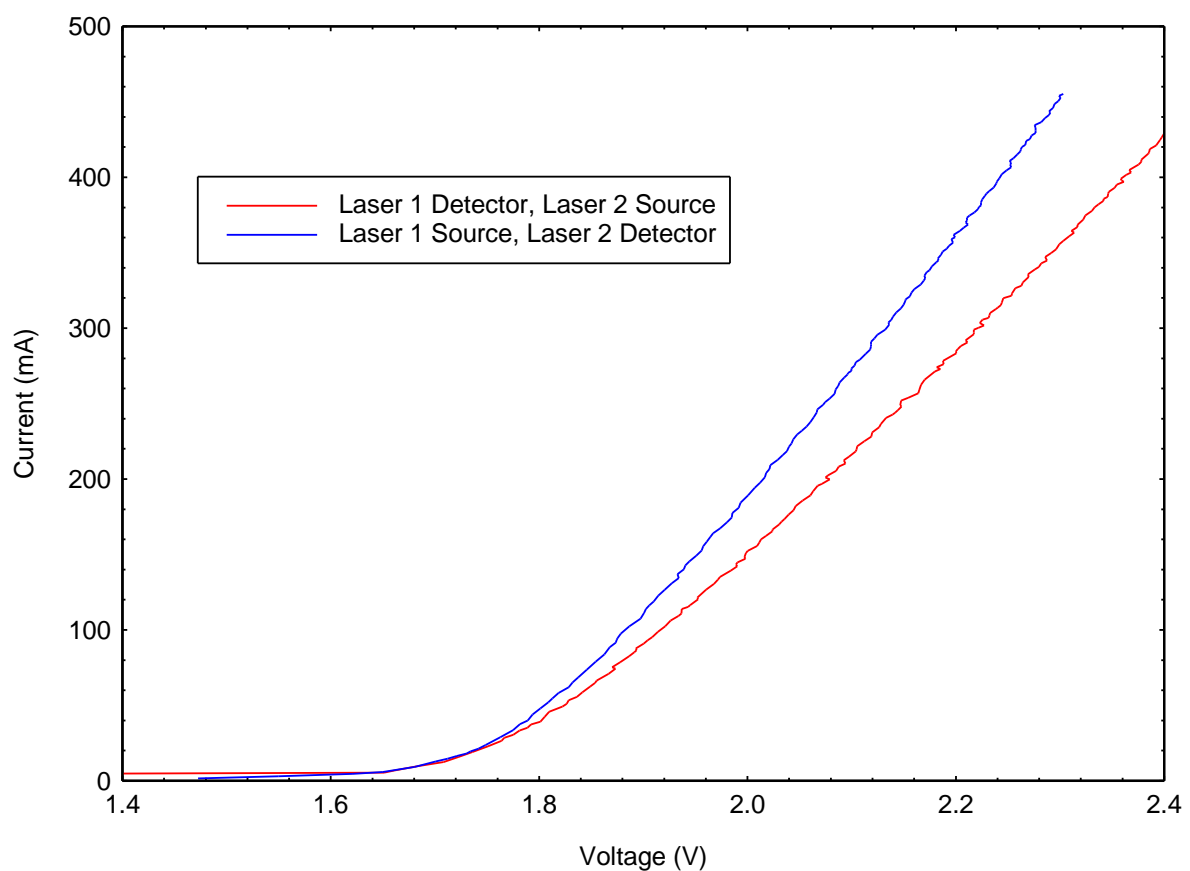


Figure 5.6 : Current - voltage (IV) curves of a coupled cavity living laser operating as a source and a detector.

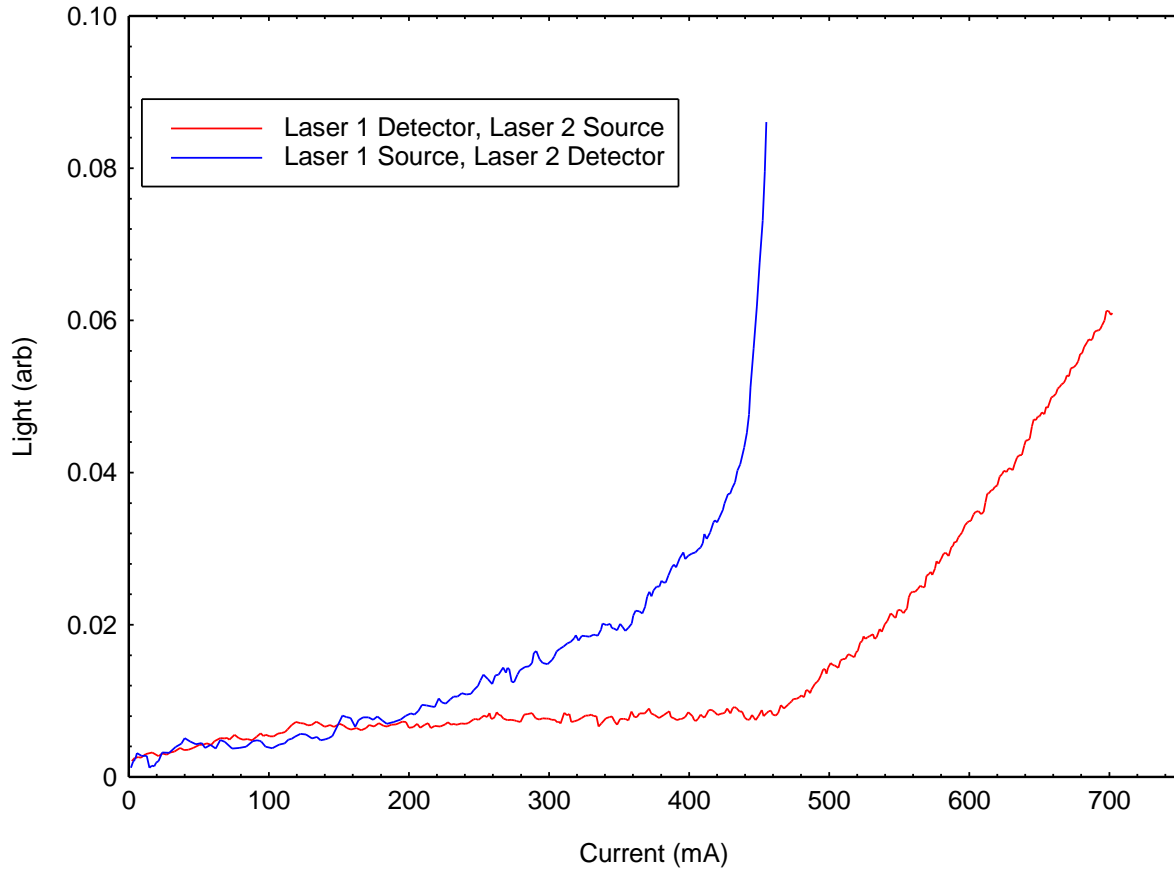


Figure 5.7 : Light – current (LI) curves of a coupled cavity living laser operating as a source and a detector.

Figure 5.7 and Figure 5.7 show the IV and LI curves of the prototype of a coupled cavity living laser with laser 1 operated as a source and laser 2 operated as a detector (blue) and vice versa (red). The turn on voltage for both operating mode is still the same as it is as an individual laser which is approximately 1.75 V. The threshold current for the laser as measured by the on-chip detector appears to have decreased from 538 mA to 421 mA for laser 1 and 588 mA to 446 mA for laser 2. However, this is unlikely to have occurred in practice and is most likely due to the very different location of the detectors. In the case of the on-chip detector the light has to travel 125  $\mu\text{m}$  before the light is coupled into the small slit shape detector. From the result of far field measurement, the proportion of emitted light transferred to the detector is small above threshold where the far-field measurements are performed. However, one of the key characteristics of a laser is that the stimulated emission process causes a spatial concentration of the light around threshold. This spatial concentration of the light will cause a greater divergence in the far

field (at 125 $\mu$ m) and collection of a decreasing fraction of the light from the other laser. We believe the change in the shape of the LI characteristic around threshold relative to that measured with the large area detector position further away leads to this apparent change in threshold. Both sets of results indicate that both parts of the coupled cavity laser are operating.

### **5.4.3 Laser 1 And Laser 2 As Laser – Laser**

The prototype of a coupled cavity living laser is also put to test for laser – laser mode. If one laser can affect another, the cell with certain features may alter the properties of another laser. Hence, making this device not only good for cell analysis but it also opens up the chance of a more sensitive bio-optical integration in the future. Therefore, to test whether one laser can affect another, the lasers have been pumped individually with separate but jointly triggered current sources. The second pulse generator is used to pump one laser with a constant pulse amplitude input current. The light – current characteristic of the opposing laser is measured by the computer controlled pulse generator. The measurement is taken for the current input varying below and above threshold current. The purpose of this measurement is to check if an increasing constant input current applied to one laser, will affect the performance of the opposing laser. Figure 5.8 and Figure 5.9 show the current – voltage and light – current characteristics of laser 1 when an increasing constant current is applied to laser 2 and vice versa in Figure 5.10 and Figure 5.11.

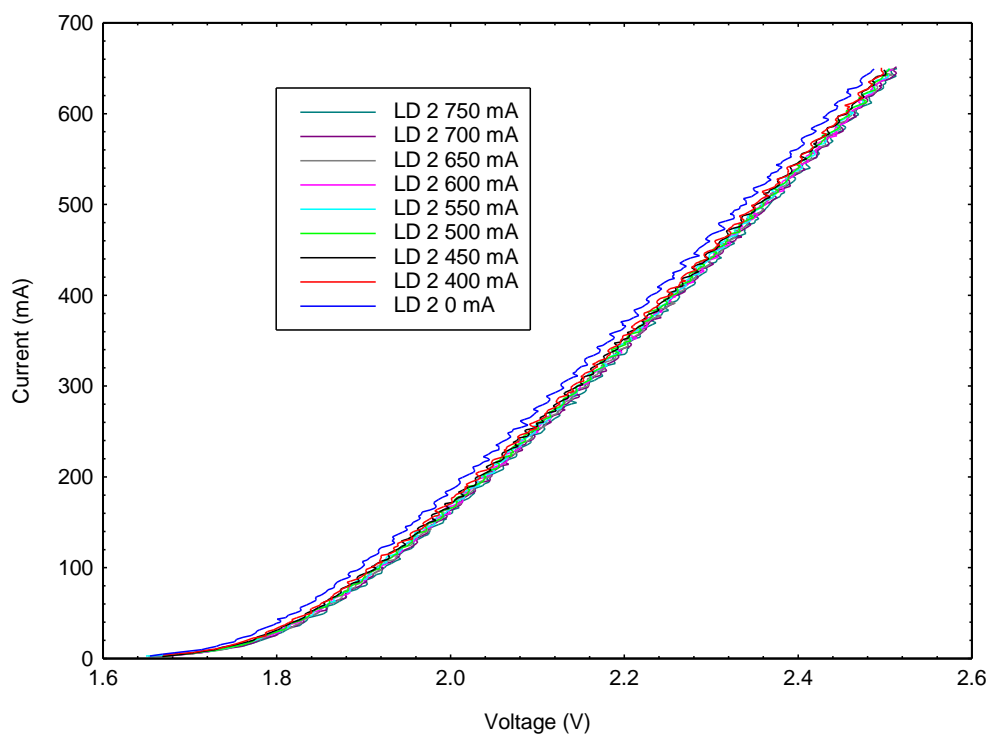


Figure 5.8 : Current – voltage (IV) curves of laser 1 when a constant current is applied to laser 2.

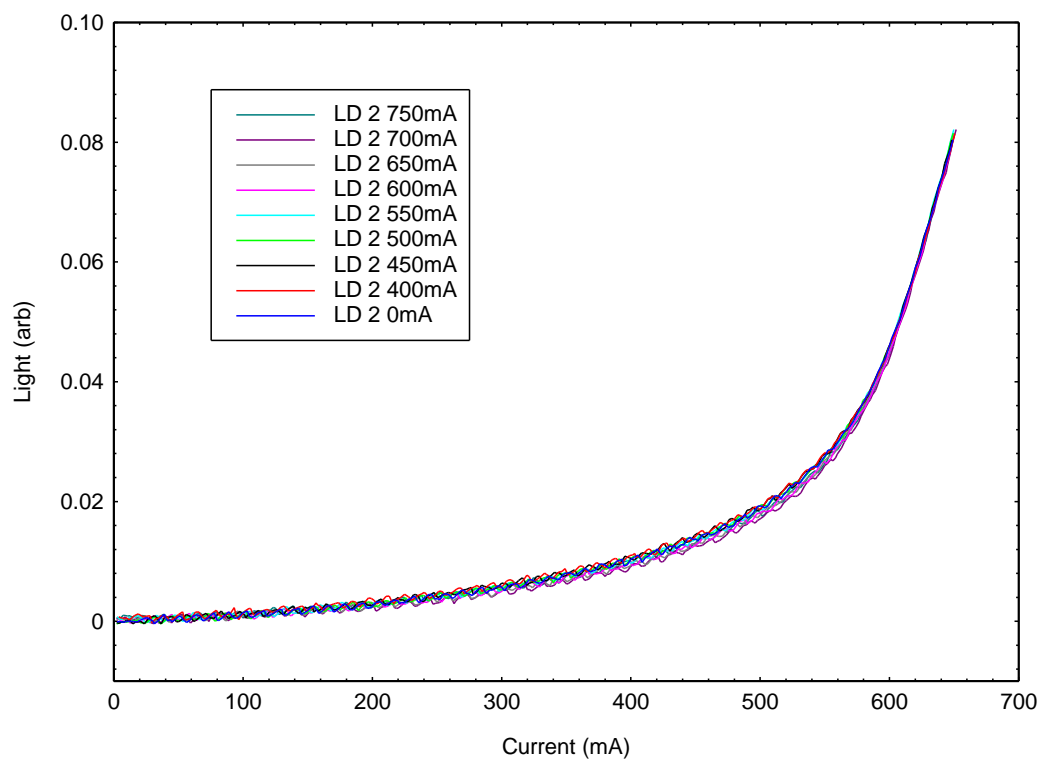


Figure 5.9 : Light – current (LI) curves of laser 1 when a constant current is applied to laser 2.



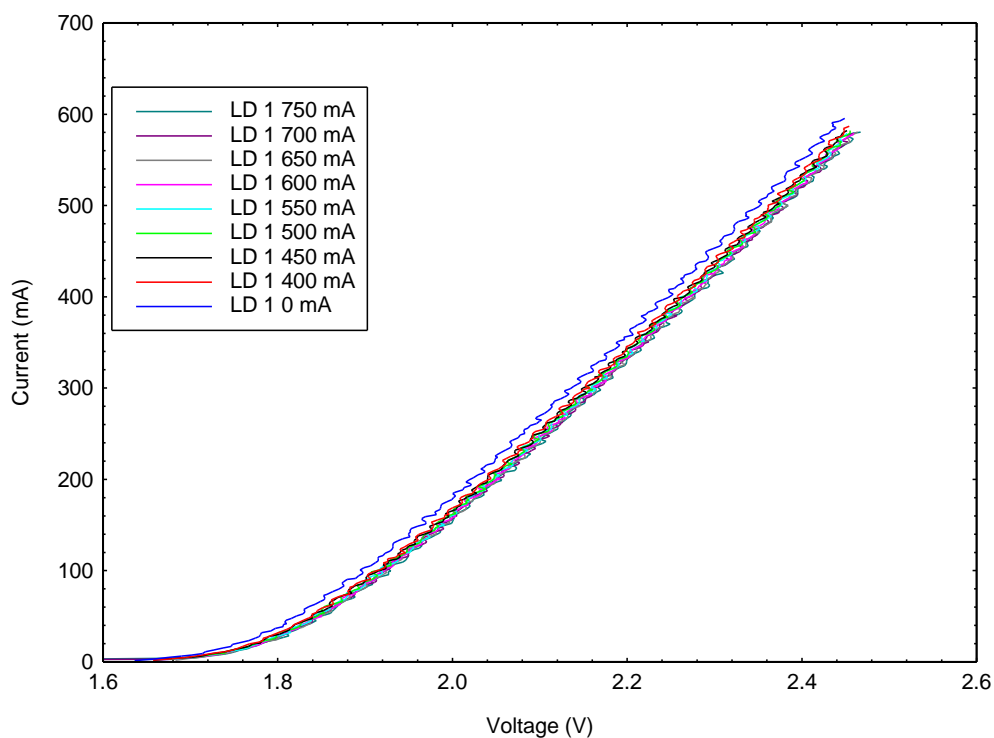


Figure 5.10 : Current – voltage (IV) curves of laser 2 when a constant current is applied to laser 1.

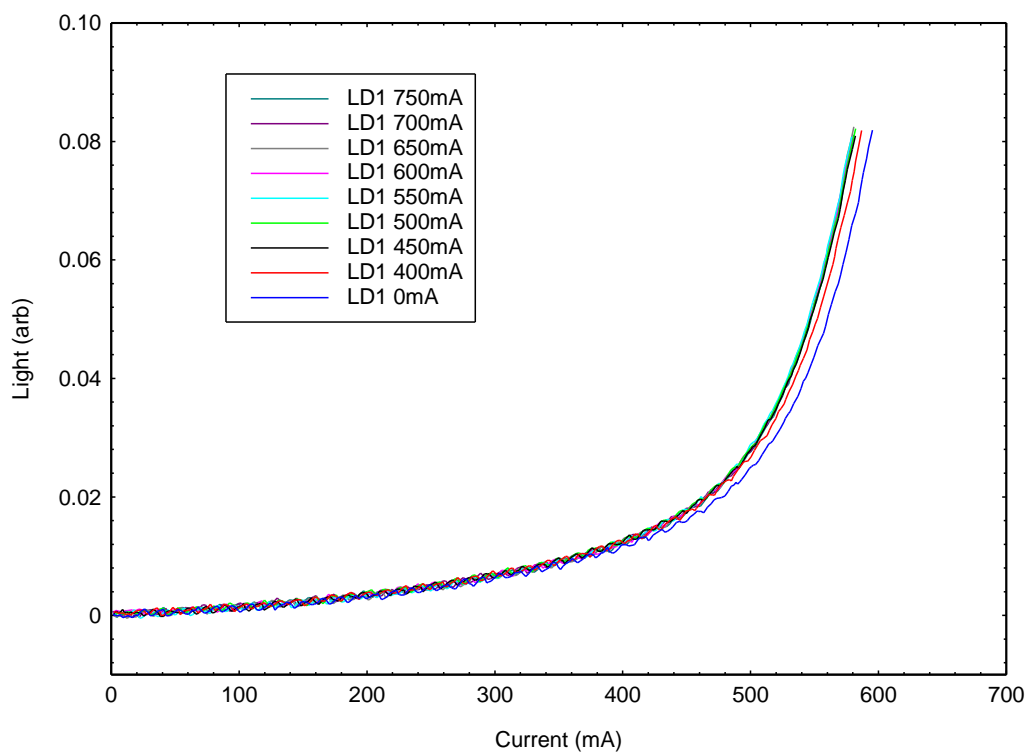


Figure 5.11 : Light – current (LI) curves of laser 2 when a constant current is applied to laser 1.

The very small differences in the I-V and L-I curves of Figure 5.10 to 5.13 demonstrate little obvious difference when the current to the second laser is altered over a very wide range from below lasing to above lasing. If there had been an electrical leakage from one to the other we might have expected a change in current over the whole characteristic and this may be happening in these curves to a very small degree. If a light induced change had been occurring such as optical pumping from one laser to the other we might have expected a larger change to the L-I characteristic above threshold compared to below threshold- as essentially we would have been reducing the mirror reflectivity. This does not appear to be the case and may be because of the very small fraction of the light from laser 1 coupled to laser 2.

### 5.5 Conclusion

This chapter describes the development of a processing procedure for the fabrication of the prototype of a coupled cavity living laser. The chosen active medium material is a quantum well based on the characterization measurements and analysis done in Chapter 3. Meanwhile, the fabrication procedure of inner etched facets of the prototype of a coupled cavity living laser is determined by the technique developed in Chapter 4. The fabricated prototype was then characterised.

The far field measurement have been performed on a cleaved-etched laser device to investigate the fraction of light from etched facet that will be coupled into the detector after travelling across a large 125  $\mu\text{m}$ . The result shows that the angular far field divergence  $\theta$  of  $25^\circ$  and the fraction overlap of the electric field profile which leaves the waveguide and the electric field profile after travelling a distance of 125  $\mu\text{m}$  which is the width of the channel,  $F(x)$  is 0.004.

The fabricated prototype of a coupled cavity living laser is working well as individual lasers with threshold current of 538 mA for laser 1 and 588 mA for laser 2. The device is also functioning well when operating as a source – detector although the apparent

threshold current is reduced for laser 1 to 421 mA when laser 1 is operating as a source and laser 2 as a detector. Meanwhile, the apparent threshold current of laser 2 is 446 mA when operating in vice versa mode. This may be due to the changing fraction of light coupled from one to another as the near field changes spatially around the laser threshold. The coupled laser does not show any obvious influence from one laser to the other and this may be due to the small fraction of light coupled from one to another. This could be greatly increased by reducing the distance between the lasers or using a laser with a smaller far field divergence.

## 5.6 Bibliography

- [1] K. W. Oh and C. H. Ahn, "A review of microvalves," *Journal of Micromechanics and Microengineering*, vol. 16, pp. R13 - R39, 2006.
- [2] D. J. Laser and J. G. Santiago, "A Review Of Micropumps," *Journal of Micromechanics and Microengineering*, vol. 14, pp. R35 - R64, 2004.
- [3] V. Hessel, H. Löwe and F. Schönfeld, "Micromixers— A Review On Passive And Active Mixing Principles," *Chemical Engineering Science*, vol. 60, pp. 2479 - 2501, 2005.
- [4] J. Fattaccioli, J. Baudry, J.-D. Emerard, E. Bertrand, C. Goubault, N. Henry and J. Bibette, "Size And Fluorescence Measurements Of Individual Droplets By Flow Cytometry," *Soft Matter*, vol. 5, pp. 2232 - 2238, 2009.
- [5] I. Schmid, W. J. Krall, C. H. Uittenbogaart, J. Braun and J. V. Giorgi, "Dead Cell Discrimination With 7-Amino-Actinomycin D In Combination With Dual Color Immunofluorescence In Single Laser Flow Cytometry," *Cytometry*, vol. 13, pp. 204 - 208, 1992.
- [6] D. A. Watson, L. O. Brown, D. F. Gaskill, M. Naivar, S. W. Graves, S. K. Doorn and J. P. Nolan, "A Flow Cytometer For The Measurement Of Raman Spectra," *Cytometer*, pp. 119 - 128, 2008.
- [7] M. D. J. H. C.-T. L. S. S. Monica Diez-Silva, "Shape and Biomechanical Characteristics of Human Red Blood," *US NIHPA Journal*, vol. 5, no. 35, pp. 382-388, 2010.
- [8] L. A. Coldren, S. W. Corzine and M. L. Mashanovotch, *Diode Laser and Photonic Integrated Circuit*, New Jersey: Wiley, 2012.
- [9] J. P. Brody, P. Yager, R. E. Goldstein and R. H. Austin, "Biotechnology At Low Reynoylds Number," *Biophysical Journal*, vol. 71, pp. 3430 - 3441, 1996.

- [10] J. G. Santiago, "Electroosmotic Flows in Microchannels with Finite Forces," *Analytical Chemistry*, vol. 73, no. 10, pp. 2353 - 2365, 2001.

## Chapter 6 : Conclusions And Future Work

### 6.1 Conclusions

This thesis describes the work that has been carried out to develop a prototype of a monolithic coupled cavity living laser for cell analysis. The work involves characterization of an active medium. Quantum well and quantum dot active media have been used as a comparison. The multisection devices were made for each of the materials. The multisection technique was used to for characterization purpose. Quantum dot active medium has much lower internal optical loss,  $\alpha_i$  which is  $2 \pm 1 \text{ cm}^{-1}$  compared to quantum well active medium which is  $12 \pm 3 \text{ cm}^{-1}$ . The  $\alpha_i$  remain unchanged within experimental uncertainty with temperature change. The gain spectra of quantum dot are broader with reduced peak gain magnitudes as compared to the quantum well sample that have narrow gain spectra with higher peak gain. The peak gain of both active media is observed shift to lower wavelength as the current density increased. The peak gain shift of quantum dot is larger than quantum well. This larger wavelength shift implies much greater scope for wavelength tuning of the coupled cavity device. Lower  $\alpha_i$ , broader gain spectra and larger peak gain shift gives advantage to quantum dot sample to be used as an active medium as it allows fabrication of the prototype of a coupled cavity living laser with a longer cavity whilst the device still operating at the saturated part of the gain. However, the maximum gain obtainable with quantum dot is smaller, which might limit the device performance with etched mirror with higher loss. Since we also have access to a more quantum well material, the fabrication of the prototype of a coupled cavity living laser is done with quantum well active medium material. It is believed that the device fabricated with quantum dot active medium will show better performance than the one fabricated with quantum well if the loss of the etched facet could be reduced.

Another aspect of the work is investigating the recipe for fabrication of etched facet. Though cleaving is a better approach of forming better quality facet, due to the monolithic design of the coupled cavity, an etching technique has been applied as an alternative. The investigation starts with selecting the mask for inductively coupled plasma etching of the

semiconductor. Silicon dioxide ( $\text{SiO}_2$ ) and nickel were tested as the mask material. Facet fabricated with  $\text{SiO}_2$  shows terraces and striated pattern due to volatile interaction between the etching chemical and the oxide during the high temperature inductively coupled plasma etching process. Meanwhile, the facet fabricated with nickel mask only shows a striated pattern without any terracing effect because there is no reaction between metal mask and etchant during plasma etching. Air plasma etching and oxygen etching were also tested for stripping resist at the bottom of the pattern before nickel evaporation. The results show that air plasma etch left residues on the sample due to contamination in the chamber redeposited back on the surface of the sample. Therefore, air plasma is not used in the process. Electron beam lithography was used for mask patterning in this work. The optimum exposure dose factor and developing time for fabrication of etched facet was investigated. The results show that the facet fabricated with higher exposure dose factor, which is 1.5, and lower development time, which is 40 seconds, makes an etched facet with better reflectivity, which is 0.24. The oxide stripe laser with cleaved – etched facet fabricated with a nickel mask with exposure dose factor 1.5 and development time 40 seconds have the lowest threshold current density which is  $754 \text{ Acm}^{-2}$ . An external and internal quantum efficiency,  $\eta_{ext}^d$  and  $\eta_{int}^d$ , shows better results, i.e higher value, at a higher exposure dose factor applied during electron beam lithography process. A facet reflectivity of 0.24 increases the optical loss from  $6 \text{ cm}^{-1}$  for a 2 mm long cavity with cleaved facets to  $6.6 \text{ cm}^{-1}$ . An appropriate gain can be achieved to overcome these losses with quantum dot material.

Finally, the processing procedure for fabrication of the prototype of coupled cavity laser is developed. A prototype has been successfully made by using quantum well active medium material and recipe of etched facet fabrication obtained from experiments in Chapter 4. The laser devices has been tested individually to ensure that it lasing and working well as an individual laser cavity. The result shows that both laser cavities are lasing with threshold current 538 mA and 588 mA. The far field measurement was also conducted to ensure the light emitted from the etched laser facet is able to be coupled into the opposing laser that serve as a detector. The result shows that the angular far field divergence  $\theta$  of  $25^\circ$  and the fraction overlap of the electric field profile which leaves the waveguide and the electric field profile after travelling a distance of  $125 \mu\text{m}$  which is the width of the channel,  $F(125 \mu\text{m})$  is 0.004. The fabricated prototype of a coupled cavity

living laser is also functioning well in a source – detector mode. Laser 1 appears to have the threshold current of 421 mA while laser 2 is 446 mA when operating as a source. This may be due to the change in detector position, size and shape which makes to collection of light more dependent on the emitted far field of the laser device. This far field will change around threshold due to the changing nearfield, that is one of the fundamental properties of a laser, resulting in a change in the L-I characteristic shape. When both sections are operating as lasers little difference can be seen on either due to the other and this may be due to the very small 0.004 fraction of light that is coupled above threshold.

## 6.2 Future Works

The prototype of a coupled cavity living laser has been successfully developed and fabricated in this work. However, there is still a lot of room for improvement for future work. Here are my recommendations for future works:

- i. To use quantum dot material as an active medium in the device. The results obtained in this work suggest that quantum dot is a better option for an active medium in this device. The lower internal optical loss, broader gain spectrum, larger peak gain shift allowing the device to be fabricated with longer cavity which is much needed requirement for the end product of a coupled cavity living laser. A longer device is more practical and convenient for handling during the mounting of electrical wire bonding for full circuit integration.
- ii. To apply the ridge waveguide laser system instead of a broad area laser. The width of the waveguide used in this work is 50  $\mu\text{m}$  and the average diameter of a red blood cell is 6 – 8  $\mu\text{m}$ . The cell may have a negligible effect on the coupling of the laser from the source into the detector. Hence, application of narrow ridge waveguide may enhance the influence that the cell have on optical coupling. Besides, exposure time taken in preparing the mask during electron beam lithography can be reduce significantly by using the ridge waveguide system since the area to be exposed is much smaller than the broad area design. The time taken



to exposing only 8 pairs of coupled cavity with beam current 0.16 nA with exposure dose factor of 1.5 is about 30 hours.

- iii. The channel width should be reduced and the laser layer structure designed to produce a smaller far field divergence to increase the fraction of light from one laser affecting the other. A far field divergence of  $8^\circ$  has been achieved in the literature [1]. With a channel width of 50  $\mu\text{m}$ , this would increase the fraction of light coupled from the source to detector to approximately 0.017.

## 6.3 Bibliography

- [1] M. V. Maximov, Y. M. Shernyakov, I. I. Novikov, L. Y. Karachinski, N. Y. Gordeev, U. Ben-Ami, D. Bortman-Abiv, A. Sharon, V. A. Shchukin, N. N. Ledentsov, T. Kettler, K. Posilovic and D. Bimberg, "High-Power Low-Beam Divergency Edge-Emitting Semiconductor Laser with 1- and 2-D Photonic Bandgap Crystal Waveguide.," *IEEE Journal of Selected Topics in Quantum Electronics*, vol. 14, no. 4, pp. 1113-1122, 2008.

